VIABILITY, DEVELOPMENT, AND RELIABILITY ASSESSMENT OF COUPLED COASTAL FORECASTING SYSTEMS

A Dissertation

by

GAURAV SINGHAL

Submitted to the Office of Graduate Studies of
Texas A&M University
in partial fulfillment of the requirements for the degree of

DOCTOR OF PHILOSOPHY

August 2011

Major Subject: Ocean Engineering

VIABILITY, DEVELOPMENT, AND RELIABILITY ASSESSMENT OF COUPLED COASTAL FORECASTING SYSTEMS

A Dissertation

by

GAURAV SINGHAL

Submitted to the Office of Graduate Studies of
Texas A&M University
in partial fulfillment of the requirements for the degree of

DOCTOR OF PHILOSOPHY

Approved by:

Co-Chairs of Committee,	Vijay G. Panchang
	James M. Kaihatu
Committee Members,	Billy L. Edge
	Gerald E. Hite
Head of Department,	John Niedzwecki

August 2011

Major Subject: Ocean Engineering

ABSTRACT

Viability, Development, and Reliability Assessment of Coupled Coastal Forecasting Systems. (August 2011)

Gaurav Singhal, B.Tech., Indian Institute of Technology, Kharagpur, India;
M.S., Texas A&M University
Co–Chairs of Advisory Committee: Dr. Vijay G. Panchang
Dr. James M. Kaihatu

Real-time wave forecasts are critical to a variety of coastal and offshore operations. NOAA's global wave forecasts, at present, do not extend into many coastal regions of interest. Even after more than two decades of the historical Exxon Valdez disaster, Cook Inlet (CI) and Prince William Sound (PWS) are regions that suffer from a lack of accurate wave forecast information. This dissertation develops high-resolution integrated wave forecasting schemes for these regions in order to meet the critical requirements associated with shipping, commercial and sport fishing vessel safety, and oil spill response. This dissertation also performs a detailed qualitative and quantitative assessment of the impact of various forcing functions on wave predictions, and develops maps showing extreme variations in significant wave heights (SWHs). For instance, it is found that the SWH could vary by as much as 1 m in the northern CI region in the presence of currents (hence justifying the need for integration of the wave model with a circulation model). Such maps can be useful for several engineering operations, and could also serve as a guidance tool as to what can be expected in certain regions. Aside from the system development, the issue of forecast reliability is also addressed for the PWS region in the context of the associated uncertainty which confronts the manager of engineering operations or other planners. For this purpose, high-resolution 36-h daily forecasts of SWHs are compared with measurements from buoys and satellites for about a year. The results show that 70% of the peak SWHs in the range 5-8 m were predicted with an accuracy of 15% or less for a forecast lead time of 9 h. On average, results indicate 70% or greater likelihood of the prediction falling within a tolerance of ±(1*RMSE) for all lead times. This analysis could not be performed for CI due to lack of data sources.

To My Parents

ACKNOWLEDGMENTS

First and foremost, I would like to extend my gratitude to Dr. Vijay Panchang for graciously accepting me as his PhD student in Fall 2007. Dr. Panchang provided continuous support and motivation throughout my research work. I am also grateful to Dr. James Kaihatu for willingly serving as the co-chair of my committee, and for providing insightful comments throughout my research.

I would also like to thank my committee members Drs. Billy Edge and Gerald Hite for their helpful suggestions/comments towards my doctoral research. Thanks also go to Drs. Martin Miller, Juan Horrillo, Carl Schoch, Ayal Anis, Zeki Demirbilek, and Earl Hayter. I would also like to thank NOAA, TIO, and Texas A&M Galveston's Research and Graduate Office for partial funding support.

I have also been blessed to have the support of a number of colleagues and friends throughout my research. I would like to thank Chan Kwon, Abhishek, Ashwin, Myoung Keun, Bo, Emily, Keith, Jitendra, Waqar, Puneet, Praveen, Sarabjyot, Veera, Prasenjit, Anuja, Rohit, and all others that I may have missed. I am also extremely grateful to the Gifford and Lewis families for graciously including me in several of their family holiday dinners.

Last but not the least, I am extremely grateful to my parents, elder brother Manish, sister-in-law Nisha, and nephew Kaushal for providing unconditional love and support throughout the course of my education. Without their sacrifices, I would not have made it thus far.

TABLE OF CONTENTS

LIST OF TABLES

LIST OF FIGURES

FIGURE Page

FIGURE Page

1. INTRODUCTION AND LITERATURE REVIEW

Operational wave forecasts, from a practical standpoint, are critical for safety of maritime operations (e.g. evacuation of oil platforms during storms/hurricanes), planning of coastal and offshore engineering activities (such as installation and maintenance of offshore structures), and sustainable management of coastal habitat and resources. During the Offshore Wind Energy Workshop (June 2009, Virginia), for instance, it was noted that the installation or operation of offshore wind turbines would be suspended for wind speeds greater than 12 m/s and seas associated with such winds. Wave forecasts are also critical to ship operators (cruise ship accidents caused by waves are well-publicized in the press), as well as to harbor masters responsible for securing boats and other equipment in a harbor during foul weather. In the case of oil spills, wave forecasts - in addition to ocean currents - may be needed for spill tracking, containment, and clean-up operations. In some cases, wave-induced surface drift can be of the same order of magnitude as the wind-induced currents that are typically used for predicting spill trajectories.

From a scientific perspective, numerical wave modeling serves as an efficient and cost-effective tool to examine the synoptic patterns of wave generation, propagation, and dissipation over a large spatial domain. In addition, analysis of the model results compared to measured data (if available) provides an estimate of the quality of the output (e.g. wave heights). Such estimates can be used to improve the model, if needed, by appropriate adjustment of the model parameters or by including more complex physical phenomena (wave-current interactions) that were initially excluded.

This dissertation follows the style of Ocean Engineering.

Furthermore, sensitivity studies of wave predictions to various forcing functions (e.g. winds, currents) help in identifying regions that are most sensitive to input variation and assessing the extent of fluctuation in the model results. For instance, by inducing an artificial adjustment (multiplying by a constant factor or adding random noise) to winds over a spatial region, the wave modeler is able to assess if such a change has any dramatic influence on the output in that region. Mapping of such regions through modeling studies could guide the future deployment of additional data source(s) in those regions. One can establish confidence in models through such data, and also help in understanding the dynamic behavior among various phenomena. Through sequential control of forcing functions in the numerical modeling, the modeler can also identify input forcing(s) that most influence the wave growth (or decay).

The work performed in this dissertation addresses the aforementioned scientific and practical aspects associated with the wave forecasts that have hitherto been only briefly examined. In particular, this dissertation develops the integrated forecasting system for two coastal domains, viz. Cook Inlet (CI) and Prince William Sound (PWS), Alaska by coupling wind, wave, and circulation models. Both these domains present unique challenges such as complex bathymetry, rugged coastlines, sharp topographical gradients that influence the wind-fields, significant swell energy from the Gulf of Alaska, and locally generated wind-seas in various channels and inlets. In addition, CI domain experiences strong tidal fluctuations with prominent wetting and drying of shallow areas. Simply put, these processes are complex, dynamic, and inter-twined that render numerical modeling extremely difficult in such domains.

Furthermore, in spite of the famous Exxon Valdez oil spill disaster more than two decades ago, these domains still lack wave information (data as well as reliable model predictions) that is critical for supporting the extensive oil, gas, shipping, fishing, and tourism industries. This dissertation, thus, answers several questions in order to develop operational wave forecasting systems and fulfill the practical needs associated with various activities noted above. In summary, the main contributions of this dissertation are:

- the development of high-resolution multiscale integrated wave forecasting schemes for coastal regions,
- the assessment of the viability of including higher order physics (wave-current interactions), from the viewpoint of efficiency and accuracy, in forecasting schemes that has not been studied in much detail in published literature,
- mapping of regions that show significant output variation through model sensitivity studies (as pointed earlier, this could benefit strategic deployment of gauges in the future),
- the development of new techniques for estimating the likelihood of occurrence and uncertainty of a given forecast for use in various practical applications, and
- the development of user-friendly interface for real-time dynamic coupling between wave and circulation models for forecasting purpose (this can be extended to any number or combination of models, e.g. wind, wave, current, sediment transport).

1.1 Historical background

The first evidence of wave predictions can be dated back to the Second World War, when the knowledge of sea-state was required for amphibious assaults in France and North Africa, including the D-day invasion at Normandy. Sverdrup and Munk

(1947) developed wave prediction theory using the wind and wave growth laws to estimate the sea-state, which was also validated using limited data at the time. The work of Pierson et al. (1955) introduced the concept of wave spectrum where the mean wave energy was shown to be distributed along various frequencies and directions, instead of being composed of only a single wave height and period. Gelci and others later described the evolution of wave spectrum using empirical equations (Gelci et al. 1956). Hasselmann (1962) derived a general expression for the source function of wave evolution which was based on three terms representing the wind input, the nonlinear transfer, and the dissipation due to whitecapping. The spectral wave energy equation based on Hasselmann's work can be described as follows:

$$\frac{DF(f,\theta)}{Dt} = S_{in} + S_{nl} + S_{ds} \tag{1}$$

where F is the mean wave energy spectrum, f is the wave frequency, and θ is the wave propagation direction. The left hand side of Eq.(1) represents the linear propagation of wave energy in space, whereas the right hand side is composed of the source and sink terms identified by Hasselmann. S_{in} describes the wave growth due to wind input (source term), S_{nl} describes the nonlinear wave-wave interactions, and S_{ds} is the dissipation term due to whitecapping (sink term); these terms are also dependent upon f, θ. The above equation is still being used in different forms today, most notably for the coastal waters where other nonlinear phenomena also affect the wave energy spectrum (discussed later).

A major breakthrough in understanding the evolution of wave spectra was made through the Joint North Sea Wave Project (JONSWAP; Hasselmann et al. 1973). Contrary to the Pierson-Moskowitz spectrum (Pierson and Moskowitz 1964), which showed that the waves become fully developed after wind blows steadily for a long duration, Hasselmann et al. (1973) found that the wave spectrum is never fully developed and rather continues to evolve in space and time through nonlinear wave-wave interactions.

In the mid to late 1970s, with the availability of faster computers, advancements to numerical wave predictions began to take shape. During the SWAMP study (SWAMP 1985), wave models were distinguished between the first generation (1G) and second generation (2G) type. 1G models neglected the nonlinear wave interactions, while the 2G models included such interactions in an empirical manner. Through various modeling tests, SWAMP study compared the performance of 1G and 2G models and found the results from the two models to be comparable. However for one test simulating the wind conditions during a hurricane, the models produced wave heights that differed significantly. It was then determined that the two-dimensional description of sea-state was more important than simply using parametric models. This finding led to the development of a full spectral model that provided full two-dimensional description of the sea-state. The full spectral model was classified as the third generation (3G) wave model. The 3G model explicitly accounts for the nonlinear wave interaction term (S_{nl} in Eq.1) and the spectral shape is allowed to develop dynamically without any constraints.

Modeling the sea-state using 3G models has become more efficient through advances in computing power and numerical schemes. The wave model (WAM) was the first 3G model (WAMDIG 1988; Komen et al. 1994) and solved the action balance equation of the form similar to Eq.(1). Since WAM, a number of other wave models have been developed such as WAVEWATCH III (hereafter WW3; Tolman 1991, 1999, 2009), Simulating Waves Nearshore (hereafter SWAN; Booij et al. 1999, Ris et al. 1999), etc. All these models belong to the 3G type and solve the full two-dimensional spectrum of the sea-state. In addition, these models have been used for wave hindcasting and forecasting throughout the world (details in the next section).

1.2 Overview of operational forecasting

Operational forecasting for offshore regions has been undertaken through the efforts of various meteorological offices such as the European Centre for Medium-Range Weather Forecasting (UK) or the National Oceanic and Atmospheric Administration (NOAA; USA) which have been providing, for several years, continuous forecasts of oceanic conditions (wind velocity, significant wave height (SWH), peak wave period (T_p), peak wave direction (D_p), etc.); these forecasts contribute to various engineering operations including, for example, the evacuation of oil platforms in advance of hurricanes in the Gulf of Mexico. As a result of these developments, the fundamental viability of the approach and the basic protocols for producing such forecasts have been established; various NWS offices (Eureka, Anchorage, Dickinson, etc.) and the public appear to be using the products. The results of the data suggest that (i) it is reasonable to expand such efforts to new regions where a demand for local ocean weather information exists, and (ii) it is necessary to address certain limitations encountered in present efforts (the "first generation" of coastal wave forecasting schemes), or in other words, to advance the technology through more sophisticated model implementation procedures in order to gain improved reliability.

In the US, NOAA's National Centers for Environmental Prediction (NCEP) uses the well established third-generation wave model WW3 which primarily incorporates formulations for wave generation, dissipation, and nonlinear wave-wave interactions. NCEP's modeling efforts encompass the entire globe at a coarse resolution ($\sim$ 30 km) and provide forecasts for upto 7 days in advance. NCEP's forecasts, however, do not extend into nearshore domains, primarily because in such regions other small-scale nonlinear phenomena exist that are not properly accounted for in the global version of WW3. Recently, a shallow water version of WW3 (version 3.14) became available that incorporates shallow water processes such as triad wave-wave interactions, bottom effects, and depth-induced wave breaking. NCEP uses the shallow water version of WW3 for the coastal regions of the US and generates forecasts on a multi-grid setup with better resolved grids. For example, in Alaskan waters, wave forecasts are generated on regional ($\sim$ 15 km) and coastal ($\sim$ 7 km) grids. Nevertheless, these resolutions are still not fine enough to resolve the rugged and whimsical coastal domains present throughout the US (e.g. Mobile Bay, Alabama; Corpus Christi, Texas; Gulf of Maine, Maine; Cook Inlet (CI) and Prince William Sound (PWS), Alaska; etc.). Furthermore, other higher order effects (such as those induced by the presence of currents, changing water levels, etc.) are still not part of NCEP's ongoing efforts and the role of such effects on the forecast efficiency and accuracy is not fully known.

One simple solution is to accommodate the effects of high-resolution local geometries and relevant physics (e.g. wave-current interaction) in regional models that interface with the NCEP's outer ocean forecasts, thus enabling the extension of NCEP's products into coastal regions at the appropriate scales. In recent years, coastal forecasting systems such as the Gulf of Maine Ocean Observing System (GOMOOS), the Alaska Ocean Observing System (AOOS), etc. which involve bay-scale domains coupled to the outer ocean forecasts have gained prominence. To account for the effect of tides and currents on the waves, the wave model is coupled with an appropriate circulation model. For instance, wave forecasts in Humboldt Bay (provided by National Weather Service, Eureka) include the effect of tidal currents near the harbor entrance. Coupled forecasts of surface waves and currents are also provided by the Naval Research Laboratory for the Mississippi and Southern California Bights. It is to be noted that although such systems exist, these are developed for domains that do not present complex challenges such as those found in CI and PWS. In particular, the tidal range and magnitude of the currents at these locations are not as extreme compared to those found in CI. In addition, the reliability and uncertainty of these systems has not been addressed in published literature.

Some other examples of forecasted metocean conditions include coastal currents in Galveston and Matagorda Bays (provided by the Texas Water Development Board http://midgewater.twdb.state.tx.us/bays˙estuaries/bhydpage.html), Penobscot Bay (www.gomoos.com); and wave conditions in Humboldt Bay (http://www.wrh.noaa.gov/eka/swan/), in the Great Lakes (provided by NOAA; http://www.glerl.noaa.gov/res/glcfs/), and in Penobscot and Massachusetts bays (www.gomoos.com).

1.3 Literature review

Several near-shore models, such as STWAVE, MIKE21, SWAN, WW3 v3.14, account for shallow water processes such as triad wave-wave interactions, dissipation due to bottom friction and depth-induced wave breaking (Booij et al. 1999; Ris et al. 1999; Sorensen et al. 2004; Tolman 2009) and can be used to extend the offshore wave climatology into near-shore areas. Notably, the wave model SWAN has received considerable attention for application in the coupled mode (note that "coupled" mode in this instance refers to coupling between a global and a local/regional wave model and not the coupling between a wave model and a circulation model) for engineering studies. For instance, Millar et al. (2007) coupled the coarse-resolution global simulations to a regional SWAN domain to examine the impacts of wave energy farms off the UK coast. However, their local simulations were performed for specific (a series of individual) wave events, in a "stationary" mode with zero wind imposed on the local grid. The inclusion of local winds was described by Rogers et al. (2007) for studies in Southern California Bight using multiple levels of grid coupling; again, however, the stationary mode was invoked, about which they acknowledge: “Use of stationary assumption for a large computational region can lead to poor timing of swell arrivals and temporal description of local growth and decay”. They also state: “the stationary assumption implies instantaneous wave propagation across the domain, as well as instantaneous wave response to changes in the wind field”. It is to be noted that in addition to these simplifications which could adversely impact predictions, these studies primarily involved hindcasts, as did the unsteady-state six-and-a-half years of coupled simulations performed by Panchang et al. (2008) for aquaculture engineering and other applications in coastal Maine. Some other studies that have tested various aspects of SWAN (some with multiple levels of nesting) in the hindcast mode include applications on the open coast (e.g. Rogers et al. (2003) in Mississippi Bight; Zubier et al. (2003) in Duck, NC) as well as those in semi-enclosed areas (e.g. Gorman and Nielsen (1999) in Manukau Harbor; Chen et al. (2005) in Mobile Bay; Moeini and Etemad-Shahidi (2007) in Lake Erie; Panchang et al. (2008) in Penobscot Bay). In contrast, studies related to the evaluation of SWAN in the forecast mode are scarce (e.g. Rogers et al. (2007) in Southern California Bight; Allard et al. (2008) in Portugal; Dykes et al. (2009) in the Adriatic Sea).

Although the viability of interconnecting regional wave models to global counterparts is well established, the impact of other higher order effects (wave-current interaction, wetting and drying, etc.) on regional wave models is still poorly understood. To account for such phenomena, the wave model has to be coupled to an appropriate circulation model. There are several theoretical as well as experimental studies that have addressed the effects of wave-current interaction, e.g. Huang et al. (1972), Thomas (1981), Nwogu (1993), Hedges et al. (1985), Chakraborti (1996), Guedes Soares and de Pablo (2006), etc. However, only a few studies have been undertaken for real-life applications. These include studies of Chen et al. (2007) and Funakoshi et al. (2008), who coupled SWAN and ADCIRC ("Advanced Circulation") for various applications in Mobile Bay and Florida, respectively. However, the intensity of currents in these studies was rather small ($\sim$ 0.5 m/s) compared to those found in CI ($\sim$ 2.5-3 m/s). Further, both studies were done in the hindcast mode where computational efficiency was not an issue. In the forecasting mode, on the other hand, efficiency becomes a critical consideration so that the output can be provided in reasonable time.

1.3.1 Hindcast vs. forecast

In engineering applications, simulations in the hindcast mode are usually limited in scope: they are performed for a set of predetermined specific events. These simulations can be repeated after modifying or adjusting various model parameters or forcing functions, using available data as a guide, and the best possible spatial/temporal resolution can be used. Simulations in the forecast mode, on the other hand, offer the modeler relatively little flexibility in this regard. The modeler has no data for the future and has little recourse (except data assimilation) if the forecast indicates a mismatch with the data (if available). Model resolution may be dictated to a greater extent by the logistics of obtaining a forecast rather than by modeling accuracy. Forcing functions also may contain inaccuracies, against which there may be no easy remedy. Thus, once a system has been designed (guided by hindcast studies), the modeler has little choice but to accept the flaws of the system. Therefore, a specific assessment of the forecast skill must be provided. This will enable the manager of engineering operations to invest the appropriate confidence in the forecast and plan accordingly. Indeed, companies providing met-ocean services are sometimes penalized if their predictions turn out to be faulty.

To address forecast uncertainty, forecast centers sometimes run wave model ensembles. This issue has also been recently addressed in a limited manner by Bidlot et al. (2002) for global simulations (not regional) and Dykes et al. (2009) for the Adriatic. These studies compared model predictions to data. However, the comparisons are provided in the form of the usual statistics (viz. correlation coefficients, best-fit slopes, scatter indices etc.) which do not, on their own, assist the manager of engineering operations in establishing the likelihood of occurrence of a predicted condition. In contrast, one of most significant contributions of this dissertation is the provision of forecast uncertainty to the end-user (in addition to the usual statistics).

1.4 Research objectives

To be more specific, the goals of this study are to develop integrated forecasting schemes and examine the issues noted above for coastal regions where accurate wave information is needed for a variety of coastal and offshore operations. Specifically, the forecasting schemes developed in this dissertation are tested for CI and PWS (Fig.1) domains. Even after more than two decades of the historic Exxon Valdez disaster, these regions suffer from a lack of accurate wave information. In addition, due to existing and ever expanding offshore engineering, there is an established need for ocean weather predictions in these regions. Numerous cargo ships, oil tankers, fishing, and recreational vessels traverse PWS and CI round the year.

As discussed earlier, from the technical/modeling perspective, the PWS and CI domains are characterized by extremely complex geometry, a larger overall size than most domains on which such programs have been implemented, islands and moun-

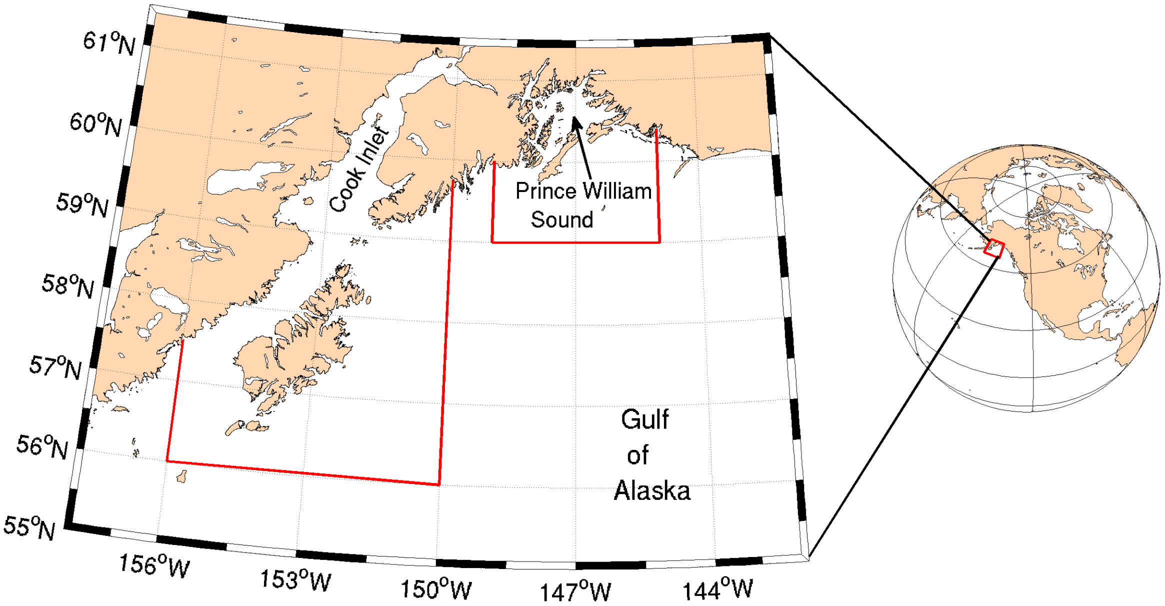

Fig. 1. Cook Inlet and Prince William Sound domains.

tainous terrains that influence the wind-fields, and strong tidal effects. It is therefore necessary to use a combination of wind, wave, and circulation models. There are several candidate models that can be utilized for such coupled studies. SWAN is the most suitable option for performing wave simulations in unsteady state. As for the circulation modeling, both finite element type (ADCIRC) and finite difference type (ROMS, POM, EFDC) models could be used. All these models have various capabilities and have been evaluated for numerous cases. In particular, EFDC ("Environmental Fluid Dynamics Code") is the most diverse and advanced three-dimensional model that internally links the hydrodynamic, sediment transport, water quality and eutrophication, and toxic contaminant transport (e.g. oil spill) submodels in a single source code (Hamrick 1992). Thus, EFDC has great advantage over other models in terms of eliminating the need for complex interfacing of multiple models to address the different processes. In this dissertation, SWAN and EFDC were chosen for wave and circulation modeling, respectively (details of the two models are given in Sections 2.1-2.3).

In particular, this dissertation addresses the adequacy of the circulation model and the level of wave-current interaction required to obtain appropriate forecasts in CI and PWS. A detailed qualitative assessment of coupled model predictions is also performed to determine regions which show prominent wave-current interactions. Due to paucity of observations in CI domain, quantitative comparisons, to the extent possible, are also made to assess the reliability of predictions in CI. In particular, the development of the CI integrated forecasting scheme is guided by a two-week period which consisted four distinct storm events with wave heights $\sim$ 5m. Sensitivity analysis is also performed to identify the sources of errors in the wave predictions and to map regions where such errors are large. Such analysis would eventually serve as "guidance" for estimating the modeling uncertainty of the forecasts, especially in CI region where no reliable information currently exists.

As for the PWS domain, more comprehensive datasets are available for estimating model veracity. Specifically, data from four buoys, two wave gauges, and three satellites are available, which greatly benefit the estimation of uncertainty of the model forecasts. Thus in this dissertation, the reliability assessment is done for about a year of wave predictions (June 2007 to May 2008) for PWS domain. This analysis provides the estimates of likelihood of occurrence of a given forecast (in addition to the usual statistics), which can be used by managers of engineering operations, who are ultimately interested in knowing the likelihood of a predicted condition to actually occur and the associated error bounds.

The dissertation is organized as follows. Section 2 provides an overview of the wave and circulation models and their governing equations. Section 3 describes the development of the integrated forecasting scheme for CI, followed by rigorous sensitivity analysis to study the impact of various forcing functions on wave predictions in Section 4. Results of Sections 3 and 4 motivate the study in Kachemak Bay (Section 5) to further study the effects of wave-current interaction on high-resolution grids. The focus is then shifted to PWS and the development of PWS forecasting system is first described in Section 6. This is followed by reliability assessment of the PWS forecasts in Section 7. Summary, conclusions, and directions for future work in Section 8 conclude this dissertation.

2. OVERVIEW OF WAVE AND CIRCULATION MODELS

2.1 Wave model

For simulating the wave-field, the wave model SWAN ("Simulating Waves Nearshore") was utilized. SWAN is a third-generation (since non-linear interactions are explicitly accounted for, see Section 1.1) spectral wave energy model capable of simulating wave propagation in time and space, shoaling, refraction, blocking, and reflection due to spatial variations in bathymetry and currents (Booij et al. 1999, Ris et al. 1999, Holthuijsen 2007).

In general, the wave models determine the evolution of action density N in space and time, rather than the energy density E. This is because in the presence of ambient current, the action density is conserved while the energy density is not. The action density is related to energy density by the expression $N = E/\sigma$, where σ is the relative wave frequency. The governing equation in SWAN model is thus based on the following spectral action balance in spherical coordinates:

$$\frac{\partial N}{\partial t} + \frac{\partial c_\lambda N}{\partial \lambda} + (\cos\varphi)^{-1}\frac{\partial c_\varphi \cos\varphi N}{\partial \varphi} + \frac{\partial c_\theta N}{\partial \theta} + \frac{\partial c_\sigma N}{\partial \sigma} = \frac{S_{tot}}{\sigma} \tag{2}$$

where N is the action density, λ and φ denote the geographical space coordinates (longitude and latitude, respectively), θ is the wave propagation direction (θ and σ denote the spectral space coordinates), and S_{tot} is the total source/sink term (similar to Eq. 1) that describes the wave growth due to wind input, nonlinear wave-wave interactions, and dissipation due to whitecapping, depth-induced wave breaking, and bottom friction.

The first term on the left-hand side of Eq. (2) represents the time rate of change of action density, the second and third terms represent the propagation of action density in geographical space with velocities c_λ and c_φ. The propagation velocities are given by the expressions $c_\lambda = (c_g cos\theta + u_\lambda)/(Rcos\varphi)$ and $c_\varphi = (c_g sin\theta + u_\varphi)/R$, where R is the radius of the earth, u_λ and u_φ are the depth-integrated ambient current velocities in longitudinal and latitudinal directions, respectively. The fourth term represents depth-induced and current-induced refraction, while the fifth term represents frequency shift due to variations in depths and currents. c_θ and c_σ represent propagation velocities in the spectral space. The group velocity $c_g = \partial\sigma/\partial k$ follows from the dispersion relation $\sigma = \sqrt{gk\tanh(kh)}$ where k is the wave number, and h is the water depth.

Note that Eq. (2) reduces to the energy balance equation in the absence of currents (the fifth term on left hand side of Eq. 2 disappears since there is no frequency shifting).

The SWAN model solves the above action balance equation using implicit solution schemes that are unconditionally stable (i.e. not dependent upon Courant-Friedrichs-Lewy criterion). Such schemes permit the use of finer grid resolutions without compromising the computational efficiency, which makes SWAN the appropriate choice for modeling studies undertaken in this dissertation.

2.2 Circulation model

This dissertation makes use of EPA's EFDC model (Hamrick 1992) for simulating barotropic circulation in the selected coastal domains. EFDC is capable of simulating three-dimensional flow, transport, and biogeochemical processes in surface water systems such as rivers, estuaries, lakes, reservoirs, and coastal regions. The EFDC model has been extensively tested and documented in a wide range of environmental and hydrodynamic studies (Kuo et al. 1996; Shen et al. 1999; Shen and Kuo 1999; Ji et al. 2001; Jin et al. 2001; Jin and Ji 2001, 2005; Park et al. 2005; Zou et al. 2006), and is being used by several universities, national laboratories, government agencies, and other private firms.

EFDC solves the three-dimensional, vertically hydrostatic, free surface, turbulent averaged equations of motion for a variable density fluid. The model uses a sigma vertical coordinate and cartesian or curvilinear, orthogonal horizontal coordinates. The model also incorporates the Mellor-Yamada level 2.5 turbulence closure scheme (Mellor and Yamada 1982) to explicitly solve for the vertical eddy viscosities in equations of motion. The model also has the capability to account for wetting and drying of shallow areas (Ji et al. 2001), which is of significance in CI domain given the large tidal fluctuations.

The generalized equations of EFDC with the horizontal curvilinear coordinates and the sigma vertical coordinate for the conservation of momentum and continuity are given by:

$$\begin{aligned}&\partial_t(mHu) + \partial_x(m_yHuu) + \partial_y(m_xHvu) + \partial_z(mwu) - mfHv \\ &\quad = -m_yH\partial_x(p+g\eta) - m_y(\partial_x h - z\partial_x H)\partial_z p + \partial_z(m\frac{A_v}{H}\partial_z u) + Q_u\end{aligned} \tag{3}$$

$$\begin{aligned}&\partial_t(mHv) + \partial_x(m_yHuv) + \partial_y(m_xHvv) + \partial_z(mwv) - mfHu \\ &\quad = -m_xH\partial_y(p+g\eta) - m_x(\partial_y h - z\partial_y H)\partial_z p + \partial_z(m\frac{A_v}{H}\partial_z v) + Q_v\end{aligned} \tag{4}$$

$$\partial_t(mH) + \partial_x(m_yHu) + \partial_y(m_xHv) + \partial_z(m_xm_yw) = Q_H \tag{5}$$

where x and y are the curvilinear-orthogonal coordinates, z is the vertical sigma coordinate, u and v are the horizontal velocity components, w is the vertical velocity in the sigma coordinate, m_x and m_y are the metric coefficients for curvilinear system and $m = m_x m_y$ is the Jacobian (if $m_x = m_y = 1$, the system becomes cartesian).

Eqs. (3), (4) represent the horizontal momentum conservation where H is the total depth ($= h + \eta$), with h being the depth below the surface ($z = 0$), and η the surface undulations around $z = 0$ (could be negative or positive). f is the coriolis parameter, A_v is the vertical eddy viscosity, p is the pressure term, Q_u and Q_v represent the momentum source/sink terms (e.g. wind stress, momentum diffusion). Eq. (5) represents the continuity equation. Q_H is the source/sink term that takes into account the freshwater discharge through rivers, precipitation, evaporation, and other sources. Note that the vertical momentum equation is based on the hydrostatic assumption, which relates vertical pressure gradient to the product of water density and gravity.

The equations (3)-(5) will form a closed system for the variables u, v, w, p and η, if the vertical turbulent viscosity (A_v) and the source/sink terms (Q_u, Q_v, and Q_H) are explicitly specified. The vertical turbulent viscosity is provided through the model developed by Mellor and Yamada (1982), which is based on a pair of transport equations for the turbulence intensity and length scale, and is computed internally in EFDC.

2.3 Background on wave-current interaction

When the waves encounter the currents and vice-versa, the excess momentum flux induces a net transfer of energy between the waves and the currents. As a result, the interaction alters both the waves and the currents.

2.3.1 Effect of currents on waves

Currents can affect the waves by changing the wavelength (or wave heights) and/or through refraction effects as waves propagate over a current. The changes in the wavelength depend upon the magnitude of the current speed and the angle between the wave propagation and current direction. In general, when waves and currents are in the same direction, the wavelength increases (wave height decreases and hence wave steepness - ratio of wave height/wavelength - decreases). In contrast, when the waves oppose the currents, wavelength decreases (wave heights increase and so does steepness). The equation relating the currents to the waves is given by

$$\omega = \sigma + \overrightarrow{k}.\overrightarrow{U} \tag{6}$$

where ω is the absolute angular frequency, σ is the relative angular frequency, $\overrightarrow{k}$ is the wave number vector, and $\overrightarrow{U}$ is the current velocity vector. This equation, in general, refers to the Doppler shift.

In SWAN, if ambient currents are present (e.g. output from a circulation model), then the iteration scheme solves for the action density propagation due to the shift in frequency (i.e. fifth term on left-hand side of Eq. 2 is accounted) through the use of relation in Eq. 6. As noted earlier, if ambient currents are not included, then the frequency shift term drops out from Eq. 2 and the governing equation reduces to the energy balance type.

2.3.2 Effect of waves on currents

Wave motion can also affect the waves through gradients of radiation stress (Longuet-Higgins and Stewart, 1964). Radiation stress usually refers to the mean excess momentum flux due to the presence of the waves. Variations in radiation stresses (i.e. the gradients) play an important role in understanding various coastal processes such as wave setup and setdown, wave-current interaction, and longshore current in the surf zone that affects the sediment transport.

SWAN, at present, does not compute wave-induced currents and thus these currents, if relevant, have to be included as a component while evaluating the current-field through the use of a circulation model. Similar to the wind stress, the circulation models simulate the wave-effects on currents through the gradients of radiation stress. This extra source term is added to the right-hand side of the horizontal momentum equations (usually a part of Q_u and Q_v in Eqs. 3, 4).

The equations for the gradients of the radiation stress are usually given by

$$F_x = -\frac{\partial S_{xx}}{\partial x} - \frac{\partial S_{xy}}{\partial y} \tag{7}$$

in the x-direction, and

$$F_y = -\frac{\partial S_{xy}}{\partial x} - \frac{\partial S_{yy}}{\partial y} \tag{8}$$

in the y-direction, where S_{xx}, S_{yy}, and S_{xy} are the components of the radiation stress tensor S. For a plane progressive wave propagating at an angle θ, these components can be expressed as:

$$S_{xx} = \left[(1+\cos^2\theta)\frac{kh}{\sinh 2kh} + \frac{1}{2}\cos^2\theta\right]E \tag{9}$$

$$S_{xy} = \left(\frac{kh}{2\sinh 2kh} + \frac{1}{4}\right)E\sin(2\theta) \tag{10}$$

$$S_{yy} = \left[(1 + \sin^2\theta)\frac{kd}{\sinh 2kh} + \frac{1}{2}\sin^2\theta\right] E \tag{11}$$

where h is the water depth, k is the wave number, and E is the wave energy. SWAN provides the output of gradients of radiation stress (F_x and F_y through eqs. 7-8), that could be used as input forcing in the circulation model to account for the wave-induced currents. EFDC, however, does not accept gradients of radiation stress directly. In particular, EFDC requires a radiation stress tensor (i.e. eqs. 9-11) and computes the gradients of radiation stress internally in the code. In addition, EFDC only accounts for the steady-state radiation stress forcing. SWAN, at present, does not have an option to output the radiation stress tensor.

To solve these issues, a separate code wrapper was built in EFDC that bypassed the requirement of radiation stress tensor. Essentially, the "unsteady" gradients of radiation stress from SWAN were directly embedded through this wrapper into EFDC. This forcing term was then added to the right-hand side of horizontal momentum equations of EFDC (Eqs. 3-4).

The updated EFDC code was tested for Dingemans case (Dingemans et al. 1987), that predicted wave-induced currents around a coastline with cosine-squared protuberance and rather straight bottom contours (both generated through formulas given in Dingemans paper). SWAN was forced by a single wave on the open boundaries, propagating in the +x-direction with wave height 1 m and period 8 s. SWAN-computed gradients of radiation stress were then fed into EFDC through the updated code wrapper. Fig. 2 shows the EFDC-modeled wave-induced currents for Dingemans test case. These results closely match those obtained by Dingemans (Fig. 10 of Dingemans et al. 1987). This exercise shows that the updated version of EFDC works well for simulating wave-induced currents.

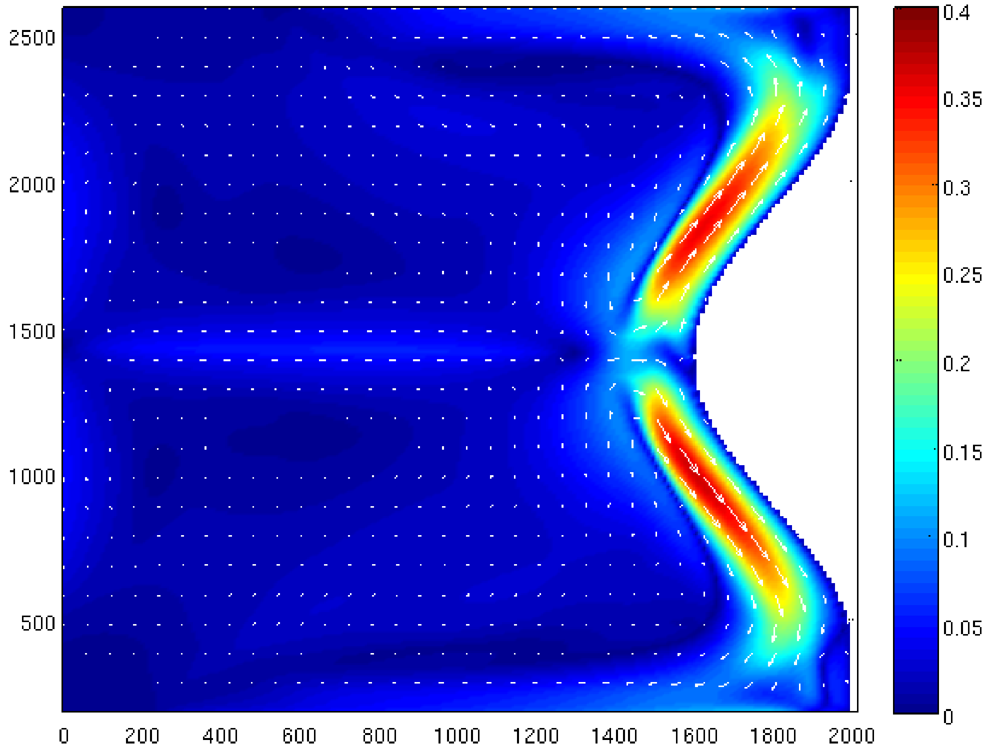

Fig. 2. Wave-induced currents (in m/sec) from EFDC using code wrapper for gradients of radiation stress.

3. DEVELOPMENT OF INTEGRATED WAVE FORECASTING SCHEME FOR COOK INLET, ALASKA

3.1 Introduction

Cook Inlet (CI) is a large estuary (∼180 miles long), stretching from the Gulf of Alaska to Anchorage in south-central Alaska (Fig. 3) and experiences a great deal of human activity (such as shipping, oil and gas extraction, etc). Approximately half of Alaska's population lives along CI's shores. Anchorage, between Turnagain and Knik Arms at the head of CI, is Alaska's largest city and a center of transportation, commerce, industry, and tourism. The Port of Anchorage receives food, fuel, building materials, durable and expendable supplies for delivery to over 80% of Alaska's population and to four large military installations; while seafood, minerals, and gas are exported. Shipping routes in CI serve the port year-round, as well as the ports of Nikiski, Homer, and Drift River with transshipment to smaller coastal communities. Other marine traffic is related to the recreation and tourism industries as well as commercial fishing. Homer Harbor is one of the largest boat harbors in the state and accommodates commercial and charter fishing, excursion, government agency, and private recreation boats. The majority of citizens living in south-central Alaska rely on the marine environment to some extent for subsistence, recreation, or commerce.

CI is also an extremely dynamic system. Being exposed on three sides to the Gulf of Alaska, which has among the largest waves in the world, the activities noted above can be subject to complex and dangerous surface wave action. A cursory examination of the brief dataset available from Buoy 46105 (hereafter, B05), near Stevenson Passage, suggests that significant wave heights (SWHs) can be as large

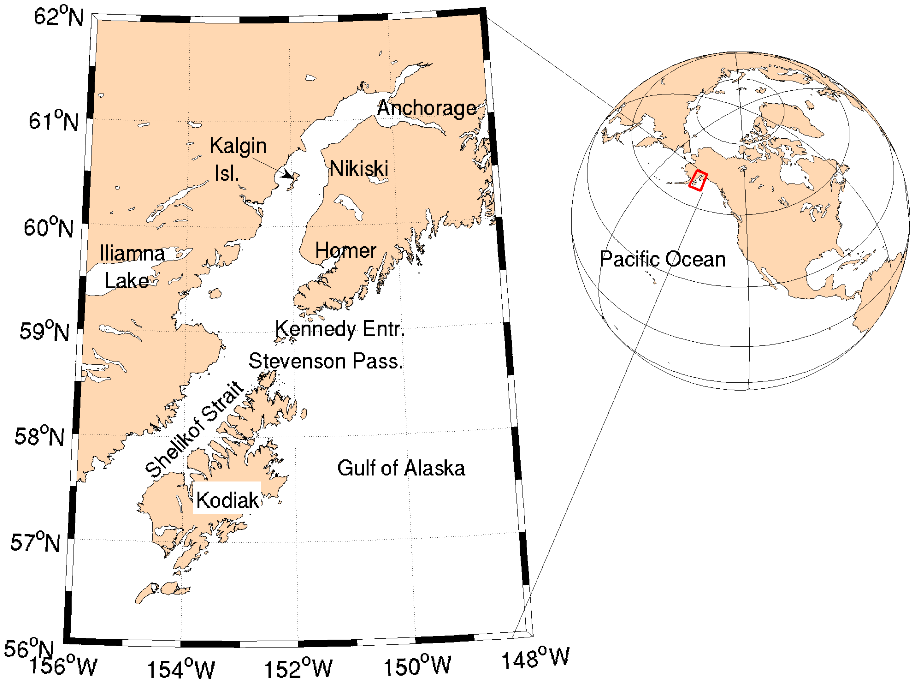

Fig. 3. Cook Inlet domain.

as 7 m (corresponding to “maximum” wave conditions of about 13 m in that sea-state). There are also large tidal variations (about 8-9 m, the largest in the US) and the complex bathymetry and coastal morphology result in large tidal currents. For example, tidal bores are commonly found in Turnagain Arm, creating currents in excess of 2-3 m/s. Currents on the order of 1-2 m/s also occur throughout the inlet during full tidal flow. There is also significant wave/current action and during low tide, silty bottoms (mudflats) are exposed which compound navigation difficulties. The Anchorage Daily News has often publicized grounding of boats during low tide. In addition, the interaction of rugged topography (mountain ranges with elevations that abruptly rise to 3000 m, gaps, and channels) with the strong atmospheric pressure gradients results in the so-called “gap winds” that adversely affect maritime and aviation activities during the winter season (Liu et al. 2006). Also important is the impact of the strong tidal flows through lower CI into and out of the Gulf of Alaska. Mariners piloting vessels in the region attest to the impact of the interaction of these forces on maritime operations. Given the paucity of wave observations in CI, it is critical to provide accurate and timely forecasts of surface conditions through the use of state-of-the-art wave/circulation models.

Over the last few years, several regional wave forecasting systems have been established for various locations around the US. As discussed in Section 1.2, these systems provide wave forecasts on high-resolution grids and are connected to NCEP's coarse resolution global wave forecasts (Tolman 2009). In some cases, the regional wave model is also coupled with the circulation model to account for wave-current interaction (Chen et al. 2007, Funakoshi et al. 2008).

The viability of interconnecting multiple models (i.e. winds, waves, and currents) in dynamic environment such as CI presents unique challenges that have hitherto been only briefly examined. The sharp topographic gradients produce complex wind regimes that should be properly modeled, in order to obtain reliable simulations of waves and currents. The strong currents noted earlier, which are created by winds, tides, and other (e.g. baroclinic forcing) mechanisms, can influence the waves (a strong opposing current could increase the wave height and steepness). Waves, in turn, could also affect the currents by transferring their momentum to currents through gradients of radiation stress (Longuet-Higgins and Stewart 1964). This dynamic feedback between the waves and the currents, and its effect on surface conditions should thus be addressed in CI wave modeling. The interest of this study is to include those phenomena in regional forecasting schemes that may indeed affect the waves, but without expanding the cost and effort required to generate the forecast.

This section describes the development of an integrated wave model that includes the complex effects induced by winds, currents, and water-levels in CI. Wave-current interaction is studied by one- and two-way coupling of the wave and circulation models, using a two-week period in October 2008 that included multiple storm events with winds in excess of 20 m/s and SWHs about 4-6 m in lower CI. Such events are potentially hazardous to mariners and fishermen operating in the region. SWAN and EFDC were chosen for wave and circulation modeling, respectively. In particular, this study addresses the adequacy of the circulation model and the level of wave-current interaction (one-way or two-way) required to obtain appropriate forecasts. The influence of the time interval for information exchange between the two models on the results and on modeling efficiency is also addressed. A detailed qualitative and quantitative assessment of coupled model predictions is also performed to determine regions which show prominent wave-current interactions. Spatial maps showing the extreme SWH variation in the presence of currents are also created for use in various applications.

This section is organized as follows: Section 3.2 provides a description of various bathymetric datasets available, along with a qualitative assessment of bathymetric patterns in the CI region. Section 3.3 describes the surface-wind models available for use in the wave and circulation modeling schemes, followed by Section 3.4 that addresses the development of a basic circulation model, run in the barotropic mode (with tides, winds, and river discharge), for wave forecasting purposes. The adequacy of the barotropic model is also addressed by comparison with flow measurements in various parts of the CI domain. Section 3.5 describes the development of a general wave model for CI, followed by Section 3.6 that describes the coupling options suitable for wave-current interaction studies, along with the coupling procedure. Section 3.7 describes the application of coupled modeling system to four storm events, followed by discussion in Section 3.8.

3.2 Bathymetric information and available datasets

Bathymetry is one of the most critical aspects regarding the performance of any coastal model. Plant et al. (2009) showed the influence of bathymetric filtering on wave and flow fields, and found that the model results were extremely sensitive to the resolution of input bathymetry.

NOAA's National Geophysical Data Center provides various bathymetric datasets for CI such as Etopo1/Etopo2 Global Relief Models, Tsunami Inundation Digital Elevation Model (DEM; NOAA Center for Tsunami Research), etc. The Etopo datasets have a fairly low resolution (1 min and 2 min) and do not properly resolve many complex bathymetric features of CI, while the DEM dataset is available at a 24 sec resolution, presently the highest resolution available for CI region.

Although the DEM is the best available resolution for CI domain, the Turnagain arm region of upper CI is not properly resolved. In the entire arm, the depths are set to 3 cm (due to missing data) which may be inappropriate to simulate the wetting and drying of the region. To compensate for the missing bathymetry, past NOS surveys (conducted between 1900-1939) were utilized along with the navigational charts in the Turnagain Arm region. These data were interpolated onto the existing DEM to generate a more reliable bathymetry (a similar approach was used by Oey et al. 2007). The updated bathymetry is shown in Fig. 4. In general, the depths decrease from about 200 m near Stevenson Passage (in the south) to about 50 m in the central inlet. The depths also show across-shore variability in various regions

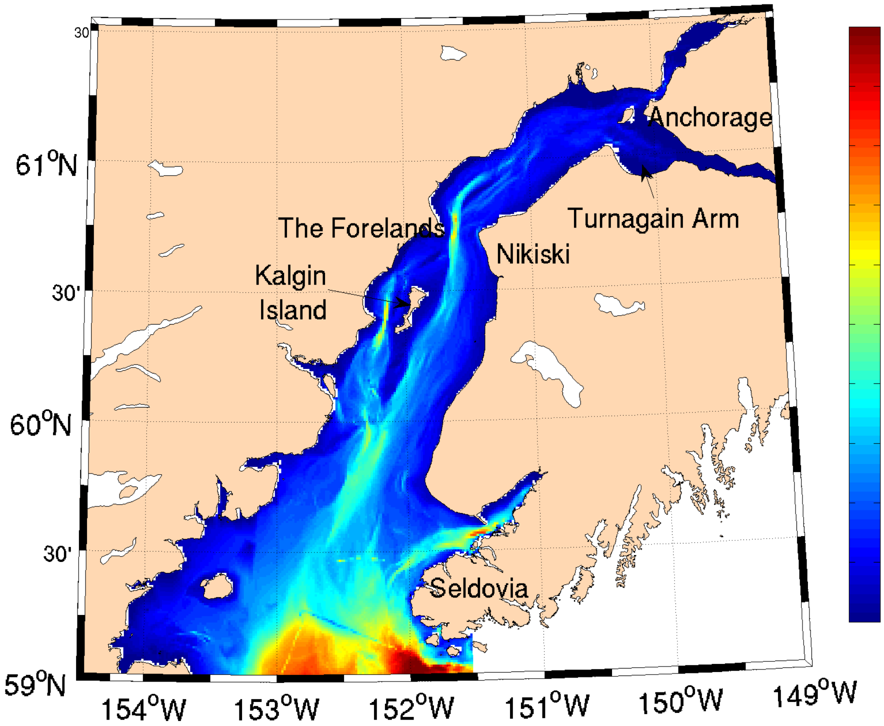

Fig. 4. Bathymetry of Cook Inlet (in meters).

(e.g. near Kalgin Island), with depths reducing from greater than 50 m to less than 10 m. Overall, CI is mostly shallow with an average depth of about 50 m.

3.3 Surface weather patterns

CI experiences very complex and dynamic weather patterns. During the winter season, winds in the northern Gulf of Alaska are a result of cyclonic storm systems off the Pacific and attain maximum strength from October through March (Stabeno et al. 2004). Due to the presence of Chugach Mountains (spanning the entire CI coastline), these storms linger and funnel down through various gaps and channels resulting into random and complex wind regime (Liu et al. 2006). It is critical to reliably model such complex weather patterns for forecasting purposes, since it is frequently stated that the quality of wave model predictions are most dependent on the quality of the input winds (Dykes et al. 2009). Unfortunately, there are not many weather stations that provide a synoptic snapshot of wind patterns over the entire CI. For example, the northern CI (north of the Forelands) only has one weather station near Anchorage that was installed by the NOS in April 2005, which provides real-time measurements of wind and gust speed, wind direction, air temperature and pressure every six minutes. Elsewhere, there are a total of six active weather stations, but these are too few to obtain a reliable description of weather patterns over this region (Fig. 5).

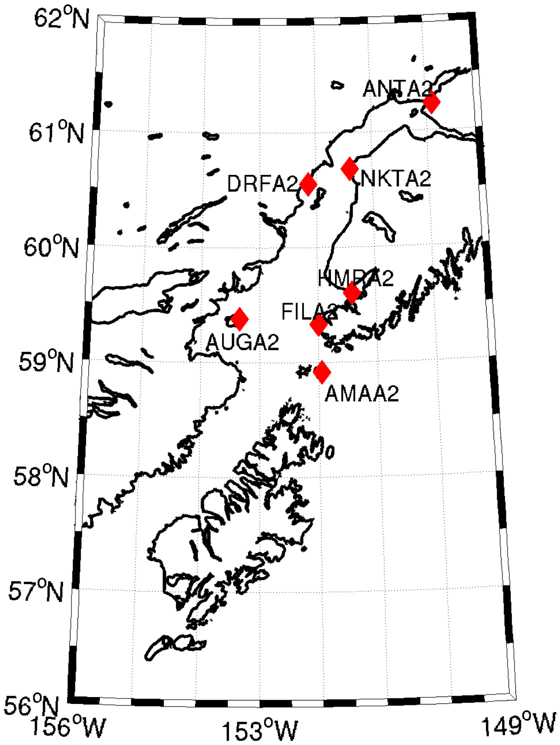

Fig. 5. Locations of weather stations in CI domain.

Over the last few years, NCEP's NAM ("North-American Mesoscale") model has provided a synoptic snapshot of surface winds over the global ocean, which are assimilated through satellite-based measurements to improve their reliability. However, the NAM winds do not properly account for coastal topographical variations, their resolution is much too coarse, and often these winds do not extend into several coastal domains (e.g CI, PWS, etc.). As an example, Fig. 6 shows a sample plot of predicted winds using NCEP's NAM model at a resolution of about 7 km. It can be clearly seen that the NAM model does not appropriately resolve the wind-fields near the coastlines and also does not extend inside the PWS domain, and hence may have adverse implications to nearshore wave and circulation modeling.

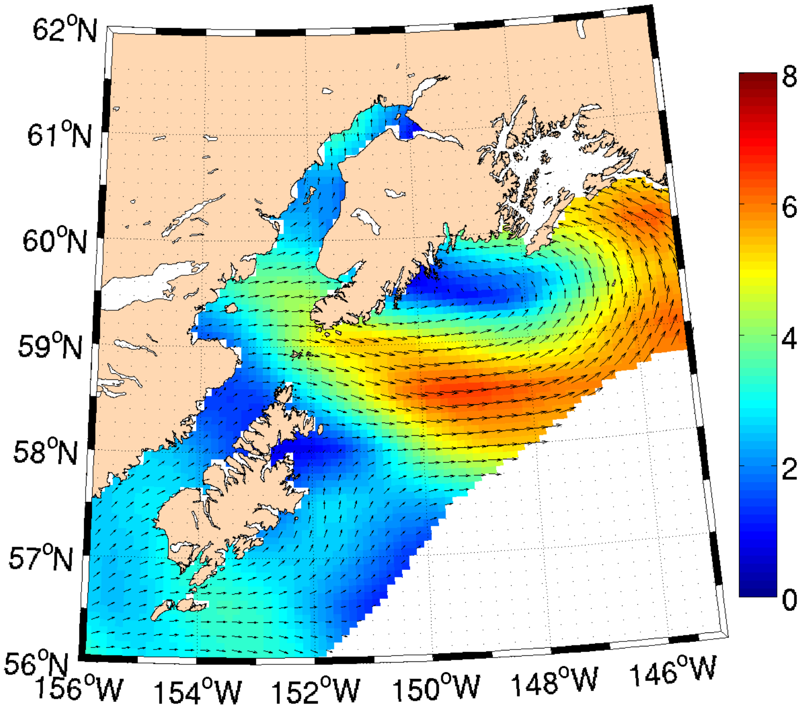

Fig. 6. Sample plot of NCEP predicted winds over northern Gulf of Alaska. Color represents wind speed (in meters/sec), whereas arrows depict wind direction.

Since early 2007, operational weather forecasts using the WRF ("Weather Research and Forecasting") model have become available (http://aeff.uaf.alaska.edu/). These provide better coverage of the CI domain and use resolutions fine enough to resolve the salient features of the underlying topography. WRF is also the latest mesoscale model adopted by the National Weather Service as well as the U.S. military and other meteorological services for generating high resolution weather forecasts in various coastal regions. The WRF model performance has been documented in several studies (e.g. Done et al. 2004; Kain et al. 2006; Mölders 2008). Details of the model and its performance are discussed elsewhere (Olsson and Volz 2011; Mölders et al. 2008). While there are some errors in the predictions (described later), Singhal et al. (2010) found their effect on wave predictions to be marginal. A sample plot of WRF predicted winds is shown in Fig. 7, and being on a higher resolution, it extends into nearshore domains. This dissertation thus uses the WRF winds obtained through the link noted above for wave modeling in CI.

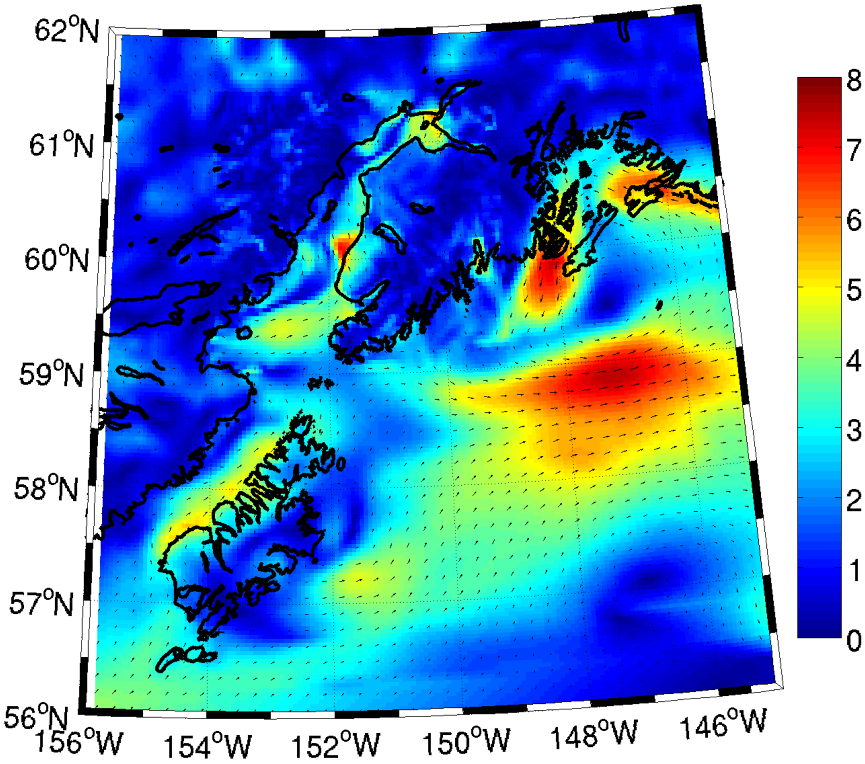

Fig. 7. Same as Fig. 6 but for WRF predicted winds.

3.4 Surface-current patterns and modeling

Circulation in CI is mostly tidally-driven with tidal period predominantly due to the M2 tidal constituent. The natural resonant frequency of CI is roughly equivalent to that of the tidal frequency, and as a result CI experiences one of the largest tidal fluctuations in the world. In addition to tidal forcing, wind-driven and buoyancy-driven flows also contribute to the overall circulation patterns in CI (Okkonen and Howell, 2003, Okkonen et al. 2009). Tidal and baroclinic effects were also addressed in modeling studies by Oey et al. (2007) and Johnson (2008). While these studies have addressed the circulation patterns and their seasonality in CI, how these affect the wave climate in general has yet to be understood. Thus, the emphasis here is on the development of a base circulation model that is capable of simulating the barotropic circulation (wind, tide, and river discharge). The output of the circulation model (i.e. surface-currents/water levels) will be used as input to the wave model. The goals are to 1) address the adequacy of the barotropic model, 2) understand the effects of wave-current interaction on overall wave climate in CI, and 3) examine the impact of adding currents/water-levels in the wave model from the viewpoint of efficiency of the forecasts.

For barotropic modeling, the EFDC model is utilized. The model was applied to the CI domain covering the region between -156 W to -149 W and 56 N to 61.5 N, on an irregular grid with a resolution of about 4 km at the open ocean boundaries, and decreasing to a resolution of $\sim$ 1.5 km in the northern-most parts of CI (Fig. 8). Other model resolutions were also tested (e.g. <1 km) for this domain, however the model simulation time increased drastically for higher resolutions without a major impact on the accuracy of the results. Since the goal is to transition the modeling into real-time operational mode, some compromise regarding the model grid resolution is needed in order to make efficient, yet accurate, forecasts.

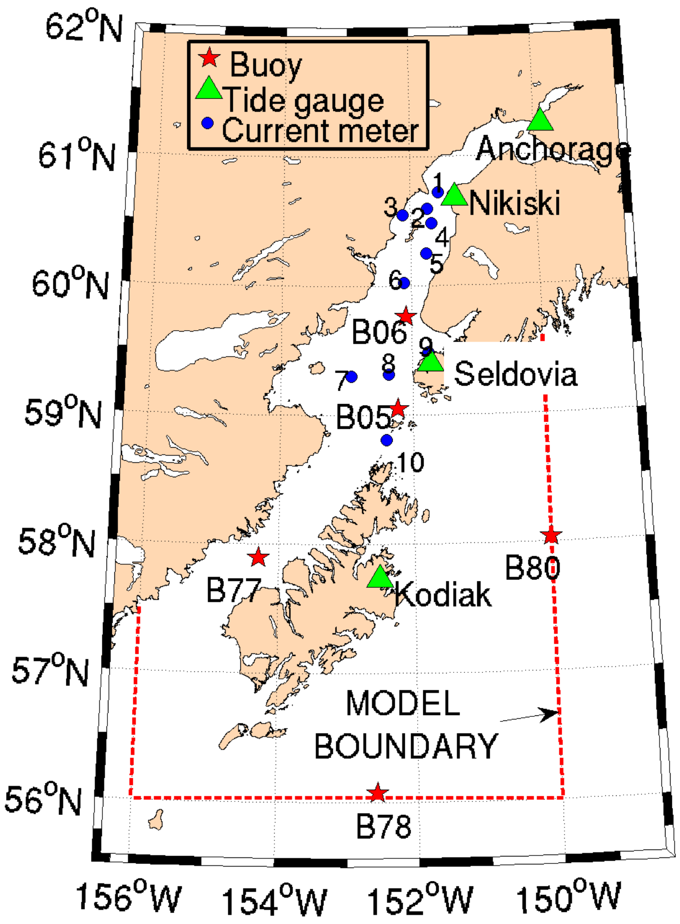

Fig. 8. Circulation model domain (red dashed line) along with data measurement locations. Blue circles represent current measurement locations, red stars represent wave buoys, and green triangles represent tidal gauges.

The CI circulation model was tested via the simulation of tidal conditions for the summer of 2005 (May-August). This period was selected mainly because it coincided with NOAA's comprehensive field campaign of current measurements within CI. Ten locations were selected from this survey for model comparison (current meter locations are shown in Fig. 8). Modeled water surface elevations (WSEs) are also compared with data from four tidal gauges (locations shown in Fig. 8). The model was initiated from motionless conditions on May 1, 2005 via prescription of WSEs and tidal velocities provided at the open model domain boundaries (8 tidal waves were taken into account, namely: M2, S2, N2, K2, K1, O1, P1 and Q1). These boundary tidal elevations and velocities were extracted from TPXO6.2 global satellite-based tidal model (Egbert and Erofeeva, 2002). In addition, discharge from seven major rivers were also inputted to account for the mass distributed by the rivers into the domain (source: USGS). Winds from six land stations and two NDBC buoys were also interpolated on the model grid to account for wind-driven circulation (WRF wind data were not available during 2005).

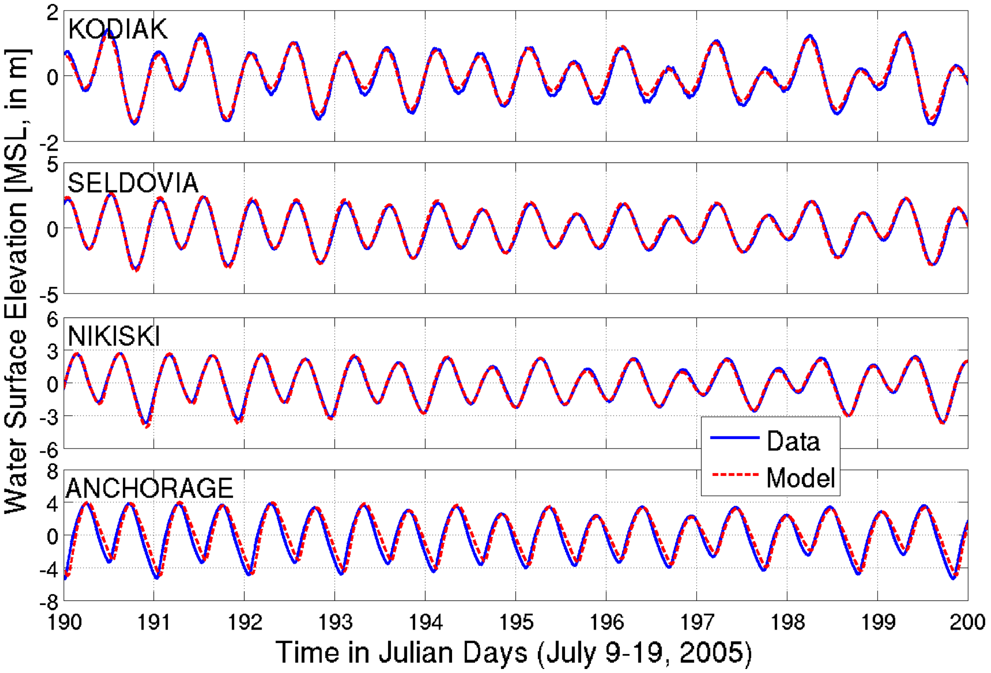

Fig. 9. Comparisons of WSEs at locations of four tide gauges (with respect to MSL, in m).

The model results for WSEs (relative to mean sea level) are shown in Fig. 9. In the north, the tidal range increases from about 3 m at Kodiak Island to roughly 8 m at Anchorage. It can be seen that the model captured the observed tidal variability, which is significant, at all four locations. A more detailed model analysis is shown in Fig. 10, where correlation of predicted WSEs is shown against the observed WSEs. For the most part, the best-fit line (red line) matches the line that represents perfect correlation (slope 1:1; black dashed line) with the exception at Anchorage where the deviation between the two lines seems largest.

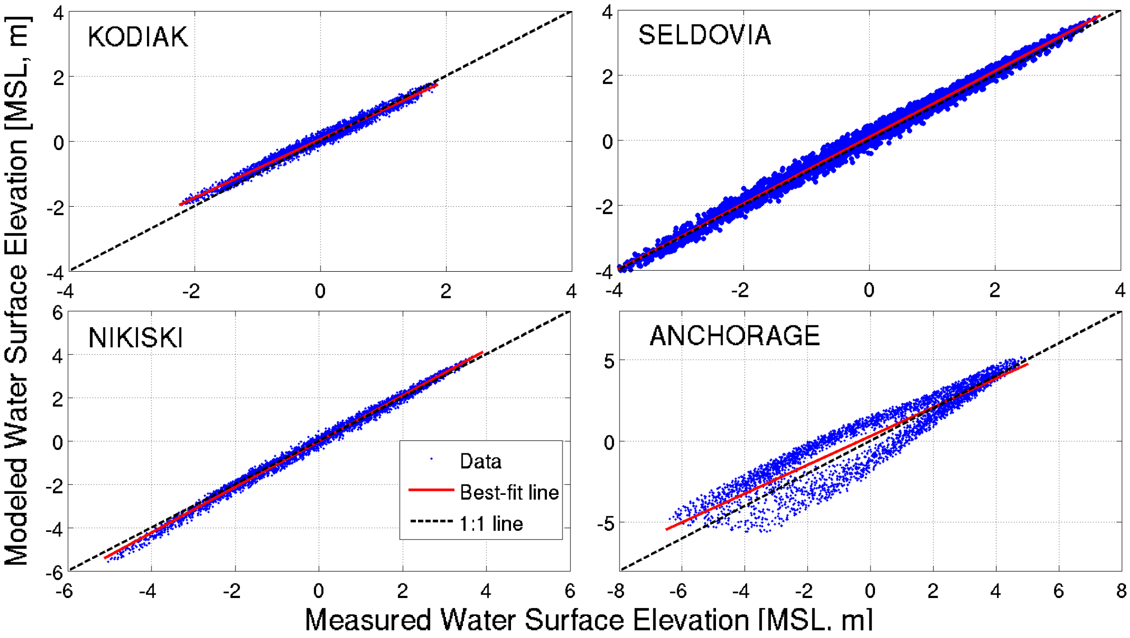

Fig. 10. Correlation of WSEs at locations of four tide gauges (with respect to MSL, in m).

Table 1 shows the summary of statistical estimates of best-fit slopes (m), intercept (c), correlation coefficients (R^2), and root mean square error (RMSE) between model and data. For the most part, the model results correlate with the data to a high degree (values of m and R^2 are in general larger than 0.88 and 0.86, respectively). Results at Anchorage, however, are more scattered compared to those at

Table 1
Statistics of WSE at four tide gauge locations. m is the best-fit slope, c is the best-fit intercept, R^2 is the correlation coefficient, and RMSE is the root-mean-square-error.

Measure	Kodiak	Seldovia	Nikiski	Anchorage
m	0.91	1.01	1.05	0.88
c	0.05	0.08	-0.02	0.28
R^2	0.98	0.99	0.99	0.86
RMSE	0.11	0.15	0.16	0.96
N	3553	3553	3553	3553

other locations and upon further examination, it was determined that although the model predicted the tidal extremes correctly, the model results lagged the data by roughly 30 minutes. The mismatch in the timing of tidal elevations could be due to the coarse 1.5 km resolution of the model grid in the vicinity of Anchorage, which is situated in a narrow, meandering channel in Knik Arm. To check if the resolution was the source of the problem, a finer grid with a resolution of 24 sec (best possible resolution) was constructed near Anchorage (Fig. 11).

The EFDC model was initiated for the finer grid using the boundary conditions from the coarse grid. The results for the two grids are compared with data in Fig. 12, and it can be seen that the timing of the tides using the finer grid near Anchorage is much improved compared to the coarse grid. Fig. 13 shows that the correlation for the WSE comparison also is greatly improved (with $m = 0.96$, $c = 0.06$, $R^2 = 0.99$, RMSE = 0.29).

The nested grid model solution was then checked for its capability in simulating the extent of “dry” regions. A large area in the vicinity of Anchorage becomes exposed during low water conditions (green-shaded area in Fig. 14). It is obviously critical to accurately predict the extent of such regions to aid ship navigation. Fig. 15 shows the model-predicted instantaneous total water depth during low water

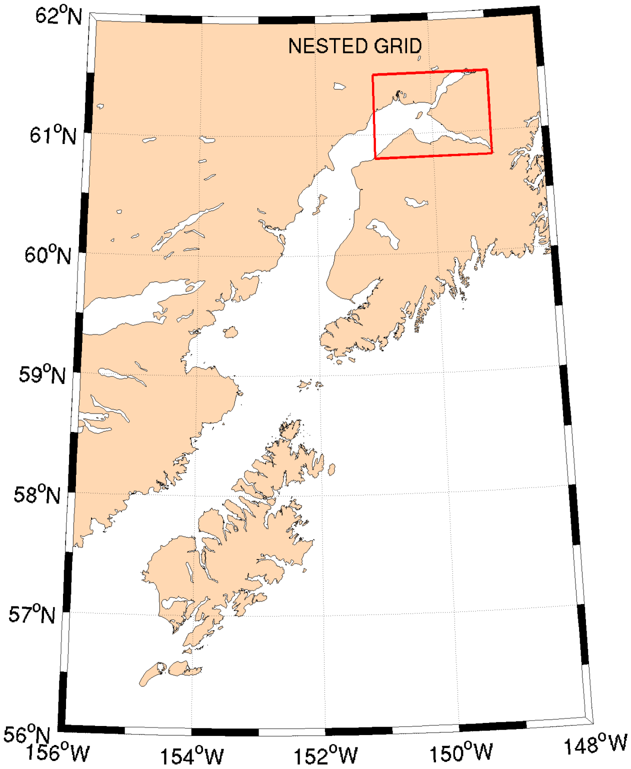

Fig. 11. Nested domain near Anchorage.

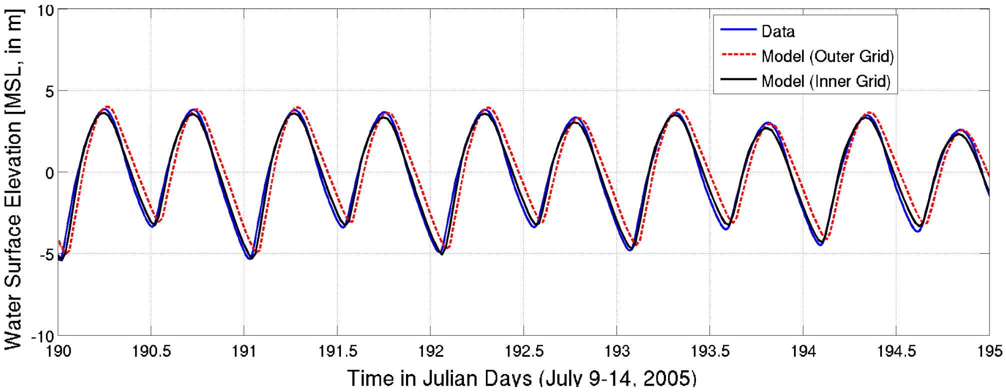

Fig. 12. WSE comparisons at Anchorage.

conditions (inset of Fig. 15). It can be clearly seen that the model-predicted “dry” regions (white patches in Fig. 15) are qualitatively similar to those shown in the NOAA navigational chart (Fig. 14).

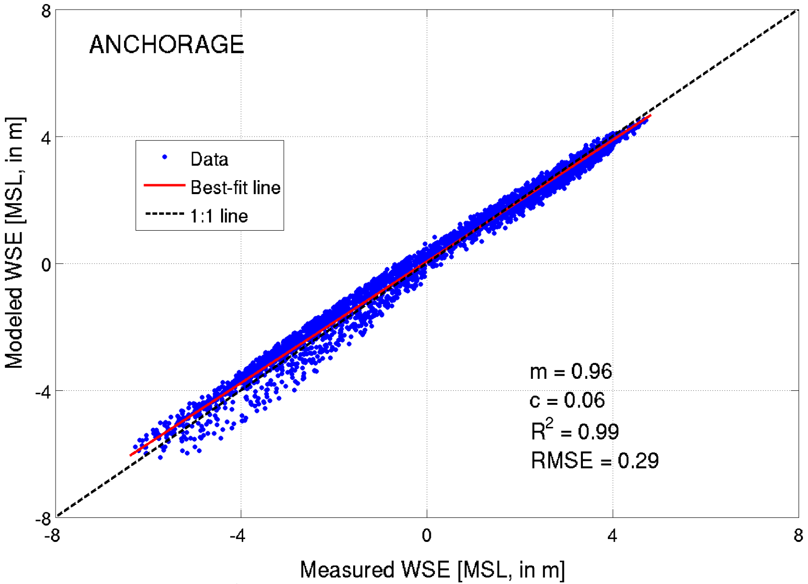

Fig. 13. Correlation of WSEs at Anchorage.

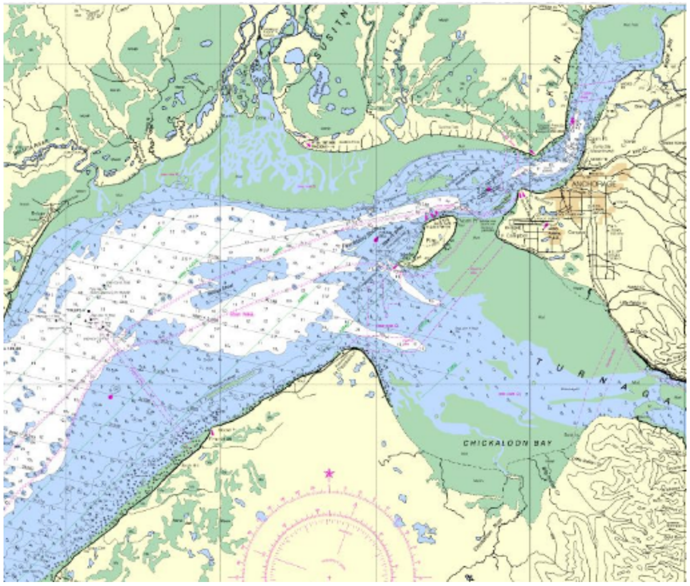

Fig. 14. Map showing the extent of "dry" regions (green-shade) near Anchorage in the northern CI (source: NOAA charts).

Comparison of modeled flow components with the measurements throughout the CI is also shown in Figs.16 and 17 for five locations in the central inlet (CCI) and five locations in the lower inlet (LCI), respectively.

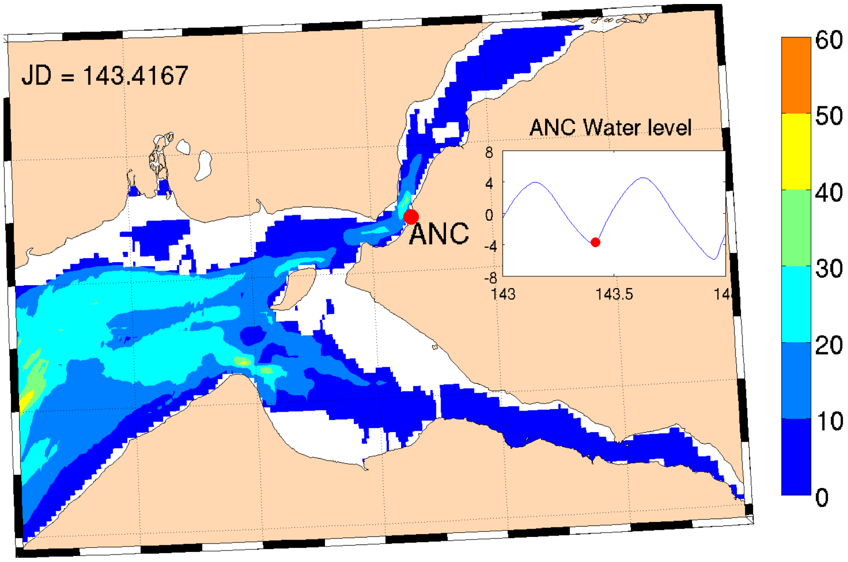

Fig. 15. Model-predicted instantaneous total water depth for the same region as in Fig. 14. White patches depict "dry" regions, whereas inset shows measured (blue) and instantaneous model-predicted (red circle) WSE at Anchorage.

Examination of data suggests that the flow patterns are predominantly tidal in the CCI (blue lines in Fig. 16), whereas a non-tidal flow structure can often be seen in the LCI (e.g. on day 192 near west of Cape Ninilchik; blue line in Fig. 17). This indicates that the tides become more dominant in the north, as opposed to the unsteady wind-/density-driven flow that may have a more pronounced effect in the LCI thereby inducing larger variability in the flow structure. As regards the flow magnitudes, the velocities are higher in the CCI (2-3 m/s) compared to those in the LCI (0.5-1 m/s), with the north-south (N-S) component usually being more dominant than the east-west (E-W) component (although E-W component is larger near Stevenson Passage). Qualitatively, the barotropic model captured the significant tidal variability at all the locations quite well (red line in Figs.16 and 17). While there are occasional mismatches (e.g. E-W flow component west of Kachemak Bay; Fig. 17), for the most part, the model predictions were in close agreement to data.

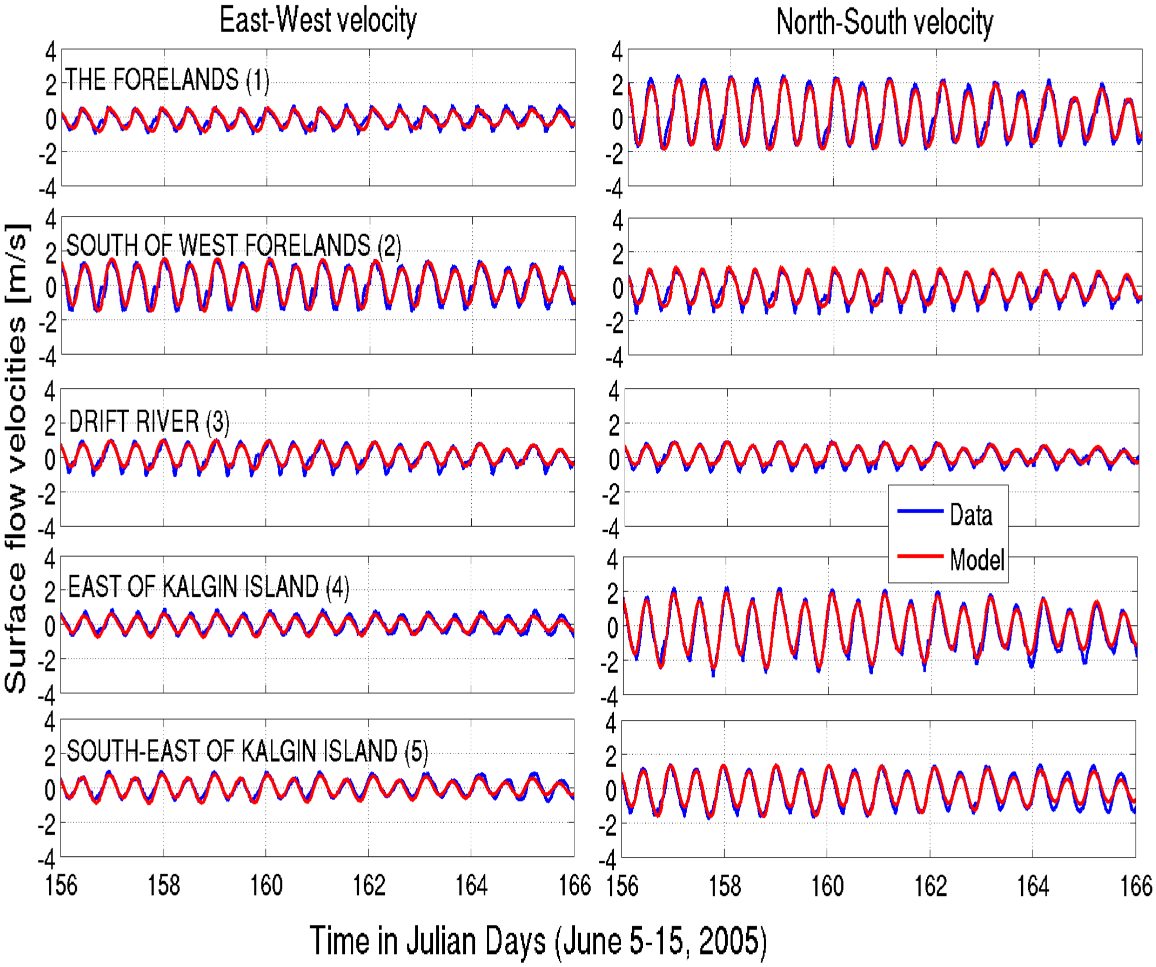

Fig. 16. Comparison of flow velocities (in m/sec) in CCI.

Results were also examined through statistical analysis of E-W and N-S flow components separately (since E-W and N-S flow velocities will be used in the wave model, it is necessary to examine their accuracy separately; see Section 3.6). Comparison with data shown in Fig. 18 and Table 2 indicates that, in general, the model matches all components quite well in the CCI (values of m and R^2 are higher than 0.79). Particularly, the more dominant component (i.e. N-S) is predicted with greater accuracy ($R^2 > 0.8$). The model errors, for the most part, are within 12% of

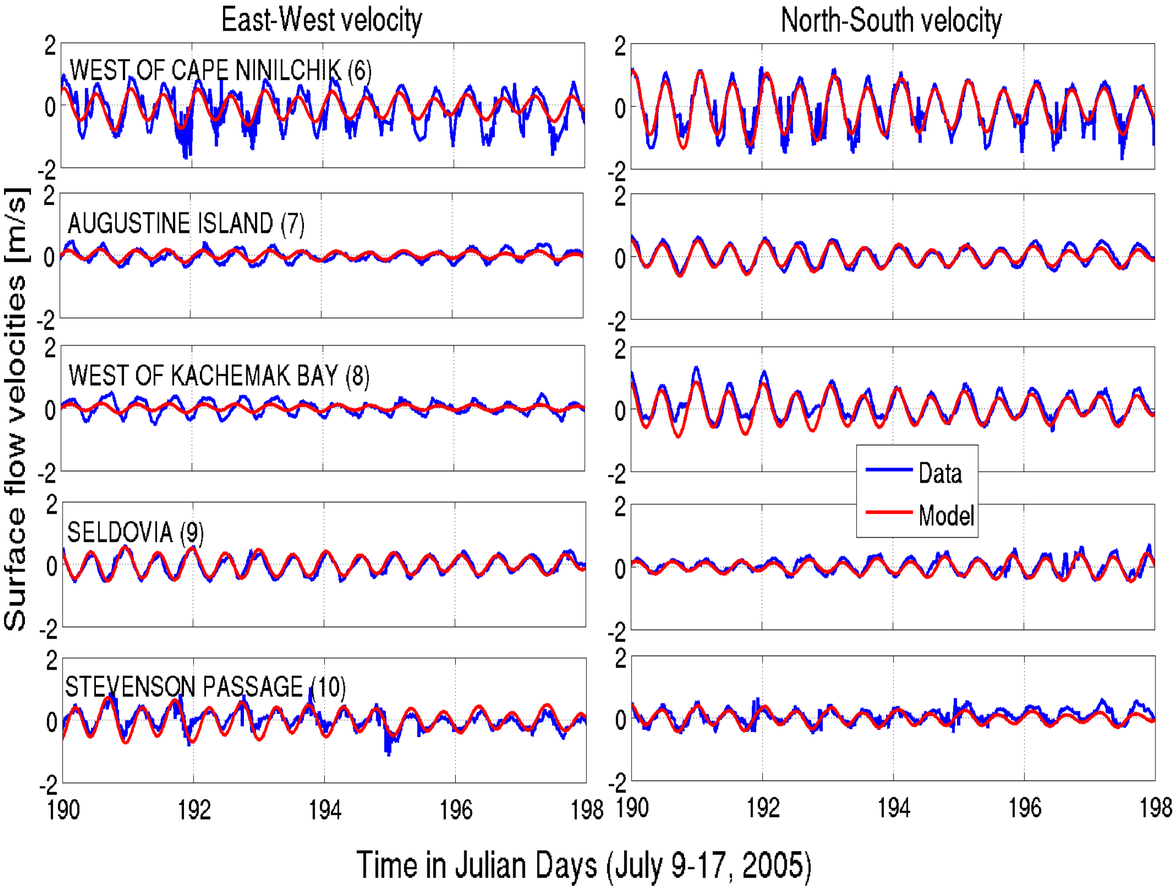

Fig. 17. Comparison of flow velocities (in m/sec) in LCI.

the flow range (RMSE < 0.32 m/s for all components) for the locations in the CCI. It is encouraging that the barotropic model has yielded such a high degree of match, suggesting that the current structure is predominantly barotropic in the CCI.

Moving to the locations in the LCI (Fig. 19 and Table 3), it is also found that the N-S component is generally better predicted (R^2 ~0.8) compared to the E-W component (R^2 ~0.6). In particular, the E-W flow component is under-predicted near Augustine Island and Kachemak Bay (locations 7 and 8 in Fig. 17). The best-fit slopes at these locations are less than 0.42, indicative of greater than 50% under-

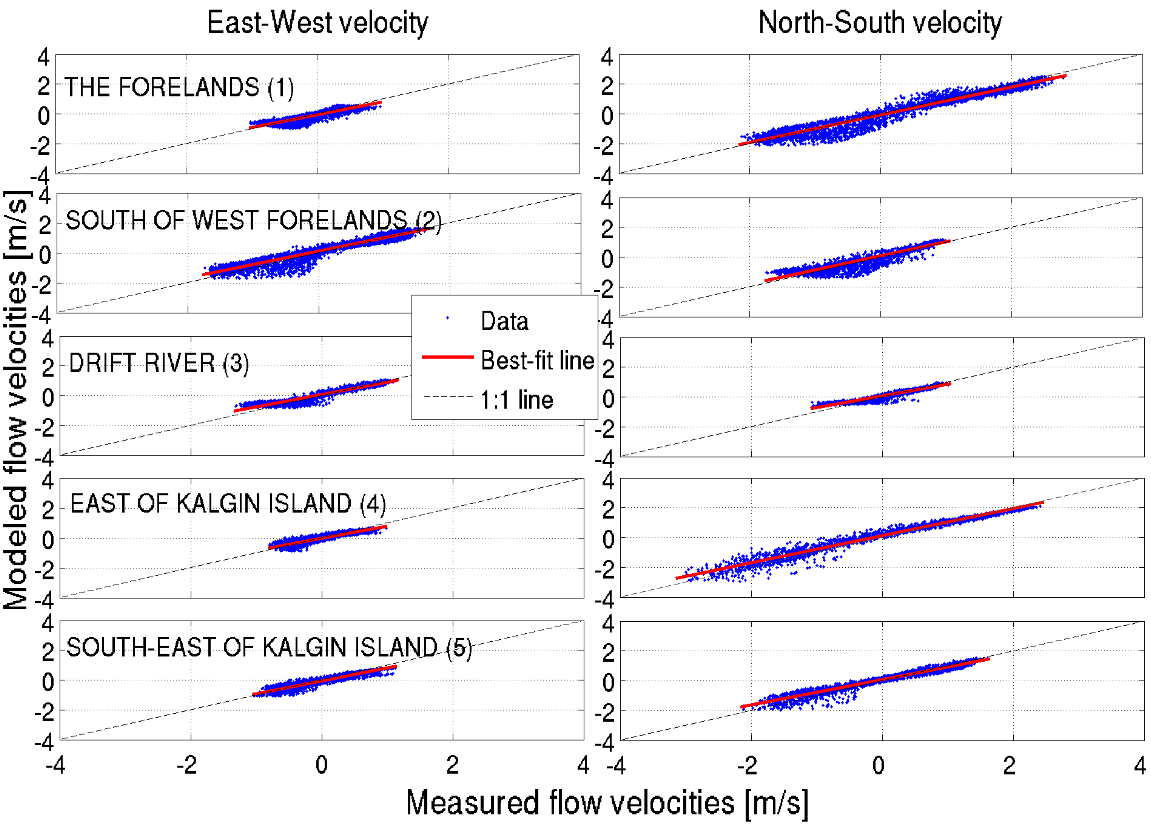

Fig. 18. Correlation of flow velocities (in m/sec) in CCI.

Table 2

Statistics of flow velocities in CCI. L1-L5 represent locations of Forelands, South of West Forelands, Drift River, East of Kalgin Island, and South-east of Kalgin Island, respectively.

	L1		L2		L3		L4		L5	
Measure	E-W	N-S	E-W	N-S	E-W	N-S	E-W	N-S	E-W	N-S
m	0.86	0.93	0.89	0.95	0.83	0.79	0.80	0.91	0.87	0.85
c	-0.06	-0.07	0.09	0.07	0.06	0.06	-0.03	0.11	-0.06	0.06
R^2	0.79	0.94	0.92	0.90	0.92	0.91	0.84	0.97	0.90	0.95
RMSE	0.18	0.32	0.26	0.22	0.14	0.12	0.15	0.22	0.14	0.18
N	2910		2773		1770		1776		1776	

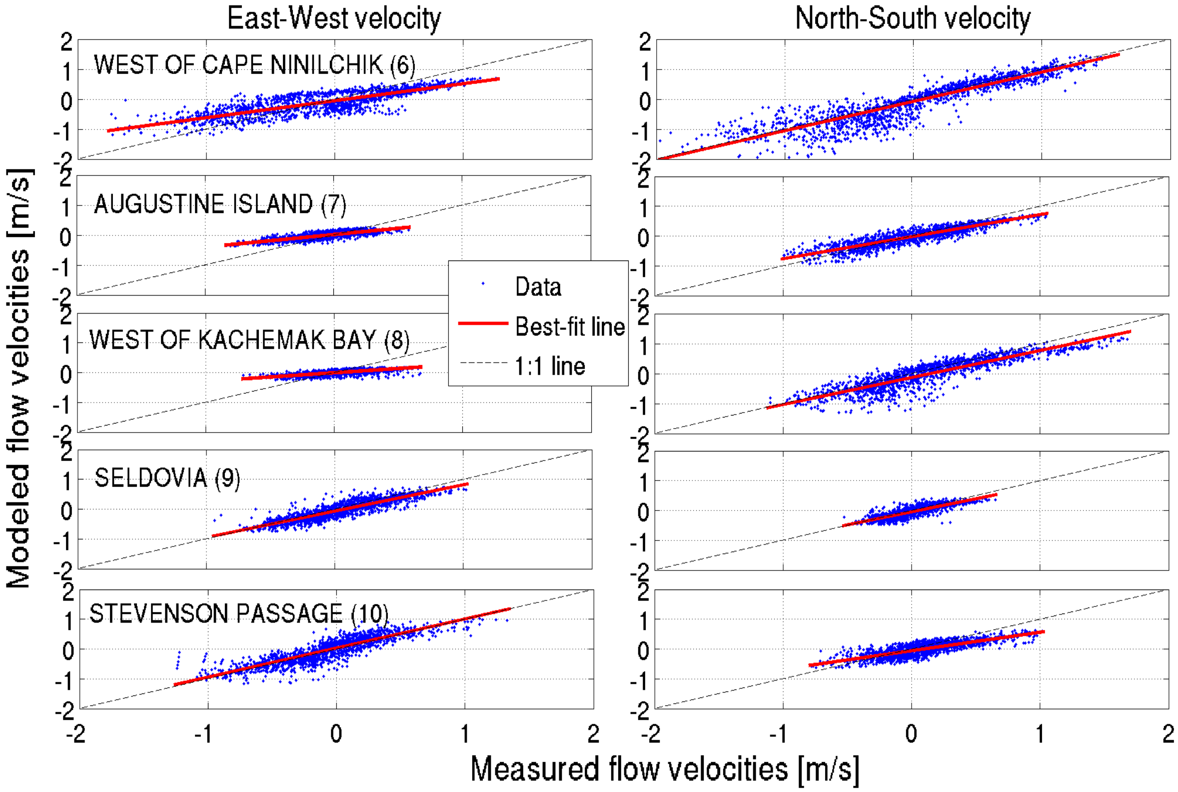

Fig. 19. Correlation of flow velocities (in m/sec) in LCI.

Table 3

Statistics of flow velocities in LCI. L6-L10 represent locations of West of Cape Ninilchik, Augustine Island, West of Kachemak Bay, Seldovia, and Stevenson Passage, respectively.

	L6		L7		L8		L9		L10	
Measure	E-W	N-S	E-W	N-S	E-W	N-S	E-W	N-S	E-W	N-S
m	0.57	0.98	0.42	0.74	0.30	0.90	0.88	0.87	0.98	0.62
c	-0.05	-0.08	0.01	-0.03	-0.01	-0.10	-0.07	-0.05	0.02	-0.05
R^2	0.66	0.85	0.62	0.82	0.55	0.83	0.79	0.80	0.77	0.65
RMSE	0.23	0.28	0.08	0.14	0.06	0.21	0.15	0.09	0.20	0.14
N	1480		1418		1413		1485		1447	

prediction. As discussed earlier, the current pattern at these locations is non-tidal during certain times, which may be caused by a combination of several factors such as the localized wind effect, heat and salt fluxes through Alaska Coastal Current (Okkonen et al. 2009), freshwater discharge through rivers/precipitation, solar radiation, etc. Further to the east of these two locations, near Seldovia (location 9 in Fig. 17), however, the E-W component of the flow is predicted with greater accuracy with values of m and R^2 roughly greater than 0.8. This indicates that the signal is predominantly barotropic and the other effects (ACC, freshwater flows etc.) may not be as prominent in this region.

Overall, the barotropic model used in this study seems to perform reasonably well throughout the CI. The comparison of WSEs and velocities is reasonable at all the locations, with the exception of the E-W flow in certain areas of the LCI. As noted above, the error is perhaps due to the baroclinic effects, which are not accounted for in this dissertation. Since the main goal is to obtain reliable wave estimates, the effect of under-prediction of the E-W flow in LCI on the wave estimates will be addressed later by way of sensitivity analysis (viz. the impact of adding random noise to the currents on predicted SWHs, as a surrogate to actual baroclinic effects, is considered in Section 4.2).

3.5 Surface wave-patterns and modeling

Due to presence of dynamic and energetic weather systems, waves in the northern Gulf of Alaska are among the largest in the world with wave heights frequently exceeding 5m.

For obtaining wave estimates for CI, the SWAN wave model (version 40.81) was utilized. The wave model covered the same region as the circulation model (Fig. 8), but at a resolution of about 1.5 km throughout the domain. SWAN was set up using the default options for wave generation (wind growth, quadruplet, and triad

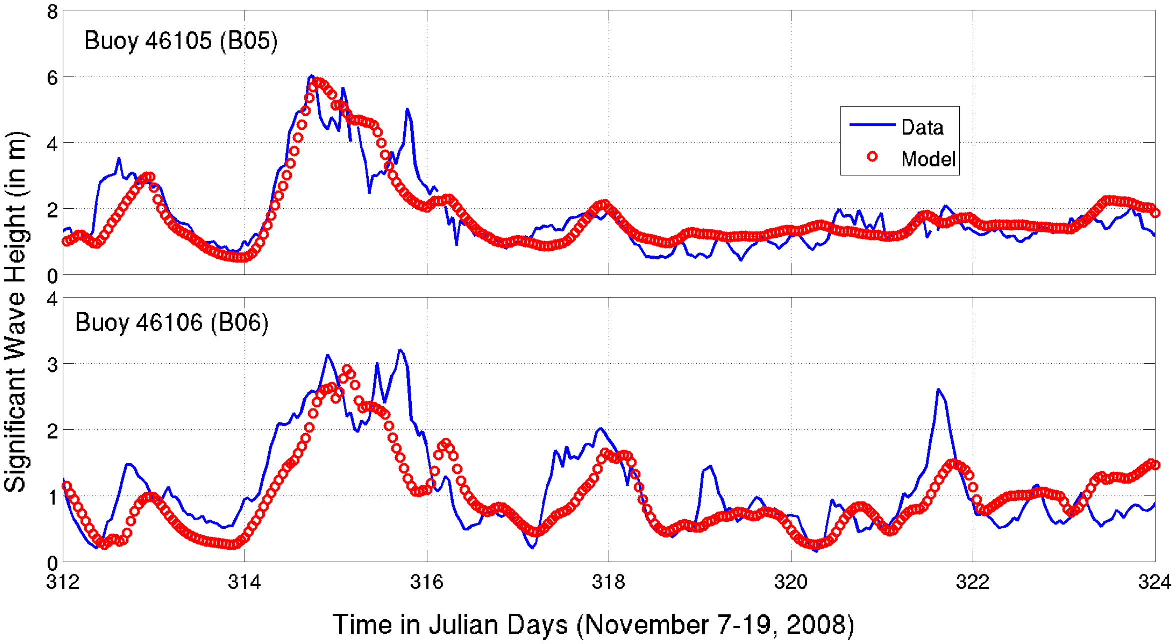

Fig. 20. Sample SWH comparisons at two buoy locations.

wave-wave interactions), wave breaking, friction, etc. A model time-step of 15 min was initially used. The wave model was forced by the WRF model that provided the output of winds every hour at ∼4 km resolution. The open boundary conditions were obtained from the global WW3 model at the locations of Buoy 46078 (hereafter B78) and Buoy 46080 (hereafter B80). The full spectral output at B80 was forced along the east boundary, while the output at B78 was used to force the south boundary. Since the WW3 model, at present, does not provide full spectral output at locations near the west boundary, the output at B78 was also assumed along the west boundary (the validity of this assumption is discussed later).

Sample results obtained using the above model configuration are compared with buoy measurements for B05 and Buoy 46106 (B06) in Fig. 20. The model results match the data reasonably well. For example, the peak SWH (∼6 m) for the event around day 315 at B05 was predicted correctly by the model (top panel Fig. 20). The wave model, in general, seems to capture the variability in the SWHs, although there are some errors which may have arisen from other factors such as winds, offshore boundary conditions, model time-steps, resolution, etc. In addition, there may be some effect due to the currents which were not included in the initial simulations. In the next section, focus is directed towards addressing the effect of wave-current interaction on wave predictions in CI.

3.6 Coupled wave-current modeling

To study the effects of wave-current interaction, the emphasis shifted towards coupling the wave and circulation models. In certain regions of CI (e.g. near the Forelands), the surface-currents are quite strong (2-3 m/s, Fig. 16) and can thus influence the local wave climate. Thus it becomes necessary to develop methodology for coupling the wave and circulation models in order to account for these dynamic processes. In this dissertation, a stand-alone interface - written in Shell scripting language - is developed in order to initiate the cross-talk between the models at appropriate time-steps. The main goals are to identify 1) what level of interaction (one-way or two-way) is needed to achieve reliable results, and 2) whether the wave-current interaction has a significant effect on the overall wave and circulation patterns in CI.

Coupling between the wave and circulation models could be performed two ways - 1) Offline coupling, and 2) Online coupling (commonly used terminology when coupling earth system models). In general, offline coupling entails running the two models separately (in no particular order) for the entire duration of simulation (e.g. two days). The information can then either be transferred from one model to the

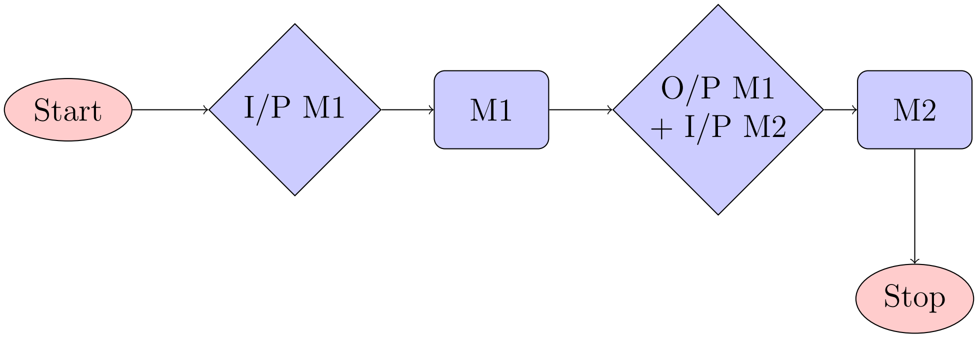

Fig. 21. Offline coupling with one-way approach. M1 represents Model 1, whereas M2 represents Model 2. I/P is input, O/P is output.

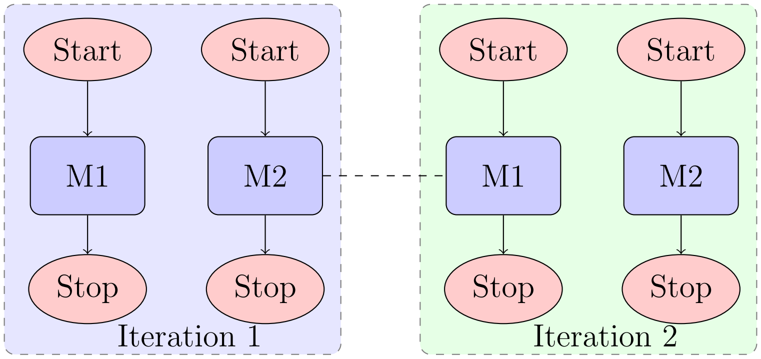

Fig. 22. Same as Fig. 21 but with two-way approach involving two iterations.

other model (one-way approach; Fig. 21), or it could be exchanged among both the models (two-way approach; Fig. 22). In the one-way approach, the second model is executed using the output of the first model (Fig. 21), whereas the two-way approach requires both models to be executed multiple times, while exchanging information, until the solution is converged (Fig. 22).

Online coupling, in contrast, invokes both models simultaneously. After a suitable time interval (e.g. three hours), the two models exchange information and continue the simulation until the next communication time step (Fig. 23). This technique avoids the use of multiple iterations as there is dynamic exchange of information among the two models during the simulation process. However, in between two

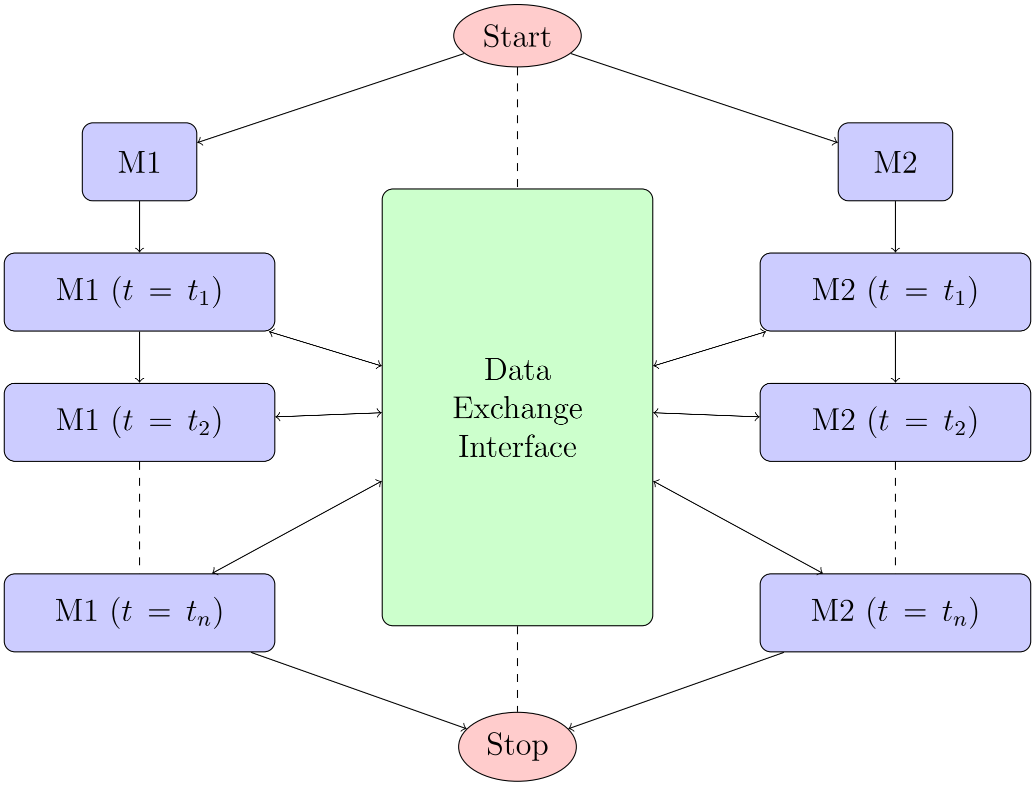

Fig. 23. Online coupling of two models.

information exchange time-steps, the conditions are assumed steady. In contrast, in the one-way approach, the required information at all time-steps from the other model is precalculated. Thus there are advantages and disadvantages associated with both the methods and the effects of these on the model accuracy and efficiency must be investigated.

In the context of the present work, the coupling of SWAN and EFDC was performed on a Macintosh computer with Quad-core processor (with hyper-threading) and 16 GB RAM. SWAN can run in parallel mode for multi-processor systems, whereas EFDC is only capable of running in serial mode. In this dissertation, one-way offline coupling (hereafter, OFC) and online coupling (hereafter, ONC) are used to study the effects of wave-current interaction. The purpose of using the two methods is to compare the wave model results with and without any coupling, and to address which method is more efficient for forecasting purposes.

In OFC, the simulation is started with EFDC which provided output of WSEs and surface-currents. SWAN was then initiated with the EFDC output along with the other forcing terms (winds, boundary conditions etc.). For ONC, a simple interface was built using the shell scripting language. This interface controlled the execution of both the models simultaneously - starting from t = 0, each model advances to the so-called "information exchange" time step when the models are stopped momentarily to exchange information (gradients of radiation stresses are transferred from SWAN to EFDC, whereas water-levels and currents are transferred from EFDC to SWAN), after which the models continue the simulation until the next "information exchange" time-step, and so on. Thus, each model has information about the other model after each exchange, which is assumed steady till the next exchange. The results from the two coupling methods were compared to the results without any coupling. The coupled results are also inter-compared for different updating intervals. Two updating intervals - 1H and 3H - are selected for this comparison. In 1H OFC, EFDC output is transferred to SWAN on hourly-spaced time-steps, and in 3H OFC, the same is done every 3 hours. In ONC, information among the two models is exchanged every hour using 1H and every 3 hours using 3H.

3.7 Results: Application of coupled wind-wave-current modeling

The development of the integrated wind-wave-current model is guided by its performance during four storm events. These occurred over a two-week period in October 2008. The measured wind and wave conditions during these events near B05 are shown in Fig. 24. Fig. 24a,b show SWH and mean wave direction respectively,

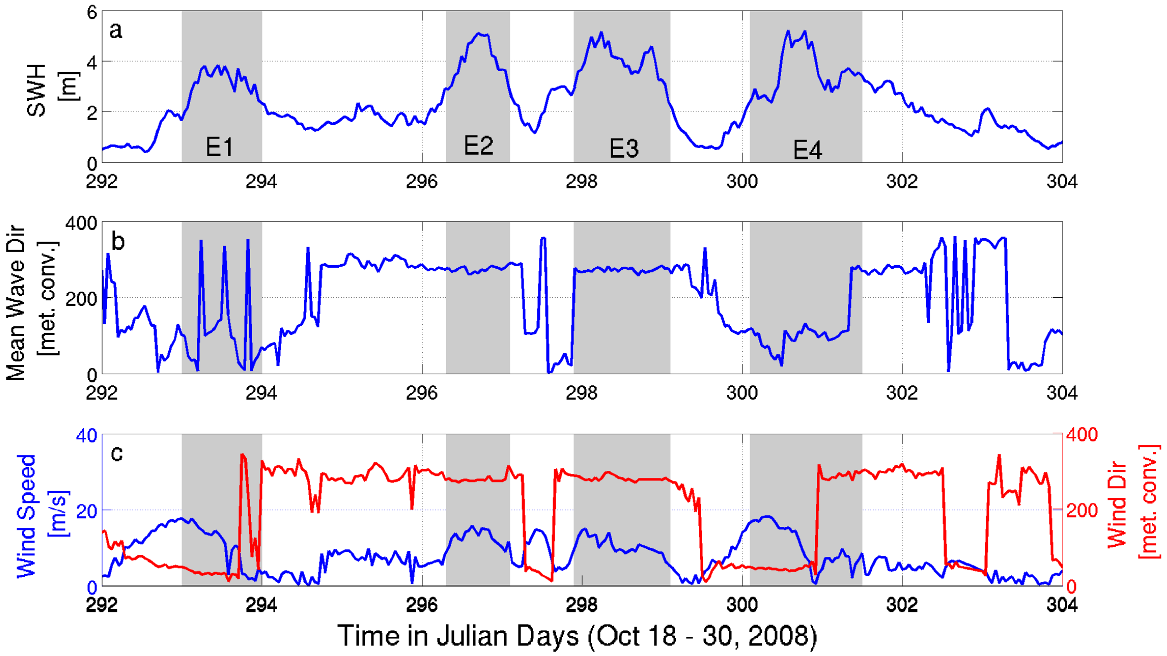

Fig. 24. (a) SWH (in m) and (b) Wind Speed (in m/sec) measured at B05, (c) Wind speed (blue) and direction (red) measured at Augustine Island weather station.

whereas Fig. 24c shows wind speed and direction measured at Augustine Island (a weather station 40 nm north-west of B05; B05 is not equipped with anemometer for measuring wind). For convenience, the four events are named as E1, E2, E3, E4.

The large waves with SWH ~5 m during E2 and E3 appear to be coming from the west (Fig. 24b), which is consistent with the dominant wind direction (Fig. 24c red line). On the contrary, waves during E4 appear to be coming from the east-south-east direction (i.e. from Gulf of Alaska). Waves during E1 exhibit greater variability and are northerly for the most part. Although the SWHs for all the events are quite large, they may be generated by different physical mechanisms (e.g. local winds funneled by the surrounding Chugach Mountains, swells from Gulf of Alaska, etc.). In summary, these events were selected because 1) of the magnitude of these events (i.e. SWHs $>$ 4m), 2) of their distinct characteristics discussed above, 3) of the availability of buoy measurements to guide the model development and validation, and 4) such events can serve as benchmarks for quantifying modeling errors for future events.

In the following discussion, qualitative (Section 3.7.1) as well as quantitative (Section 3.7.2) analyses of the various coupled approaches are presented.

3.7.1 Qualitative analysis of coupled schemes

The qualitative results of the coupled modeling schemes are presented in this section. For convenience, the entire CI domain is divided into three regions: lower inlet (LCI), central inlet (CCI), and upper inlet (UCI).

A snapshot of the modeled wind and wave conditions during event E4 (on 10/26/08 2300 UTC; i.e. day 300.9583) is first shown in the CCI region (Fig. 25). Initially, the wave model was not coupled with the circulation model. The winds and waves during this time were mostly southward with wind speeds around 12-14 m/s and the modeled SWH ~1.5-2 m. The peak wave period ranged between 5-6 seconds in this region, reminiscent of the short period seas generated by local winds.

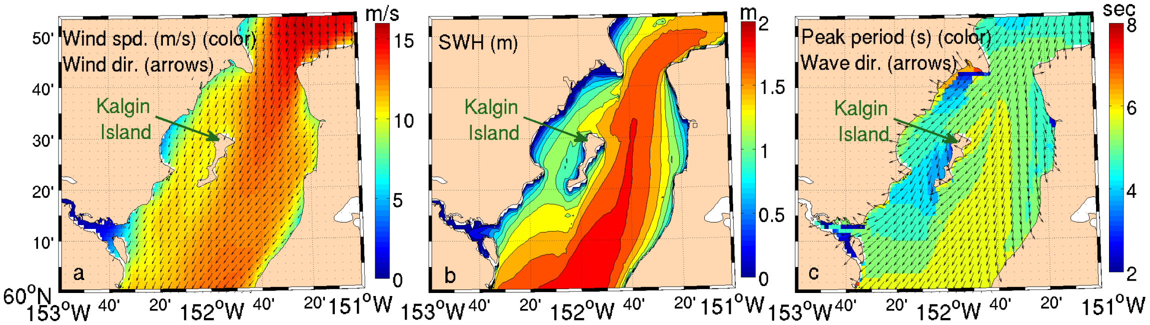

Fig. 25. Snapshot of modeled sea-conditions (without coupling) in CCI region on 10/26/08 2300 UTC: (a) Winds, (b) SWH, (c) Peak wave period and wave direction.

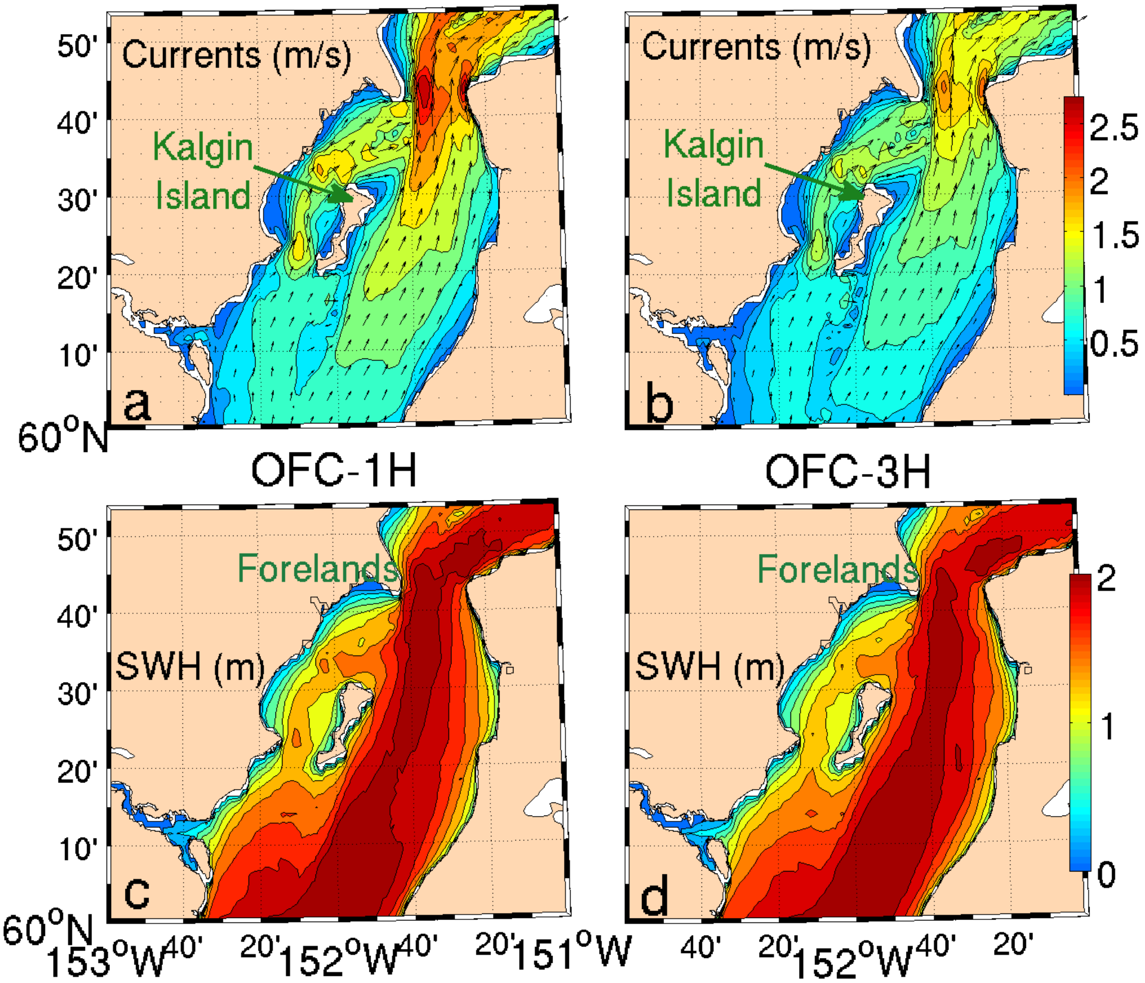

Fig. 26. Snapshot of modeled sea-conditions (with OFC) in CCI region on 10/26/2008 2300 UTC. Left panels show results using 1H interval, whereas those on the right are for 3H interval.

To assess the influence of the currents on the waves, the wave model was then coupled with the circulation model using the two coupling methods (i.e. OFC and ONC) with 1H and 3H updating intervals. Fig. 26 shows a combined plot of wave and current conditions using OFC (1H, 3H) on day 300.9583 (same time as Fig. 25). Contrary to the wind-wave direction, the current direction was northward with maximum speed of about 2.5 m/s near Forelands (contricted area near the top of Fig. 26). This flow direction corresponds to the flood current when tide is propagating northward in the domain. Compared to the SWHs obtained without any coupling (Fig. 25b), the SWHs obtained using OFC-1H (Fig. 26c) are, on average, 0.4-0.5 m higher near Forelands due to the effect from a strong opposing current. The results obtained using 3H updating interval (Fig. 26d) are smaller by about 0.1-0.15 m to those obtained using 1H interval near Forelands. This discrepancy can be addressed by observing the surface-current patterns using 1H and 3H updating intervals (Fig. 26a,b). It is found that the intensity of currents with 3H interval is smaller by about 0.5-0.6 m/s compared to 1H interval. This is mainly because SWAN interpolated currents between days 300.875 and 301 (which yields the currents shown in Fig. 26b) to estimate wave conditions on day 300.9583, as opposed to OFC-1H when current information on day 300.9583 was available to SWAN. This shows that the tidal conditions change frequently in the domain, and the OFC-1H approach seems to capture such features better than the OFC-3H approach. Nevertheless, these results - which are qualitatively consistent with our expectations given the directions of the waves and currents - inspire confidence in the used modeling scheme.

SWHs obtained using ONC (Fig. 27) seem to follow similar overall trend, with SWHs about 0.4 m higher than those obtained without any coupling. For the most part, the SWH results of ONC-1H (Fig. 27c) are similar to those obtained using OFC-1H (Fig. 26c), with minor differences of < 0.1 m in some regions. Results obtained using ONC-3H, however, show differences upto 0.25 m (compared to OFC-1H) near Forelands. This could be traced again to the flow magnitudes in ONC-3H (Fig. 27b), which shows that the intensity of flood current was smaller by about 0.5 m/s compared to that in ONC-1H (or OFC-1H). This is because in ONC-3H, the information exchange occurred on day 300.875 and the wave model assumed the

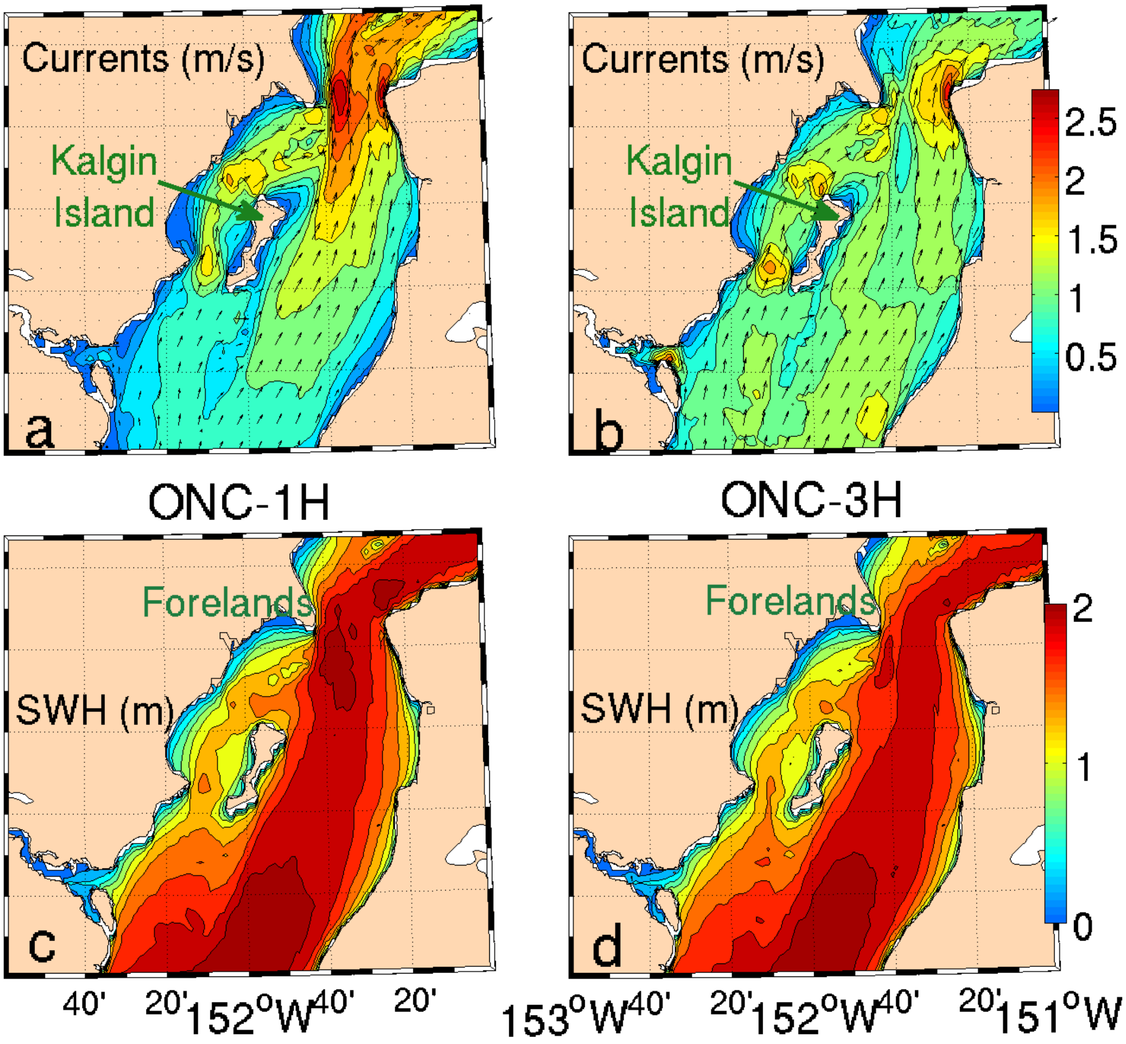

Fig. 27. Same as Fig. 26 but for ONC.

currents to be steady until the next 3H (i.e. from day 300.875 to 301). In contrast, the wave model used the actual current speed on day 300.9583 (time of conditions shown in Figs. 25-27) in OFC-1H (or ONC-1H) approach.

Overall, the differences in the SWHs ($\sim$ 0.5 m or about 30% change) with and without coupling clearly indicate that some coupling (one-way or two-way) is necessary in the CCI. Both OFC-1H and ONC-1H approaches seem to capture the rapidly changing tidal conditions better compared to OFC-3H and ONC-3H counterparts. With regard to the efficiency of the system, it was found that the OFC approach was more efficient compared to the ONC approach (a 2-day simulation using OFC-1H took about 2H, whereas with ONC-1H the same simulation took about 3H). It was also found that the reverse feedback from SWAN to EFDC (through gradients of wave radiation stress in ONC) had only a marginal effect on the circulation model results (about 2-3 cm/s). Thus the ONC approach may not be warranted. In the following discussion, results obtained using only OFC (i.e. one-way offline coupling from EFDC to SWAN) are presented.

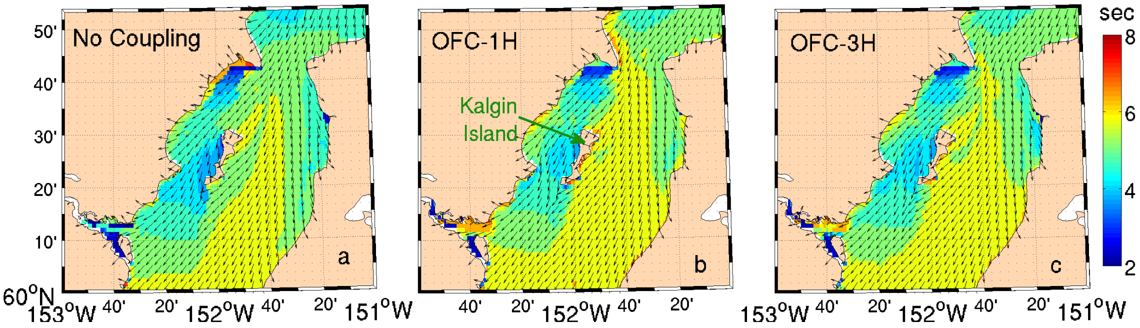

Fig. 28. Comparison of peak wave period (color) and wave direction (arrows) with (a) no coupling, (b) OFC-1H, (c) OFC-3H during the same time as in Figs. 25-27.

As to the peak wave periods and wave directions, Fig. 28 shows that the effect of wave-current interaction on these quantities is not large. For the most part, the peak wave period increased by about 1 sec to the east of Kalgin Island (colors in Figs. 28b,c) in the presence of currents.

Moving to the LCI region, Fig. 29 shows the current patterns (top panels) and the difference in SWHs with and without OFC coupling (bottom panels). The maximum

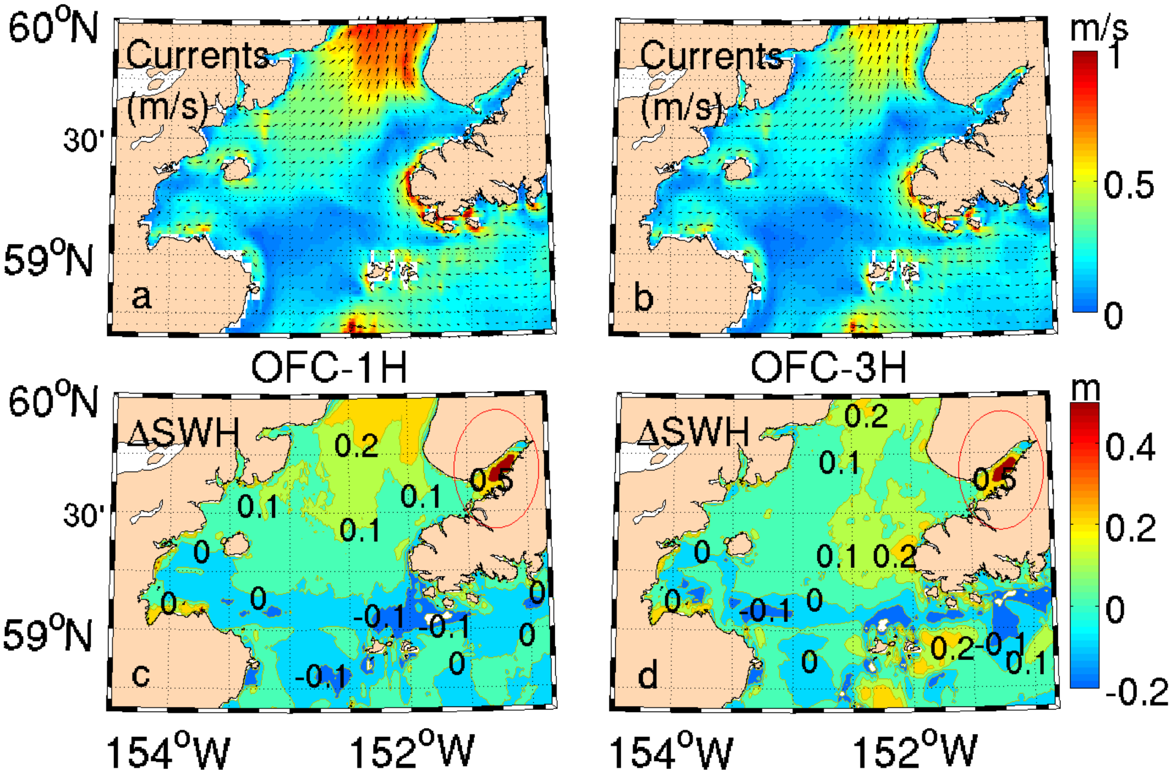

Fig. 29. Modeled sea-conditions in LCI for the same time as in Fig. 28. (a),(b) Currents and (c),(d) Difference in SWH with and without coupling for OFC-1H and OFC-3H, respectively. Red elliptical region marks Kachemak Bay area.

currents are found in the northern parts (Fig. 29a,b) and are on the order of 1 m/s (compared to upto 2.5 m/s in CCI region; Fig. 26a). Elsewhere, the currents are mostly smaller in magnitude (< 0.5 m/s). As to the pattern in the wave heights, in the northern parts, the SWHs show an increasing trend (Δ SWH>0) with maximum increase of about 0.2 m (Fig. 29c,d), since the currents were flowing opposite to the predominant wave direction. In the southern-parts, however, the SWHs show a decreasing trend (Δ SWH$\leq$0) because the currents were rather sluggish, and mostly flowing in the same direction as the waves. Differences are also evident among the OFC-1H and OFC-3H results. As noted earlier, these differences are mostly due to the choice of updating interval of currents in the wave model. Overall, these trends are again consistent with our expectations and the results seem reliable.

A more interesting feature was found in the eastern reaches of Kachemak Bay region (red ellipse in Fig. 29c,d), where the SWHs increased by over 0.5 m. It was found that, without the currents, this region showed no wave development and SWHs were quite small (<5 cm). However, with the inclusion of currents, waves penetrated further to the east and resulted into waves about 0.5-0.6 m high. However, this finding is preliminary and given the complexity of this region, model grid refinement may be needed to fully understand the coupling effects which may also include flooding and drying (this is discussed in Section 5.3).

Moving to the north, Fig. 30 shows the wave- and current-patterns for the UCI region (same time as previous figures). A couple of things stand out: 1) current speeds in OFC-1H and OFC-3H differ by as much as 1 m/s, and 2) the extent of dry regions (white spaces). The longer updating time interval appears to be affecting this region the most. The OFC-3H result shows waves in regions that are actually "dry" in OFC-1H result (Figs. 30c,d). This discrepancy again is a result of time-interpolation in OFC-3H that misses the minute details associated with the rapidly changing tidal conditions, particularly in the UCI region where tidal range is quite large (∼8 m). Apart from the mismatch in the prediction of "dry" regions, ΔSWH patterns using OFC-1H and OFC-3H are mostly similar. The largest differences of upto 0.5 m are found on the western boundary.

A composite statistical analysis was then performed over the entire domain to estimate the average and extreme differences between the modeled SWHs with and without the currents. For this analysis, only OFC-1H was considered. First, a composite map of time-averaged SWHs for the two-week simulation period is shown

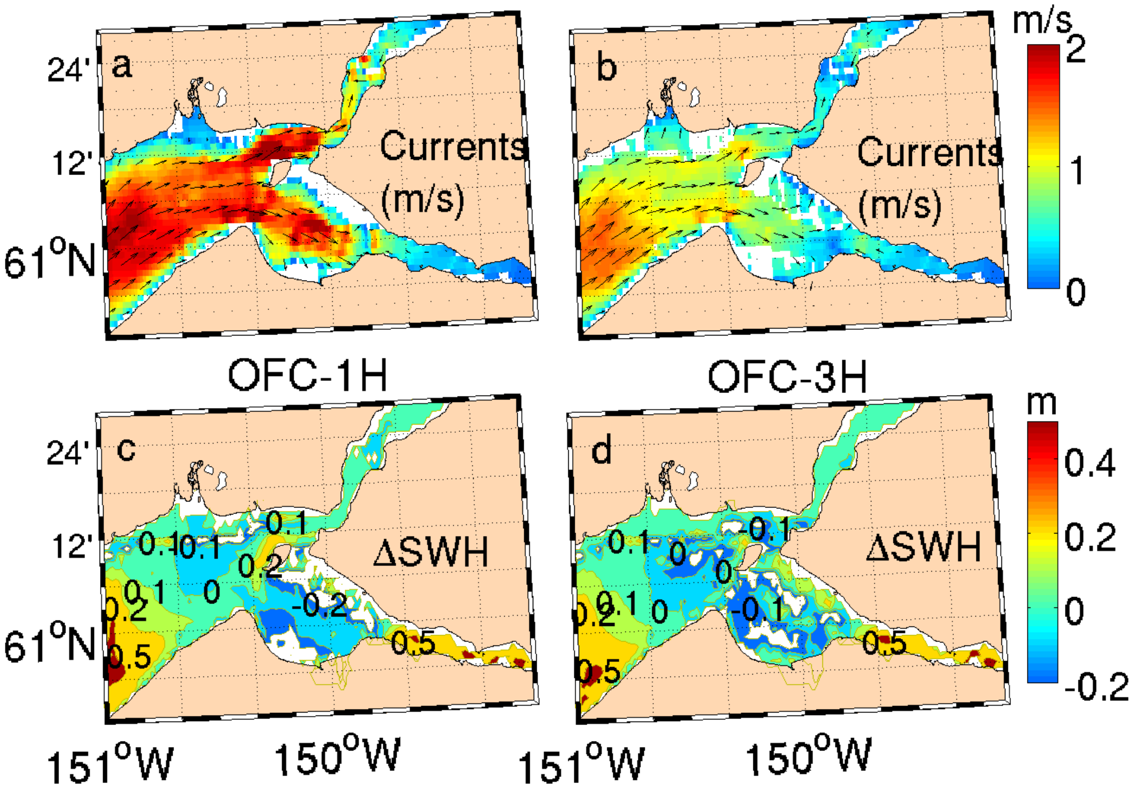

Fig. 30. Same as Fig. 29 but for upper CI. Note that white spaces denote dry regions.

in Fig. 31 to serve as the reference for comparing other statistics. On average, SWHs decrease from about 2.5 m at the CI entrance to about 1 m in the UCI region.

To compute the mean/extreme statistics, the modeled SWHs obtained without the inclusion of currents were first subtracted from those obtained with the currents at each grid point for each time-step. The result was then time-averaged to obtain the mean statistics. The following equation describes the computation of mean difference at each grid point:

$$\langle\Delta_{(i,j)}\rangle = \sum_{k=0}^{N}\left(\frac{H_{c}{}_{(i,j)}^{k} - H_{o}{}_{(i,j)}^{k}}{N}\right) \tag{12}$$

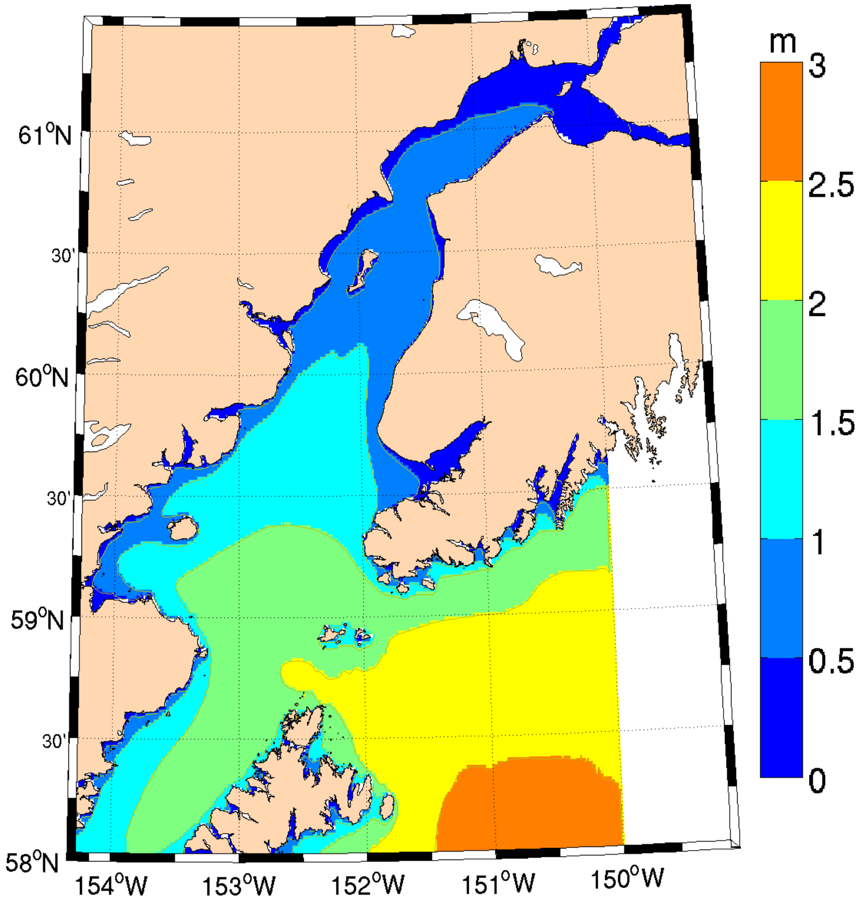

Fig. 31. Composite map of time-averaged SWHs for the two week period.

where $\langle \Delta_{(i,j)} \rangle$ is the time-averaged difference with i, j denoting the grid indices; k is the time index; H_c and H_o denote the SWHs obtained with and without the currents, respectively.

The results of mean statistics obtained using Eq. 13 are shown in Fig. 32. The mean SWH difference estimated over the two-week period is of the order of ± 0.2 m, with the largest differences found near Homer ($\sim$ +0.1 m), Kalgin Island ($\sim$ -0.15 m), and north of Forelands ($\sim$ +0.15 m). There is also a net increase in SWH (upto 0.1 m) near Kennedy Entrance, Stevenson Passage (denoted by KE and SP in Fig.

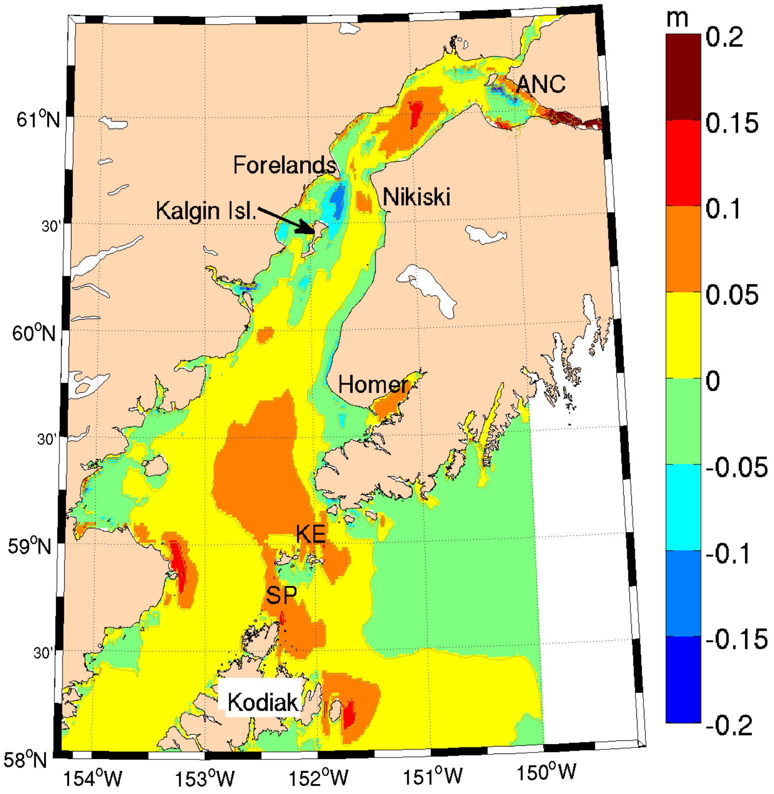

Fig. 32. Map of time-averaged difference in SWHs with and without the currents for the two week period.

32, respectively), and eastern side of the Kodiak Island. The most striking features are found at the constriction between Forelands and Nikiski where the mean SWHs decrease in the west (-0.15 m) and increase in the east (+0.1 m). These numbers correspond to about 10-15% variation in the mean SWHs (which were in the range 0.5-1 m without wave-current interaction; Fig. 31).

Although the above statistics provide an insight into the mean variations, estimation of extreme values are more important in the context of engineering applications. Thus, further analysis was performed to map the extreme variations due to the wave-current interaction in the CI domain. In particular, the maximum increase and

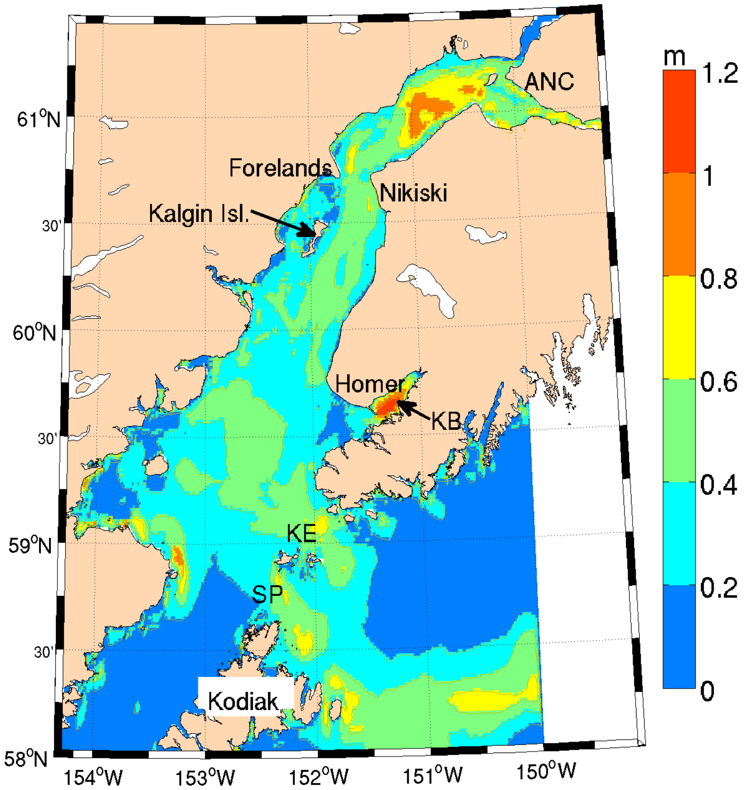

Fig. 33. Map of maximum increase in SWHs at each grid point in presence of currents for the two week period.

decrease in SWHs were estimated at each grid point during the two-week period. Fig. 33 shows the maximum increase in SWHs, whereas Fig. 34 shows the maximum decrease in SWHs in the presence of currents. The maximum increase stands out in two regions, viz. Kachemak Bay (denoted by KB) and north of Forelands, where SWHs increase by upto 1 m (Fig. 33), corresponding to greater than 50% increase without the currents. In contrast, the maximum decrease in the SWHs (-1 m) are found in the region east of the Kalgin Island (Fig. 34), corresponding to about 30% decrease without the currents. Near Nikiski, SWHs show a maximum increase ($\sim$ +0.6 m), whereas a maximum decrease in SWHs are found near Forelands ($\sim$ -0.5m).

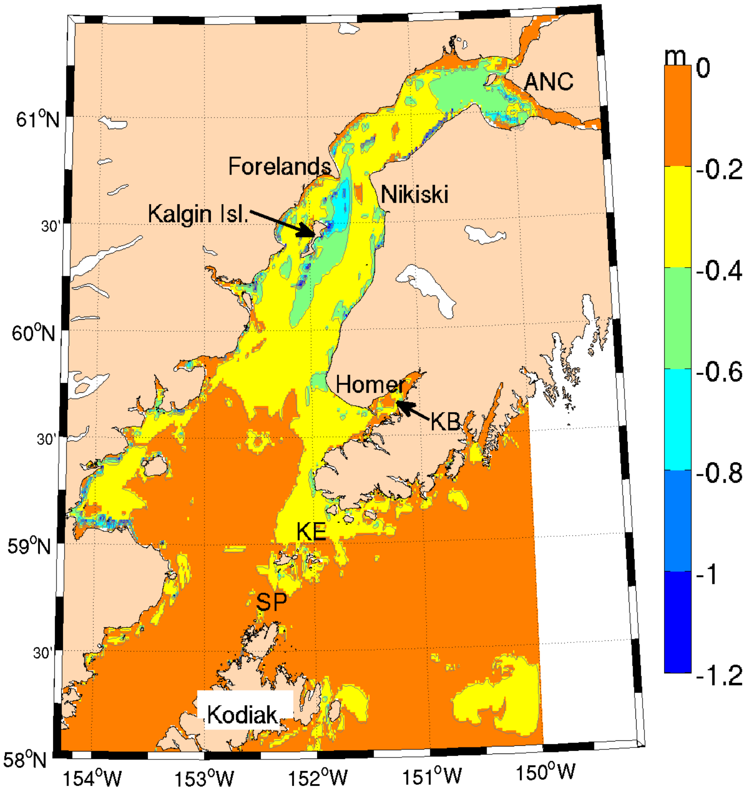

Fig. 34. Map of maximum decrease in SWHs at each grid point in presence of currents for the two week period.

This contrasting trend was also found in the mean statistics, which suggests that the directionality of currents has some phase lag along the east-west transect near the constricted region. Overall, plots shown in Figs. 32-34 show regions with extreme variations in SWH in the presence of currents. In other words, these maps depict the "worst" possible situation that may arise due to wave-current interaction.

The question, then, becomes: "How many times can one expect such large SWH variations in the presence of currents?". To that end, the probabilities of the SWH difference (i.e. ΔH_s) to exceed a particular bound were estimated. In particular, the bounds were chosen to be 10%, 20%, and 30% (Fig. 35). This analysis was done

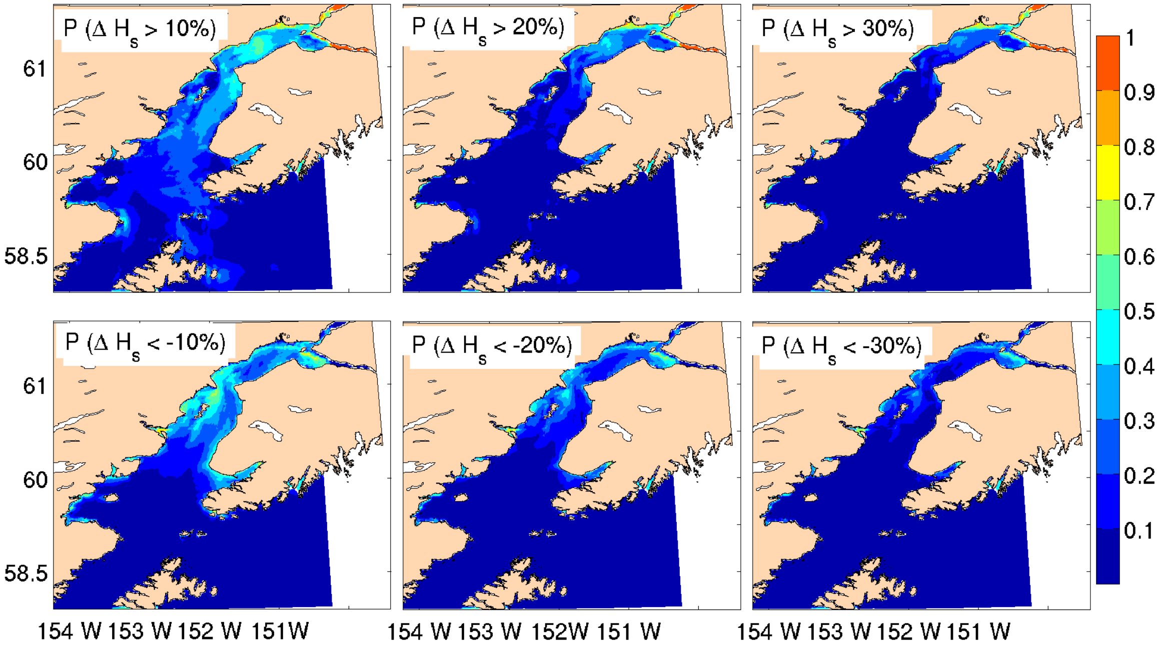

Fig. 35. Map showing probabilities of the difference (ΔH_s) to exceed a particular bound, e.g. 10%, 20%, and 30%.

for the two week period as noted earlier. It can be seen that there is greater than 50% chance for the SWHs to increase by >10% in the northern CI (Fig. 35, top left panel). As the bounds are increased (e.g. 20%, 30%), the probabilities are still higher (~30-40%) in the northern CI, however the extent of exceedance is smaller. Near Kalgin Island, it was found that there is about 50% chance for the SWHs to decrease by more than 10% in the presence of currents. Again, as the bounds are increased, the higher probabilities (~50%) are limited to much smaller regions.

The maps shown above could be used for a variety of engineering applications such as ship routing, navigation, and oil spill planning. For instance, maps shown in Fig. 35 suggest that ships sailing northwards into CI should take the region slightly to the east of Kalgin Island in order to avoid regions with strong wave-current interaction. Such maps can also be used to guide future deployments of wave gauges at various locations not only to validate the modeling study undertaken in this dissertation, but also to better understand the effects of wave-current interaction in a dynamic natural environment.

3.7.2 Quantitative analysis of coupled schemes

The model performance was then evaluated with and without coupling against data from B05 and B06 (Fig. 36). There are small differences between the results of all the coupling methods (i.e. OFC-1H, OFC-3H, ONC-1H, ONC-3H), but overall they follow a similar trend at both the locations. As also found in the qualitative assessment earlier, ONC does not seem to show large differences from OFC which further justifies the use of OFC only. Also, the discussion in the previous section

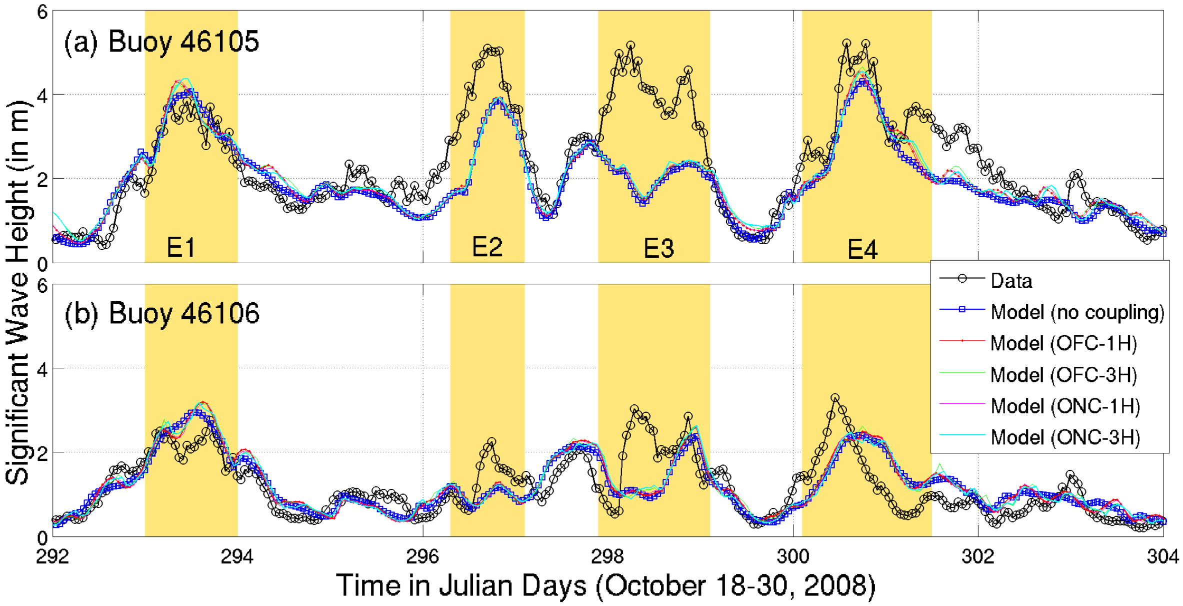

Fig. 36. SWH comparisons of different modeling schemes to data from (a) B05 and (b) B06 for the two-week period.

suggests that OFC-3H is unable to capture the rapidly changing tidal conditions, and hence only OFC-1H is utilized.

As to the inter-comparison with data, the coupled results closely follow those obtained without coupling (squared-blue line). This is because both of these buoys are in the LCI region (Fig. 8) and it was shown in the previous discussion that the largest differences are of the order of 0.2 m with coupling. The large errors in SWHs for the four events thus remain even with coupling - only event E1 seems to be predicted with better accuracy compared to the other events (E2, E3, E4 were under-predicted roughly by 20%, 40%, and 15% respectively).

Comparisons of modeled energy spectra are also shown for a snapshot during E4 at the location of B05 (Fig. 37). It can be seen that the directional energy spreading, for the most part, is reasonably predicted by the SWAN model without (Fig. 37b) and with OFC-1H coupling (Fig. 37c). However, the SWAN model underestimates the swell part (around 0.1 Hz) of the wave energy (propagating roughly along 300 deg. direction; Fig. 37a). This is also evident from Fig. 37d where the peak around 0.1 Hz is not captured by the SWAN model. The swell appears to be coming from Gulf of Alaska and the errors in energies at B05 could possibly be related to the corresponding errors in the offshore boundary conditions specified along the eastern open boundary of the wave model. Obviously, the errors discussed above demand further investigation of other factors (winds, wave boundary conditions etc.) in order to identify the cause of such errors. The error analysis is done in the next section.

3.8 Discussion

This section describes the development of an integrated wave model by coupling of wind (WRF), wave (SWAN) and circulation models (EFDC) in CI. The main em-

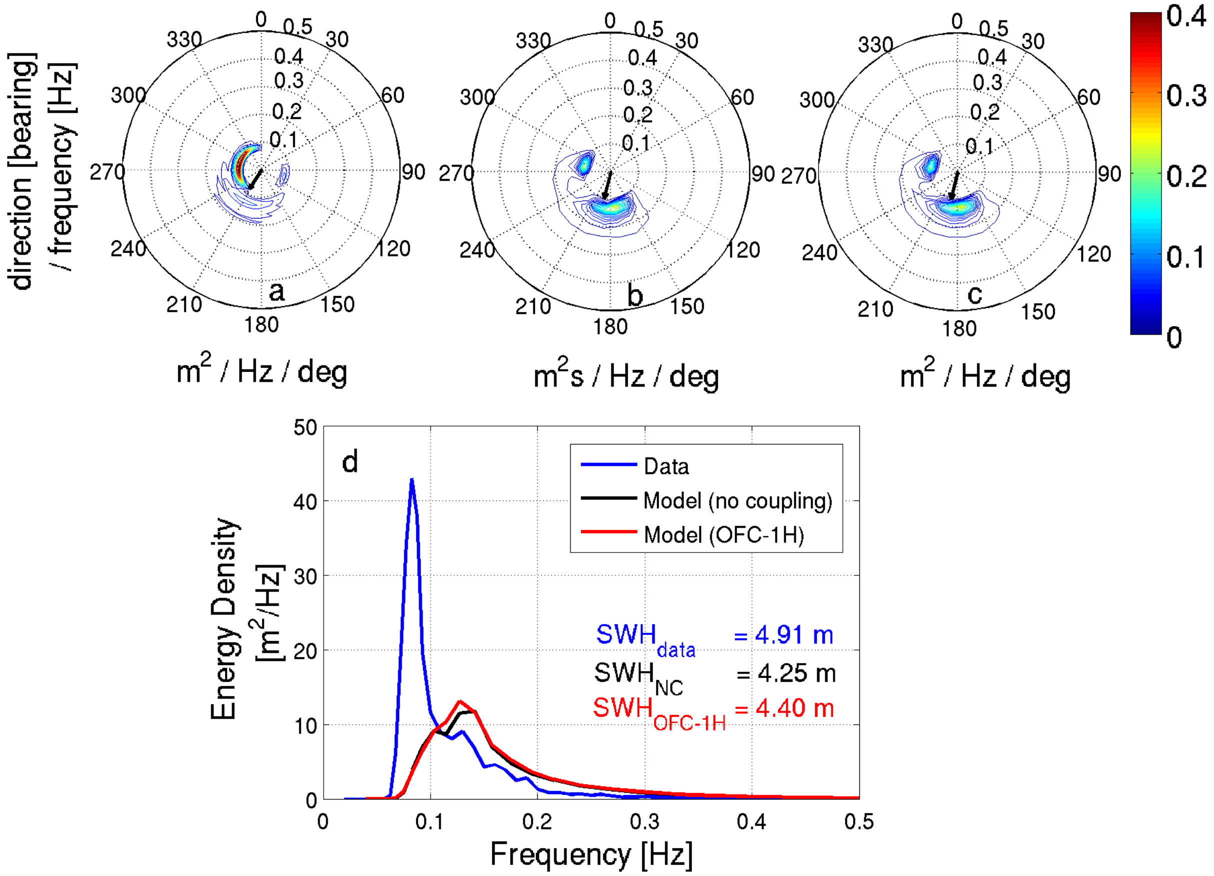

Fig. 37. Energy spectrum comparisons at B05 on 10/26 1800 UTC (during E4). (a) Measured directional wave spectra, (b,c) modeled directional wave spectra without and with OFC-1H coupling, respectively, and (d) comparison of 1-D energy spectrum. Arrows in the center of (a)-(c) show wind direction.

phasis was towards understanding the influence of currents on the wave predictions, which was addressed by coupling of SWAN and EFDC in offline (OFC) and online (ONC) modes. It was found that the differences in SWH results obtained using OFC and ONC were due to the rapidly changing tidal conditions, the effects of which are not updated frequently in ONC because of the assumption of steady conditions in the time between the information exchanges. Sensitivity studies using 1H and 3H updating intervals also showed qualitative differences in the SWHs, and to fully capture the rapid tidal fluctuations, a smaller updating interval (1H or less) may be needed. Since the numerical procedure is simpler in OFC (only EFDC to SWAN), it is found that OFC was more efficient than ONC. In addition, the ONC approach may not be necessary because the effect of the waves on the currents was found to be marginal (2-3 cm/s).

Qualitatively, it is demonstrated that the maximum increase in SWHs is about 0.5 m (>30% change) in the CCI and UCI regions in presence of strong opposing currents (upto 2.5 m/s). In the LCI region, it was found that the SWHs only increased by upto 0.2 m (<8% change) in presence of currents (mostly there were no discernible differences; Fig. 29c,d), which shows that the effects of wave-current interaction in this area are not significant. Extreme analysis showing maximum and minimum increase in SWHs over the entire domain shows regions with significant wave-current interaction (Figs. 33-34). In particular, the constricted region near Forelands shows contrasting trends with the net increase and decrease of SWHs on the eastern and western sides, respectively. The UCI region showed maximum increase and decrease in SWH of upto 1 m in opposing and following current, respectively. In some near-shore areas (e.g. Kachemak Bay), which originally had very small waves without currents (< 0.1 m), it was also found that the inclusion of currents resulted in an enhancement of wave penetration into much shallower areas thereby increasing the SWH by as much as 1 m; however these latter findings are preliminary and worthy of a more detailed micro-scale analysis using better resolved model grids in Kachemak Bay (this is discussed in Section 5.3). Overall, the maps showing extreme variations in SWHs provide an insight into regions with strong wave-current interaction, which can be useful for a number of engineering applications (most notably, navigation). These maps can also be useful for planning future deployments of wave/current gauges to further understand the dynamic wave-current interactions. Data collected through such field surveys could in turn be used for model validation purposes. Some proposed locations where data could be collected are: 1) the east-west transect near Forelands to study the contrasting increase and decrease in SWHs, 2) UCI region between Forelands and Anchorage, and 3) near Kalgin Island.

The coupled wave models were also tested against data measured at the locations of B05 and B06. Since both the buoys are situated in the LCI (where wave-current interaction is not significant), the coupled model results closely followed those obtained without any coupling. Since these buoys are not currently operational and there have been recent talks about possible relocation of B06, results of this study could help in finding alternate locations that are both scientifically and operationally viable.

The adequacy of the circulation model, run in the barotropic mode, for obtaining wave estimates was also addressed. In general, it was found that the EFDC model provided reliable predictions of water-levels and circulation patterns in CI. The water levels were predicted with great accuracy at Kodiak, Seldovia, and Nikiski ($R^2 > 0.98$); near Anchorage a finer grid was required to obtain a better match with data. Results from circulation modeling also indicated regions where barotropic and/or baroclinic effects become important. It was found that the barotropic effects (tide and wind), for the most part, dominated the CI circulation. For instance, the flow velocities (N-S and E-W) near Forelands and Kalgin Island were predicted with high accuracy (m, $R^2 > 0.80$), thereby suggesting that the barotropic effects in this region were more prominent than other effects (e.g. density-driven flows). In contrast, in the western parts of LCI region, baroclinic effects seemed to have affected the E-W flow component (the N-S flow component was modeled with a higher degree of match). The large underprediction of E-W component is possibly due to the Alaska Coastal Current that brings heat and salt fluxes into the CI. Such effects were not included in this study. However, sensitivity studies are undertaken in the next section to address the net effect of underprediction in the E-W flow component on the wave climate in the western LCI region.

4. SENSITIVITY OF FORCING FUNCTIONS ON WAVE PREDICTIONS IN COOK INLET, ALASKA

4.1 Introduction

Sensitivity studies provide a convenient way to determine the output response by inducing a known fluctuation to the input forcing. Such studies help in understanding the model behavior to changes in the inputs, which is of great importance in asserting modeler's confidence in the model results. Sensitivity analysis also helps in estimating the robustness of the model as well as the various uncertainties associated with the model output.

In the context of coupled wave modeling, Plant et al. (2009) showed that the wave and flow models were extremely sensitive to the resolution of the input bathymetry. In particular, they found contrasting responses of wave and flow models to bathymetric resolution, and suggested that bathymetric smoothing could be optimized differently for the two models. Sensitivity studies are also routinely performed for addressing the effect of winds on waves. In some cases, artificial adjustment to wind speeds are made to quantify the corresponding errors in the wave heights. For instance, Dykes et al. (2009) enhanced the wind speeds by a factor of 1.1 in order to examine if the systematic underprediction in SWHs was related to underprediction in the winds. Contrary to other findings that frequently attribute errors in SWHs to errors in winds (Janssen 1989, Cavaleri et al. 1991, Komen et al. 1994, etc.), their analysis did not show significant differences in SWHs.

In this section, sensitivity analysis is performed to determine the response of the wave model to input variation. In particular, errors in the wave model results are quantified by identifying corresponding errors in the input forcing functions (winds, currents, boundary conditions, etc.). In addition, other model parameters such as the model time-steps, resolution etc. also dictate the quality of the final product. A systematic approach is undertaken to identify the errors in SWHs for the four storm events discussed in Section 3.7 (E1-E4; Fig. 24). The identification and quantification of such errors could eventually serve as "guidance" for estimating the uncertainty associated with the wave forecasts, thereby informing the forecast user of such uncertainty. In the following, the effect of these errors is discussed in detail using SWH data measured at B05.

4.2 Sensitivity to modeled currents

It was noted in Section 3.3.4 that the circulation model under-predicted the intensity of E-W flow component in the lower inlet (LCI) by more than 50%, which may have arisen due to contributions from other factors (such as buoyancy-driven flows) not included in the circulation modeling. Since surface-currents are used as a forcing term in the wave model, errors in their predictions may have propagated into the wave model. To assess the influence of these errors on the wave estimates,

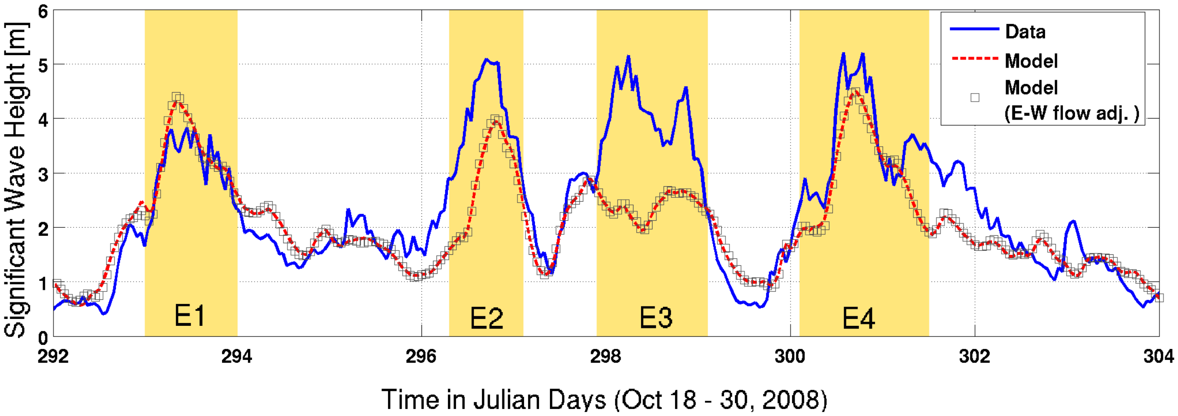

Fig. 38. SWH comparisons at B05 with and without correction factor to E-W flow.

an enhancement by a factor of 2 was applied to the E-W velocities in the lower inlet only (i.e. between 59^o to 60^o N, and -153.5^o W to -152^o W); the N-S velocities were not altered. Fig. 38 shows the comparison of SWH's at B05 with and without the correction factor. There are no readily discernible differences between the two model estimates, implying that the wave model errors due to under-prediction in E-W flow are marginal in the lower inlet.

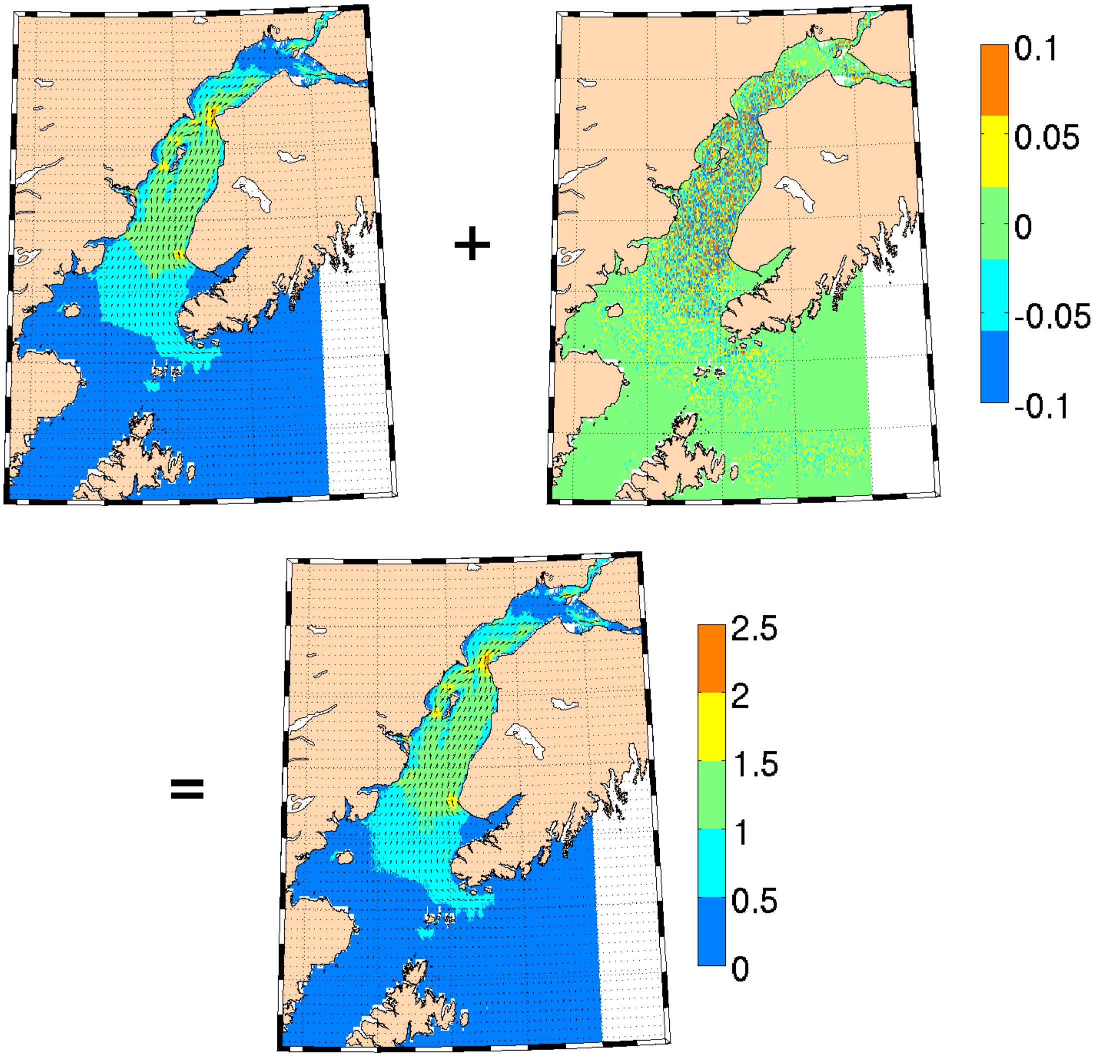

Fig. 39. Example of adding random noise to input currents.

To further examine the effect of errors in currents, which could be due to the winds, tides, and baroclinic forcing, a sensitivity analysis was performed by adding uniformly distributed random noise to the modeled flow velocities. In particular, the input current-fields were altered by a uniformly distributed ± 10% random noise, generated using MATLAB's in-built function *rand*. The following equation describes the method for adding random noise into an input vector-field

$$\overrightarrow{X'} = \overrightarrow{X} + R\overrightarrow{X} \tag{13}$$

where $\overrightarrow{X}$ is the original input, $\overrightarrow{X'}$ is the modified input, and R is the random noise (for this study $-0.1 \leq R \leq 0.1$). An example illustrating the effect of adding ±10% random noise on the surface-currents is shown in Fig. 39.

An extreme analysis of this artificial fluctuation on the modeled SWHs was then performed. Figs. 40 and 41, respectively show the maximum increase and decrease of SWHs due to the imposed ±10% noise. It can be seen that the largest fluctuation in SWHs occurs in the northern CI region (upto ±0.6 m). This is because the corresponding intensity of currents is also large in this region (~ 2 m/s) and a ±10% variation in such values induces large changes in the SWHs. This is also in line with the patterns observed in Figs. 33 and 34, when the largest fluctuations due to wave-current interactions was found in the northern regions.

At other locations, i.e. in the lower CI regions, it was found that, for the most part, the maximum differences between the SWHs were of the order of ±10 cm. These small differences are negligible in the context of the surface wave height applications.

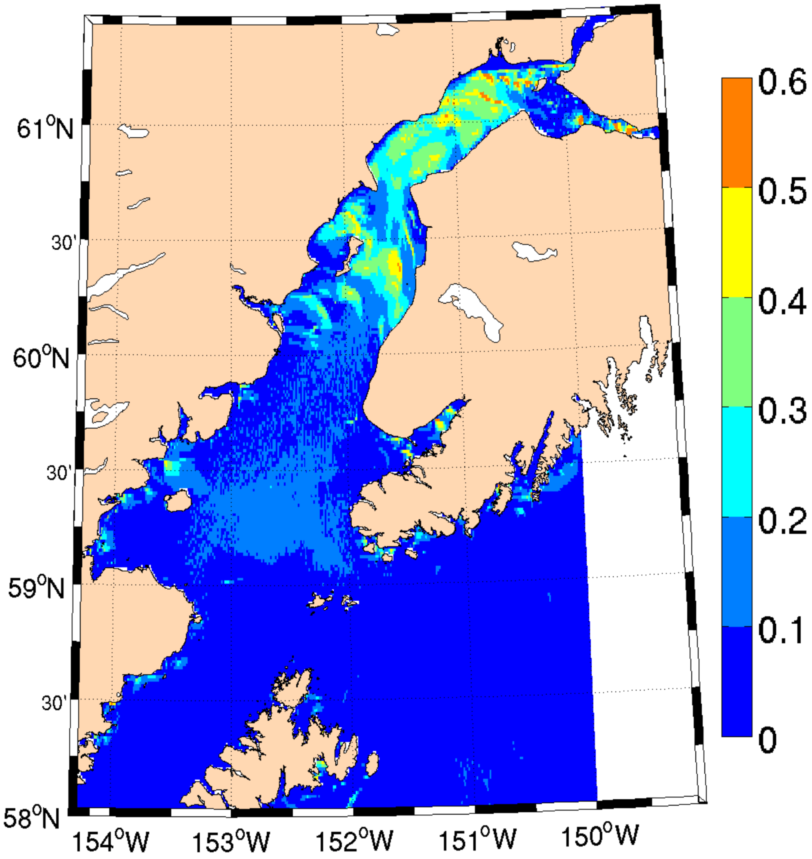

Fig. 40. Maximum increase in modeled SWH (in m) due to addition of random noise to input currents.

4.3 Sensitivity to open boundary conditions

The accuracy of the open boundary conditions (OBCs) could dictate the accuracy of the wave conditions at locations in the interior of the model domain. If the swell information at the offshore boundary of the wave model domain is not accurate, the arrival and intensity of such swells at locations inside the model domain may be incorrect. Thus, one needs "accurate" information about such phenomenon at the open boundaries so that it can be correctly represented at other locations.

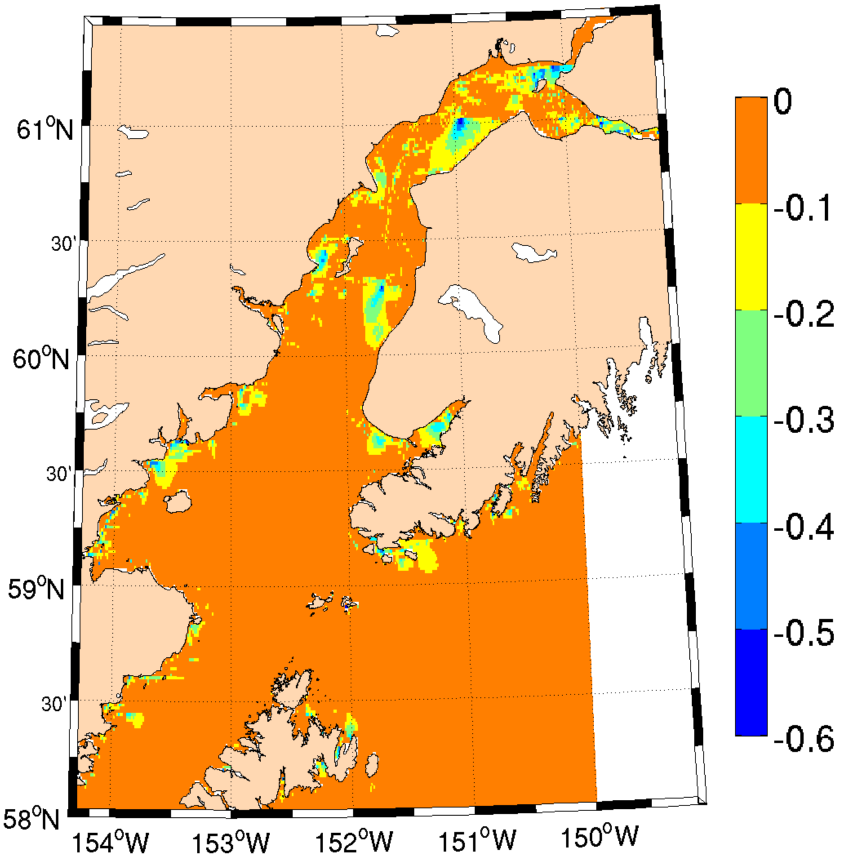

Fig. 41. Maximum decrease in modeled SWH (in m) due to addition of random noise to input currents.

The LCI is often dominated by swells coming from Gulf of Alaska through Stevenson Passage and Kennedy Entrances towards the east, and Shelikof Strait towards the west (Fig. 3). The spectral output of WW3 model forms the basis for the OBCs of the CI wave model. As discussed earlier in Section 3.3.5, spectra at B78 and B80 were forced along the open boundaries. It is thus obvious to first check the quality of WW3 output at those buoy locations to get an insight into the magnitude of errors present in the WW3 output. It can be clearly seen that the four storm events are also under-estimated by WW3 (Fig. 42). For example, during E4, the measured

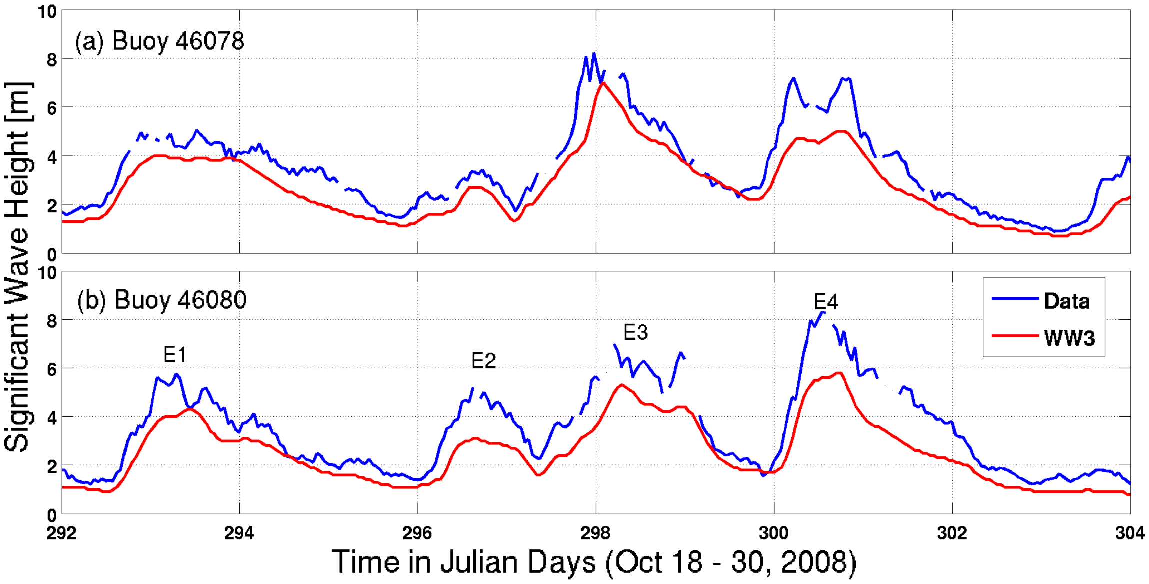

Fig. 42. SWH comparisons of WW3 output at B78 and B80.

SWH at B80 exceeded 8 m whereas the WW3 prediction was about 5.5 m (∼30% underestimation). This implies that these errors on the boundaries could be responsible for some of the error (or the entire error) at locations inside the model domain.

The only way to confirm this is to force the model through buoy-measured wave spectra on the open boundaries. Unfortunately, B78 and B80 only measure one-dimensional wave energy spectrum and do not contain any directional information. Thus, the buoy-measured spectra was used along with the WW3 output of peak wave direction (assuming it was accurate) and the spreading function of Mitsuyasu et al. (1975) to construct a two-dimensional (2D) wave energy spectrum. The resulting 2D wave spectra were then imposed along the open boundaries.

The wave model results at the locations of B78, B80, and B05 using the buoy-imposed spectra are shown in Fig. 43. The model output closely matched the buoy

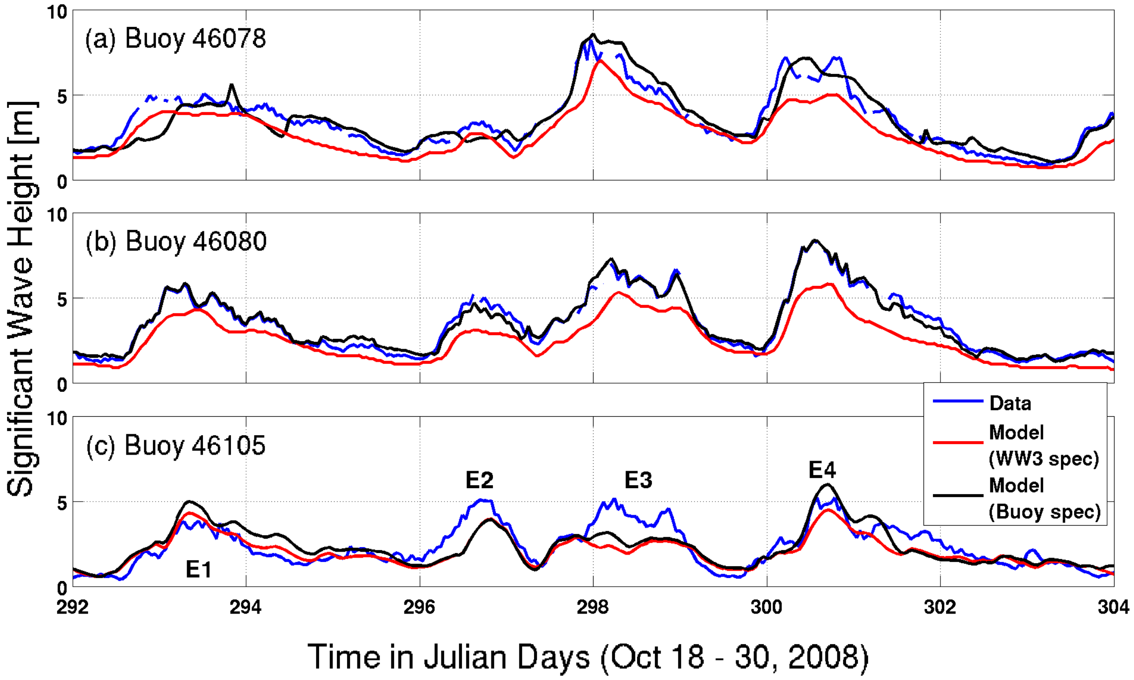

Fig. 43. SWH comparisons at B78, B80, and B05 using buoy-imposed spectra.

measurements at the locations of B78 and B80 (Fig. 43a,b). At the location of B05 (Fig. 43c), it can be seen that the model captured the peak associated with E4 quite well. As discussed in Section 3.3.7 (Fig. 37), the wave direction during E4 is predominantly from the eastern Gulf of Alaska. This implies, to some extent, that the large seas associated with E4 are representative of the seas that occurred at B80 (located on the eastern boundary of the model domain). A comparison of energy densities using WW3 spectra and buoy-imposed spectra is shown in Fig. 44. The swell part of the energy, that was missing using WW3 spectra (Fig. 37), is now captured by the model, although the peak remains under-predicted. A second peak also occurs at f=0.13 Hz, and seems consistent with the prevailing wind direction (Fig. 37). At any rate, this clearly shows the importance of accurate boundary conditions for reliable wave estimates in the interior of the domain.

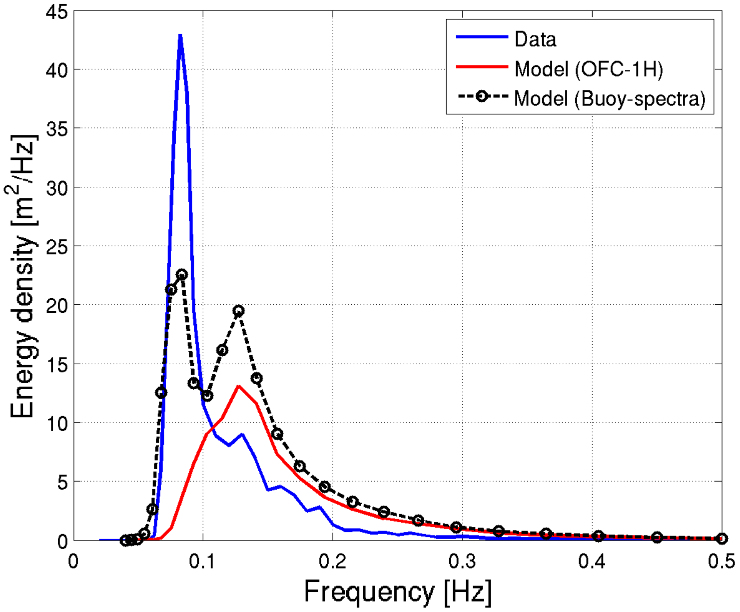

Fig. 44. Energy density (m^2/Hz) comparisons.

Apart from E4, wave heights for events E2 and E3 do not seem to be affected by the buoy-imposed spectra on the boundaries. This may possibly mean that the seas measured during these events may not have originated in Gulf of Alaska, and rather are a result of some other physical phenomenon. Indeed, during these events, the predominant easterly winds generated westward propagating waves (Fig. 24).

Comparisons at the location of Buoy 46077 (B77) are also shown to check the validity of using wave conditions at B78 on the entire west-boundary. B77 is located in Shelikof Strait (Fig. 3) and experiences the swells coming from the south-west direction (apart from locally generated wind-seas). As can be seen from Fig. 45, the model results do not fair well throughout the period of the simulation. This indicates that the assumption of wave conditions from B78 is incorrect along the western open boundary. Unfortunately, there are no nearby points along the western boundary from where full spectral information could be extracted. Thus, we have

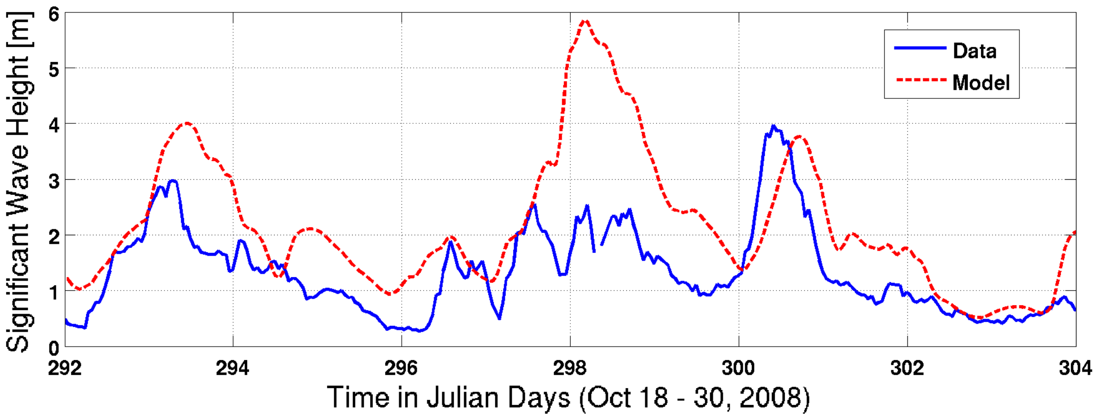

Fig. 45. SWH comparisons at B77.

resorted to using an approximate approach for generating the 2D wave spectra along the western boundary. In particular, WW3 provides output of SWH, peak wave period, and peak wave direction on a 7 km grid for northern Gulf of Alaska. Using these quantities, one can utilize the JONSWAP spectrum (Hasselmann et al. 1973) along with a suitable directional spreading function to create a 2D energy spectrum (see Section 6.3 for specific details).

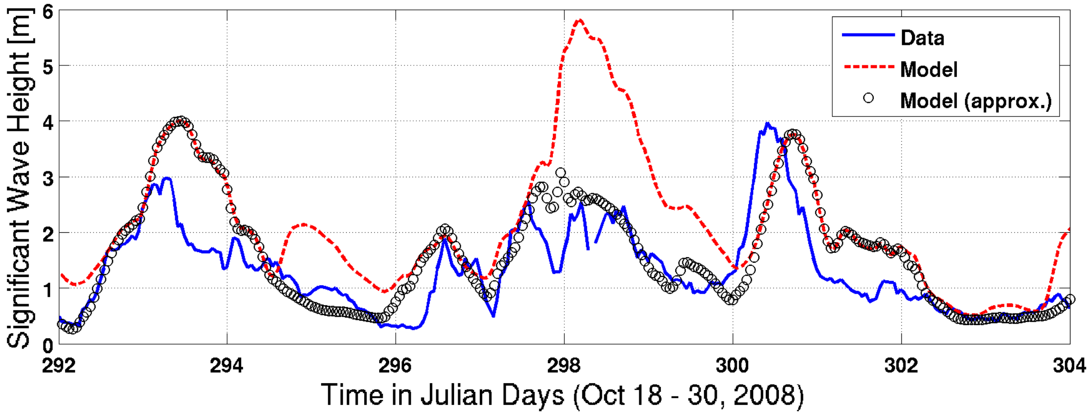

Fig. 46. SWH comparisons at B77 with approximated approach.

Fig. 46 shows the effect of using the approximate approach on SWHs at the location of B77. It can be seen that the large errors around day 298 have reduced significantly. This allows us to conclude that the approximate approach of using JONSWAP spectrum is superior to assuming the wave conditions from B78 along the western boundary. For the remainder of the discussion that follows, the open boundaries are forced by approximated 2D JONSWAP spectrum on the western boundary and the full spectral output at the locations of B78 and B80 along the southern and the eastern boundary, respectively.

4.4 Sensitivity to winds

We now consider the errors in the input winds which were obtained from the WRF model. Based on the previous discussion, events E2 and E3 do not seem to be affected by the the errors present in the currents or the OBCs. To check whether the underestimation of SWHs during events E2 and E3 were due to the errors in the winds, the quality of WRF winds was checked specifically during those two events.

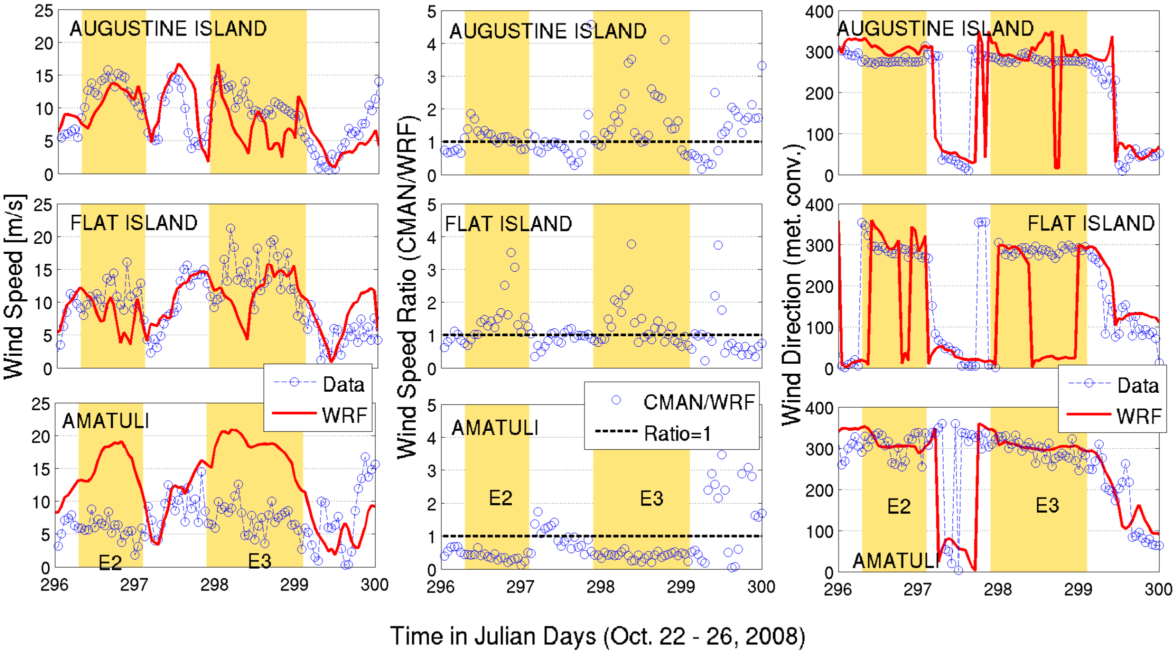

Fig. 47. Wind comparisons at three weather stations near B05.

Fig. 47 shows the comparison of WRF winds at the locations of three weather stations Augustine Island (AUGA2), Flat Island (FILA2), and Amatuli Island (AMAA2) - that form a triangle around B05 (Fig. 5). The winds were predominantly from the west during the two events (Fig. 47 right column) - this trend in wind direction is typical of the month of October when the winds originate from Iliamna Lake in the west (Liu et al. 2006). It is clear that the WRF model under-predicted the wind speeds near AUGA2 and FILA2. The under-prediction, on average, was about a factor of 1.25 for E2, and about 1.75 for E3 (central panels of Fig. 47). This under-prediction in the wind speeds seems to be in line with the corresponding under-prediction in the modeled SWHs. The winds at AMAA2, on the contrary, were consistently over-predicted by WRF (this trend was found during other times as well). It seems that the WRF model, at its operating resolution, may not have resolved the topographical features near Amatuli Island in detail. However, a full assessment of WRF model for CI is beyond the scope of this dissertation, and attention is rather directed towards finding solutions in order to improve the corresponding wave estimates.

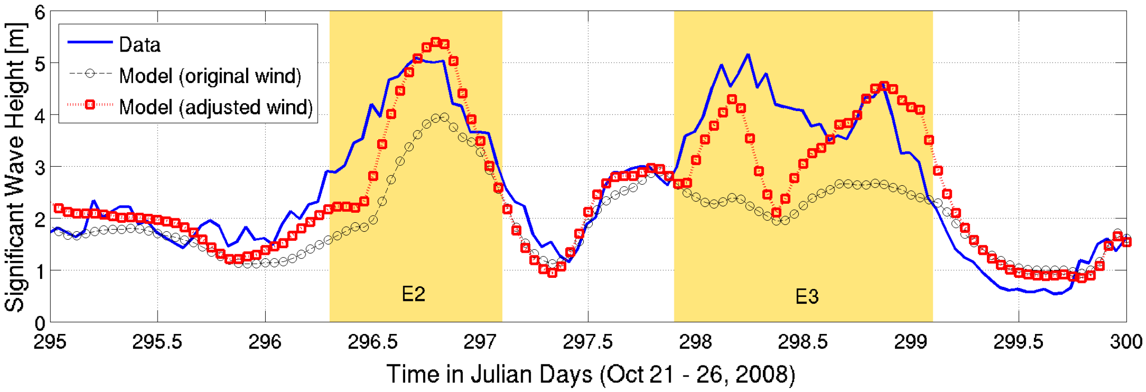

Fig. 48. SWH comparisons at B05 before and after wind adjustment.

As far as events E2 and E3 are concerned, a straightforward experiment is to modify the wind speeds using the average under-prediction ratio and observing the corresponding response of the wave model. The WRF wind speeds were thus adjusted by a factor of 1.25 locally over a small region near B05 (somewhat subjectively determined) for E2 (that lasted about a day); a factor of 1.75 was used over the same region for E3 (also lasted about a day). The SWH results after these adjustments are shown in Fig. 48. It is clear that the adjustment significantly improves the wave estimates during E2 and E3 (even though some errors still remain).

Although the above discussion shows that improving the winds for specific events may improve the wave heights, the obvious question, viz. "how does the wave forecaster know there is a problem with the winds?", still remains unanswered. The above discussion suggests that the WRF model under-performs when winds blow from the west in the lower inlet, but this conclusion is based on only two events. If this trend occurs majority of the times, one possible solution could be to correct the winds blowing from the west by a suitable factor before inputting into the wave forecast model. To test this hypothesis, data from AUGA2 was compared to WRF winds for two winter seasons-Fall 2007 and Fall 2008. Only the winds predicted to be coming from the west (i.e. between 240-300 degrees) were considered for this analysis.

Fig. 49 shows this comparison and it can be seen from the best-fit line that, in general, the WRF model under-predicted the winds from the west. However, there is significant scatter throughout the range of wind-speeds. For instance, the WRF model mostly over-predicted the winds measured between 0-5 m/s, and sometimes the over-prediction was as large as three times the actual wind speed. On the other hand, for winds measured between 10-15 m/s, WRF model seemed to have under-predicted as well as over-predicted. Thus, given the uncertainty, it is impossible to

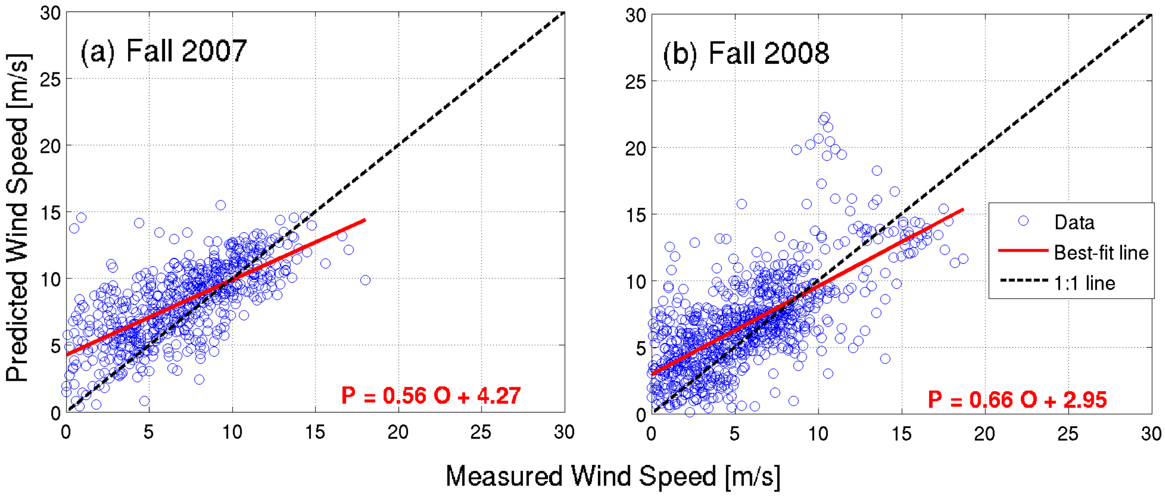

Fig. 49. Wind speed comparisons at AUGA2 for (a) Fall 2007 and (b) Fall 2008. Note that only winds blowing from the west were shown.

devise appropriate corrections to WRF winds before use in wave forecasting scheme for CI. Other solutions (such as improvement of WRF model physics, better resolved topographical features, data assimilation, etc.) are yet to be explored.

As in the case of currents, a sensitivity study was performed by adding random ±10% error to the wind velocities. Figs. 50 and 51, respectively show the maximum increase and decrease in SWHs as a result of the imposed noise.

The largest SWH variation (± 0.5m) is again found in the northern parts of CI. The results at other locations were not significantly different compared to those obtained without the random error.

4.5 Discussion

In this section, sensitivity studies involving artificial adjustment to various input forcing functions were performed in order to determine the corresponding variation

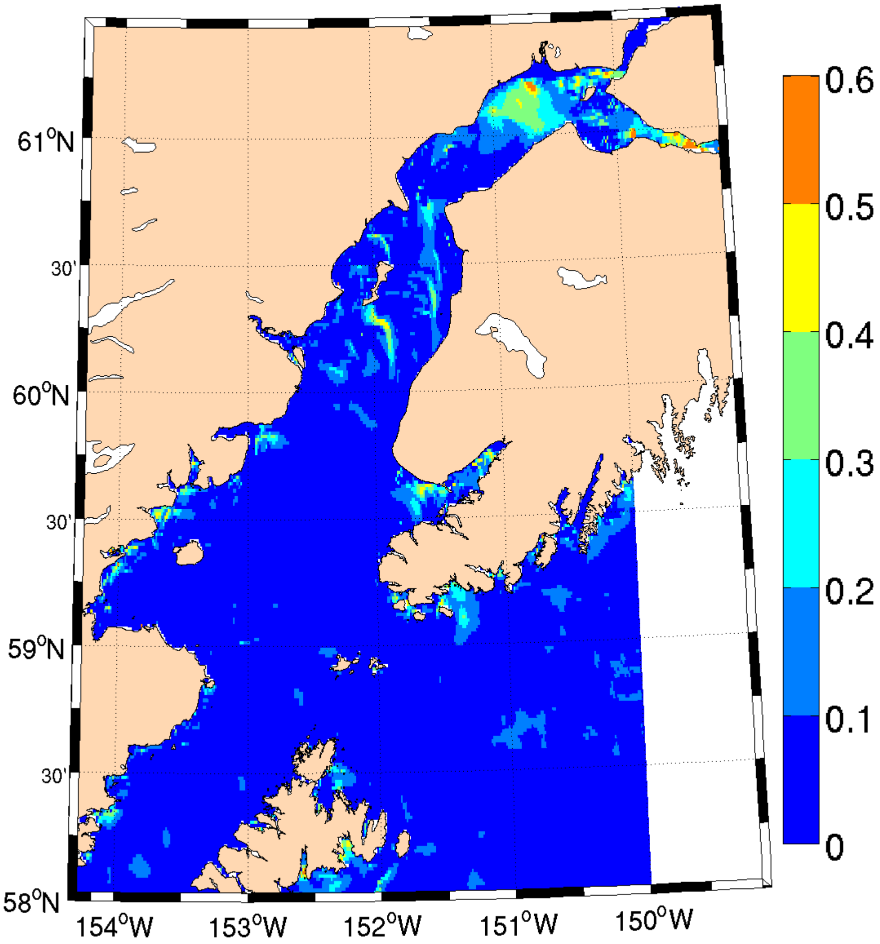

Fig. 50. Maximum increase in modeled SWH (in m) due to addition of random noise to input winds.

in the modeled wave heights, and also to find regions where such variations were largest.

In the case of input currents, it was found that 100% enhancement of E-W flow component in the lower CI (to account for baroclinic forcing) had only a marginal difference on the SWHs (< 10 cm on average). The addition of random noise in cur-

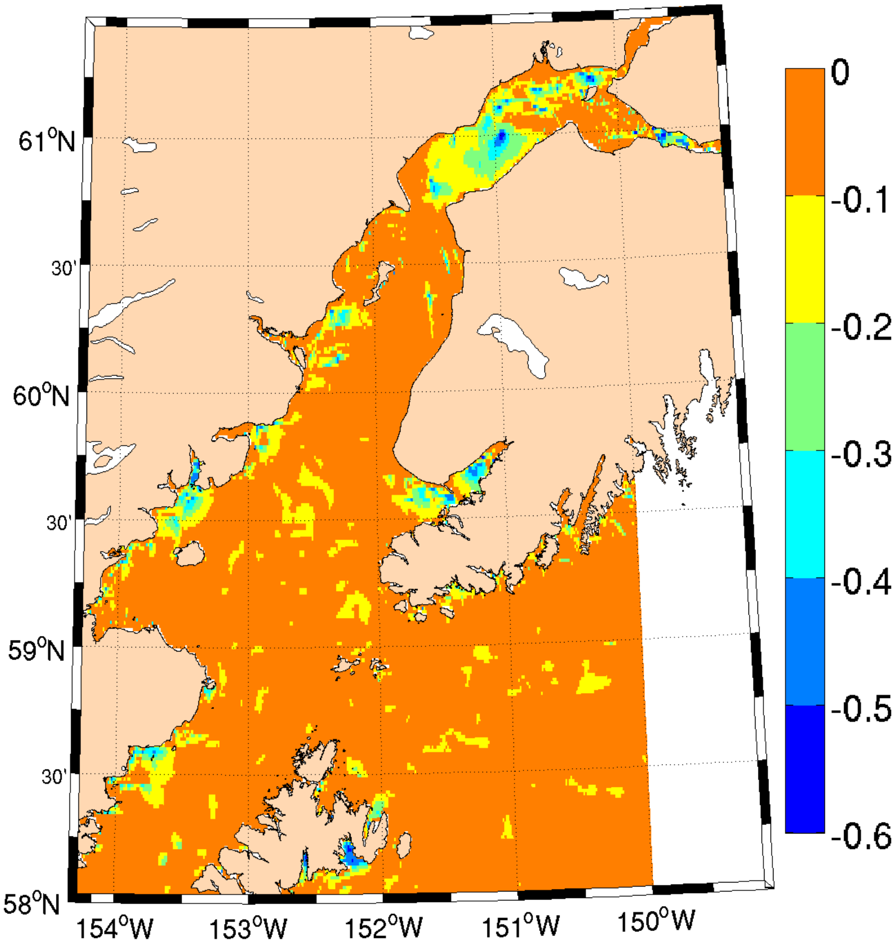

Fig. 51. Maximum decrease in modeled SWH (in m) due to addition of random noise to input winds.

rents, however, showed variations upto ± 0.6 m in the northern CI region, indicating stronger sensitivity of the wave model in that region.

The other errors in predicted SWHs were found to be due to the corresponding errors in the winds and the offshore wave boundary conditions. Both had a significant effect on the modeled SWHs, and it was shown that an improvement in their accuracy thereby improves the accuracy of the wave predictions. From statistical analysis of the WRF winds, it was found that the errors in winds were random and thus could not be easily remedied. A sensitivity analysis, similar to that adopted for currents, was also performed for the winds by adding random noise to the wind velocities. The findings of this analysis were similar to those for the currents, with upto ± 0.5 m SWH variation occurring in the northern parts. The results, however, showed no drastic differences elsewhere. As to the boundary conditions, the SWHs at B05 were sometimes found to be sensitive to the wave conditions at B80 (e.g. during E4). Overall, it is found that about 30% error in boundary conditions at B80 resulted in about 15% error in SWHs at B05.

In conclusion, this study sheds more light on the impact of various physical phenomena on wave estimates in CI, which were hitherto not understood in detail. It is demonstrated that the errors in wave modeling arise from a wide variety of mechanisms such as winds, currents, offshore wave climate and also from the choice of modeling schemes such as one-way or two-way coupling (discussed in Section 3.6). These findings clearly indicate the need for data measurements in the northern parts of CI to verify the performance of the coupled wave modeling undertaken in this dissertation. With the help of observations, advancements to these modeling systems could be performed in the future (such as high-resolution modeling, including the effects of baroclinic gradients, etc.).

5. HIGH-RESOLUTION COUPLED MODELING IN KACHEMAK BAY REGION

5.1 Introduction

Kachemak Bay (KB) is an elongated bay in the lower CI region, south-west of Kenai Peninsula (Fig. 52). The bay stretches about 40 miles in length, and about 25 miles in width. KB is the largest reserve system in the National Estuarine Research Reserve System, and is one of the most productive (in terms of biological productivity) and diverse estuaries in Alaska. The local economy is mostly based on

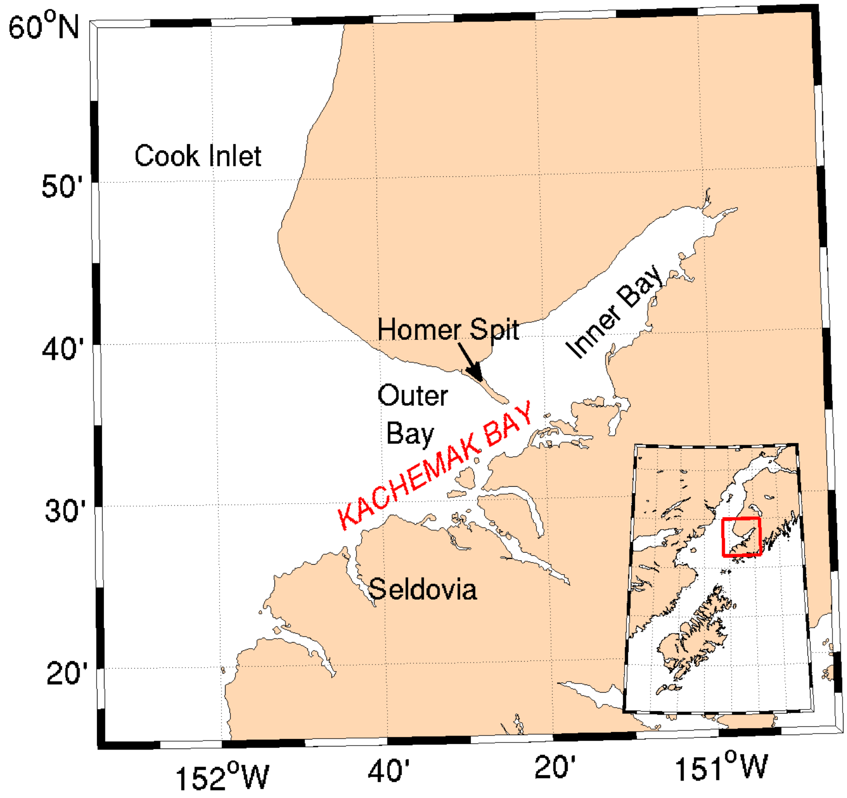

Fig. 52. General location of Kachemak Bay (KB). Red box in the inset shows the geographical location of KB in Cook Inlet, Alaska.

fishing and tourism. The Homer Spit is quite a magnificent landmark and is among the largest spits extending about 5 miles into KB. The spit separates the KB into "inner" and "outer" bays. The spit also is home to one of the largest boat harbors in the state and serves as an ideal connection to the Alaska Marine Highway. Several vessels, traveling up into CI, deliver goods to and from the Homer harbor.

Similar to CI, KB is also an extremely dynamic system. Cyclonic low-pressure systems, that originate in the Gulf of Alaska, make their way into KB from the west and as a result, the bay experiences significant wind-wave action. In particular, the western side of the Homer Spit is exposed to strong wave energy. There are also significant tidal fluctuations, with tidal range of about 8 m. In addition, strong tidal flows, together with the east-west flowing Alaska Coastal Current (ACC), dominate the circulation patterns. During flood tide, water enters into outer KB from the south and exits from the north. The narrow opening between the Homer Spit and the southern coastline facilitates water exchange between the inner and outer bays. Apart from the violent metocean conditions, the bay is also vulnerable to the threat of tsunamis due to volcanic eruptions. Mt. Augustine, about 60 miles south-west of Homer, is one of the most active volcanoes in the region. Historical evidence suggests that during an 1883 eruption, debris avalanche from Mt. Augustine created a tsunami that hit the south-side of KB with waves as high as 10 m (Beget and Kienle 1992).

The dynamic features noted above and the interesting results obtained in Section 3.6 (i.e. upto 1 m difference in the SWHs with the inclusion of currents) motivate the study conducted in this section. In particular, this section performs high-resolution coupled wave modeling for the KB region (hereafter, KB model). With the help of such modeling, this study aims to address the following questions:

1. Do the SWH results obtained from the KB model reconcile with those from the low-resolution model (see Section 3.6 for details)? If not, does one need the finer grid in order to make a more accurate forecast in KB?
2. What wave frequency range should be used if the region experiences locally generated wind-seas?
3. For the finer grid, are there significant differences with and without the currents?
4. How well does the model represent flooding and drying cycles in inner KB?

5.2 Bathymetric data and features

Due to aforementioned tsunami threats, NOAA's NGDC has compiled a very-high resolution bathymetry database to aid in the numerical tsunami predictions in KB region. The bathymetry of this dataset is at a resolution of 1/3 arc-second ($\sim$ 10 m) and is shown in Fig. 53. The bay is mostly shallow, with an average depth of about 40 m. There is significant north-south variability with shallower depths in the north, that gradually increase towards the south (Fig. 53). The southern region is characterized by several trenches and valleys with depths upto 200 m. These trenches further extend into the inner bay, through a narrow opening near the Homer Spit, and are about 80-100 m deep. The northern parts of the inner bay are very shallow ($<$ 10 m deep) and due to the extreme tidal fluctuations (upto 8 m), a large area becomes dry during low tide.

It should be noted that the available bathymetric resolution is too large for the purposes of this study. In addition, the computing equipment for handling such resolution was not available. Hence, the bathymetry was filtered to a resolution of

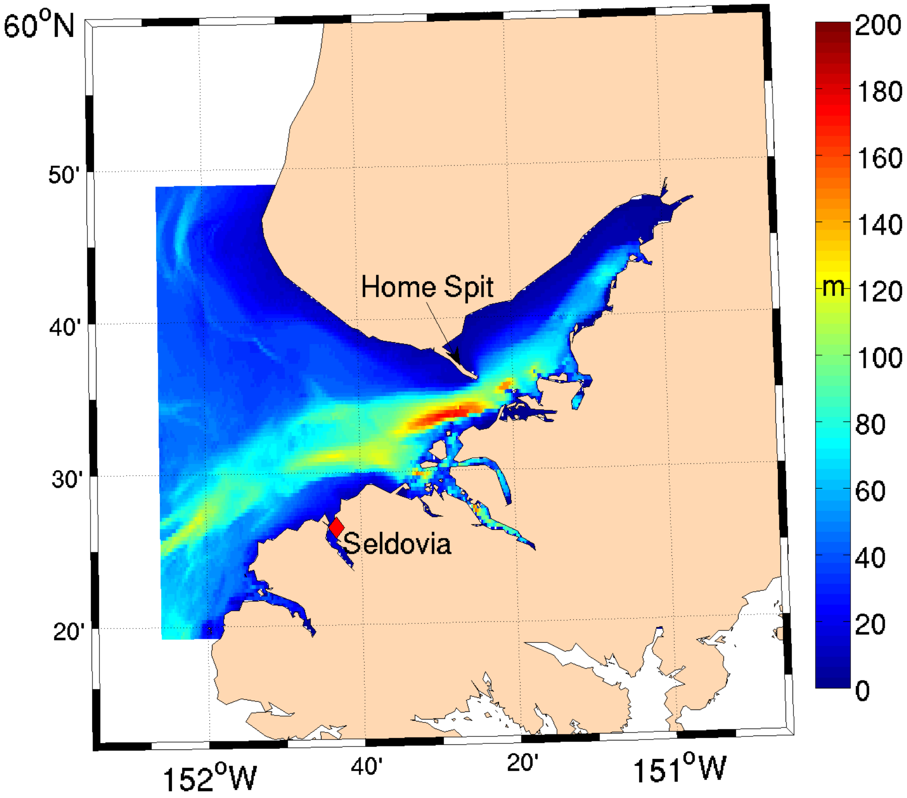

Fig. 53. KB bathymetry in meters. Red diamond shows the location of tidal gauge at Seldovia.

about 15 arc-second (approx. 200 m). The filtering was performed at NGDC and data was kindly provided to us by Mr. Barry Eakins.

5.3 Coupled wave-circulation model for KB

For understanding the wave-current interaction on higher spatial resolution, separate wave and circulation models were established in KB. These models were driven by the solutions of the low-resolution outer grid CI models on the boundaries. The model domain for KB models is shown in Fig. 54.

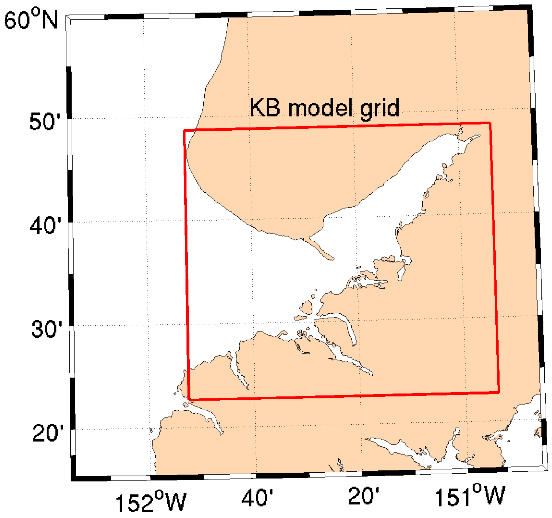

Fig. 54. KB domain for coupled wave-current model.

First, the circulation modeling part is addressed. In general, the KB circulation is driven by various mechanisms such as tides, winds, freshwater inflow (from rivers, glacial melts, precipitation, etc.), heat and salt fluxes from ACC. Even though existing literature points that the glacial freshwater discharge significantly contributes to the overall circulation patterns in KB (Schoch and Chenelot 2004), none of those studies have actually measured the glacial flow rates in KB. Also, how much flux the ACC and evaporation/precipitation bring into the system is uncertain to a large extent. Given the lack of flow data and the uncertainties, the effect of baroclinic gradients is neglected from the KB model. The focus is thus towards the wind- and tide-driven circulation patterns. Approximated glacial discharge was added into the model only from the viewpoint of mass balance.

The comparison of modeled WSEs (“water surface elevations”) to the data measured at Seldovia are shown (Fig. 55), and it can be seen that the higher resolution KB model captures the tidal variation and magnitudes quite well (similar agreement was found from the outer grid results; Fig. 10).

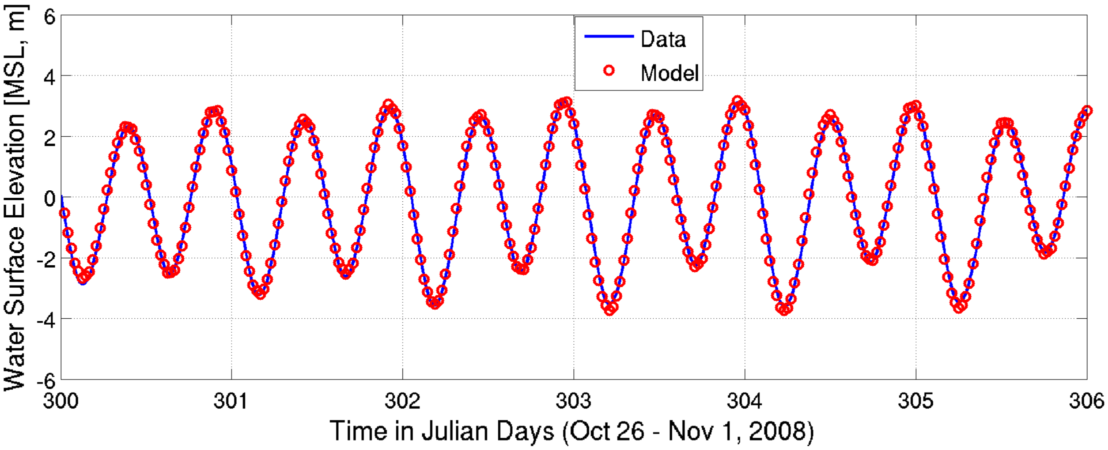

Fig. 55. WSE comparisons of KB model with data collected at Seldovia.

The model was then tested for its capability to simulate the alternate wetting and drying of KB. As can be seen from the NOAA navigational chart in Fig. 56, during low water, the entire western shoreline as well as the extreme north-eastern parts of the "inner" bay become dry.

Three representative drying depths (HDRY) - 10 cm, 20 cm, and 50 cm - were chosen to model the extent of dry regions. For each time-step, the model checks the total depth (H in Eq. 3, Section 2.2) against the drying depth (HDRY) at each grid point. If $H <$HDRY at a grid point, then the model assumes that point to be "dry" (although a thin film of water remains at that grid point for continuity balance). The flow velocities for "dry" grid points are then set to zero. Fig. 57 shows the snapshot of modeled total depth during the time when water level at Seldovia was lowest (inset of Fig. 57a). While all three chosen values of drying depths seem to show some drying, simulation performed using HDRY=50 cm (Fig. 57c) predicted the extent of "dry" regions that closely matched those shown in Fig. 56.

The KB circulation model was then tested for tide-, wind-, and river-induced circulations. The main purpose was to determine those forcing mechanisms that

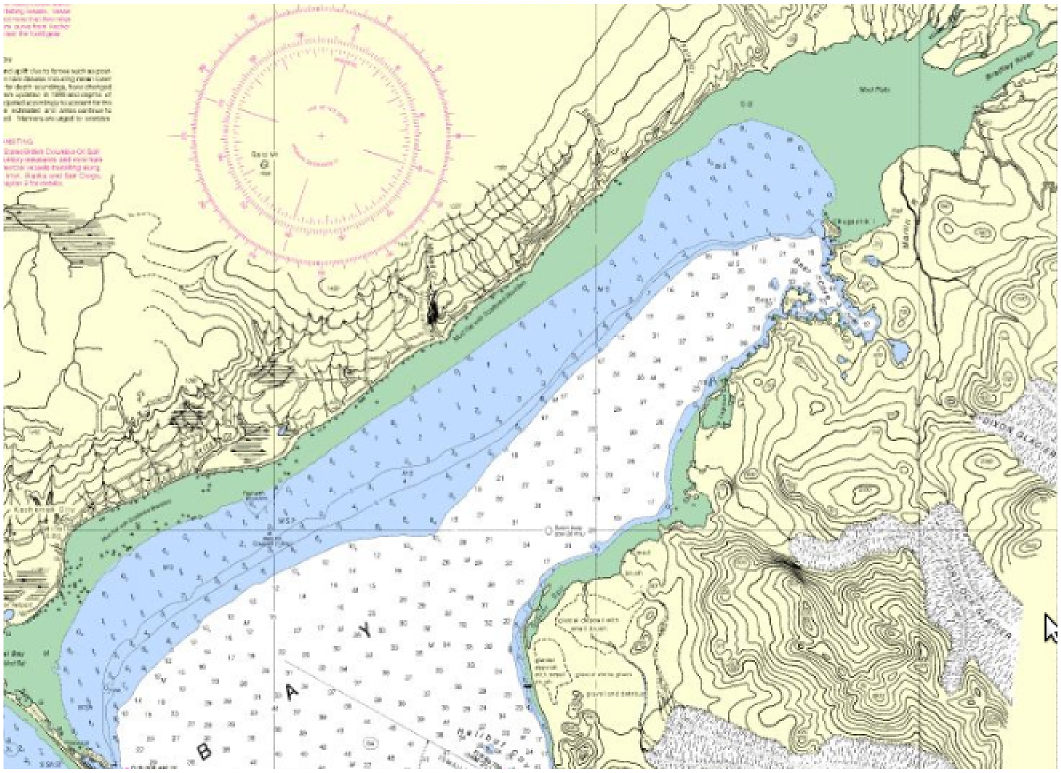

Fig. 56. Map of "inner" KB showing the extent of dry regions, which are depicted by the green shaded area (source: NOAA).

dominate the circulation patterns inside the domain. An example map of circulation patterns through various mechanisms (i.e. tide, wind, and river) is shown in Fig. 58 for the flood current. The top panels (a)-(c) show individual contributions of tide, wind, and river forcing mechanisms, respectively; the bottom panels (d)-(f) show contributions of different forcing in various combinations, viz. tide+wind, tide+river, and tide+wind+river, respectively. In the river-induced case, a constant river discharge of about 500 m^3/s was added near the north-east corner (Fig. 58c). The discharge rate and the region of inflow was subjectively determined. This discharge rate resulted into currents on the order of 0.8-1.0 m/s near the source, which do not seem to have propagated into other parts of the domain (note that the color-scale is, however, truncated to 0.6 m/s to delineate other features).

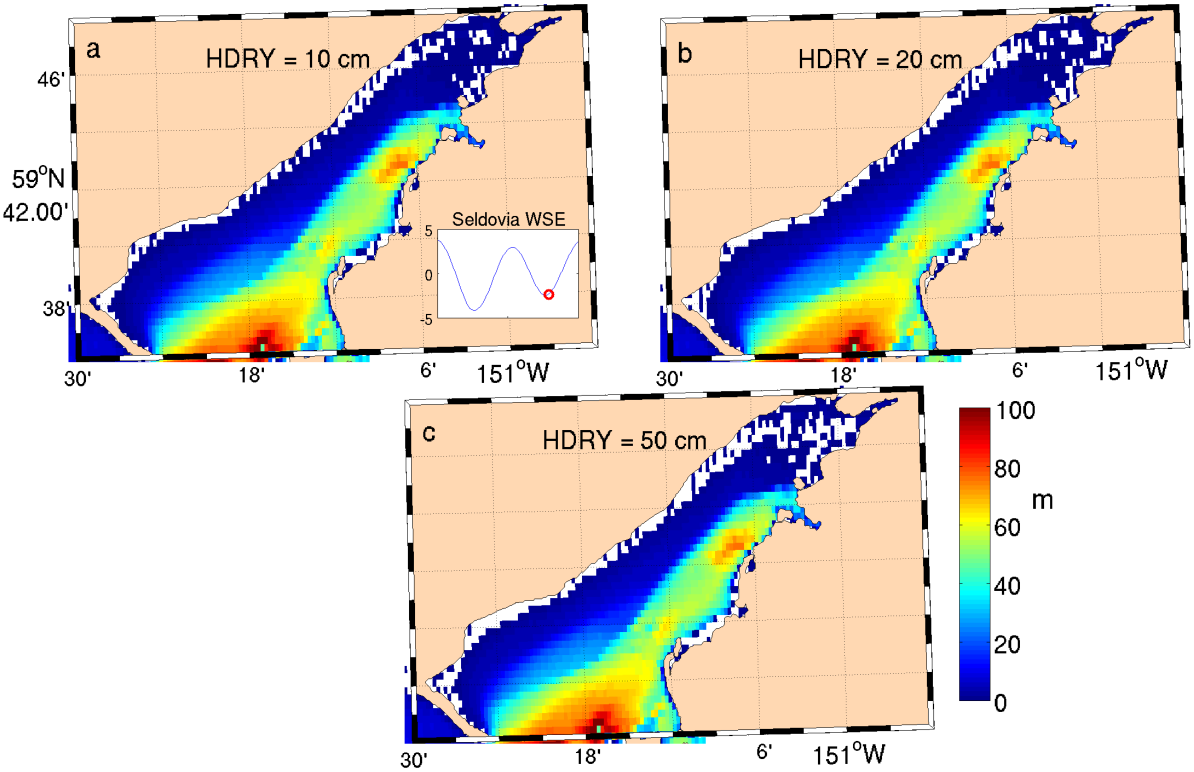

Fig. 57. Sensitivity of modeled dry regions (shown by white spaces) to drying depth. Inset in (a) shows measured (blue line) and modeled (red circle) WSE at Seldovia during the snapshot.

The tide-induced currents seem to be stronger in the "outer" bay and ranged between 0.5-0.6 m/s (Fig. 58a), while the wind-induced currents, during this snapshot, were stronger along the western shoreline of the "inner" bay (Fig. 58b) and ranged between 0.2-0.3 m/s. The maximum tidal flow was found near the northern open boundaries (upto 1 m/s). Tidal currents were also found to be elevated near the tip of the Homer Spit with values of the order of 0.3-0.4 m/s. During other times (not shown), the wind-induced currents were found to be as strong as 0.3-0.4 m/s in the "inner" bay. Although the effect of baroclinic gradients was neglected, it seems that the tides and winds contribute most to the overall circulation patterns in KB and

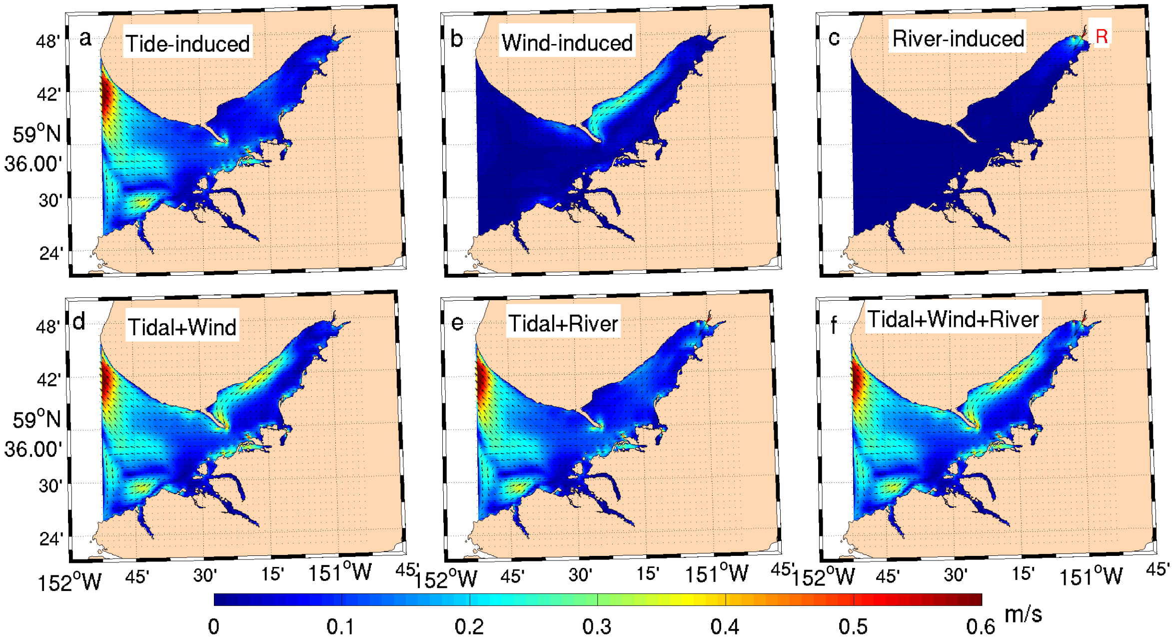

Fig. 58. Example map of various combinations of tide-, wind-, and river-induced circulation patterns in KB. "R" in panel *c* represents location of inflow in the model.

the range of currents is mostly between 0.5-1 m/s. The effect of river discharge, from the mass balance perspective, seems to be localized.

The focus then shifted towards wave modeling. The KB wave model was initially forced by the winds and wave boundary conditions obtained from the main CI grid solution. The impact of spectral resolution, in particular the frequency space, on SWHs was first studied. This was done to check the model sensitivity to short- and long-period seas. It can be seen that the "inner" bay shows wave development further to the east when higher frequencies were included in the wave modeling (Fig. 59b), and the differences of up to 0.5 m can be found (Fig. 59c). This indicates that the "inner" bay may be dominated by winds that are locally-generated (and also affected by the surrounding mountainous topography). To properly resolve such dynamic effects, the KB wave model was run for 0.05 Hz to 1 Hz frequencies.

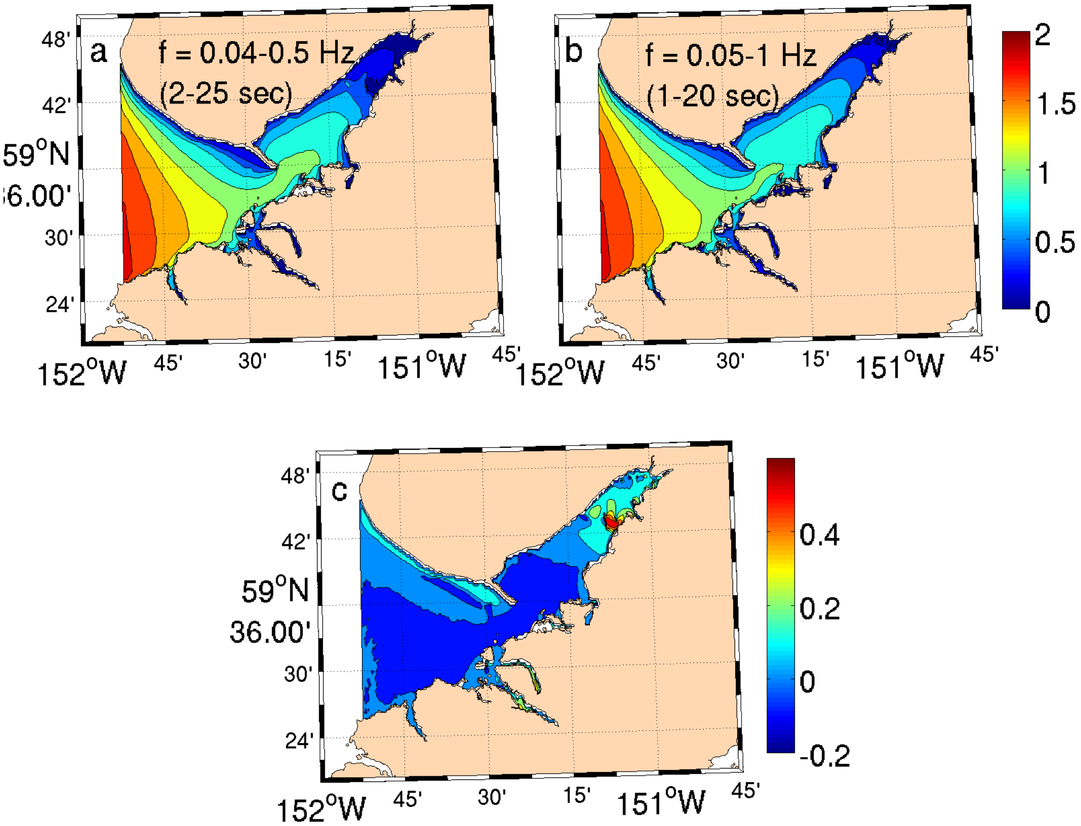

Fig. 59. Intercomparison of modeled SWH for (a) f=0.04-0.5 Hz (25 frequencies), (b) f=0.05-1 Hz (49 frequencies), and (c) difference, (b-a).

The effect of barotropic currents (tide and wind) was then added into the wave model to determine the extreme variations in the SWHs. The main goal was to check if these variations reconcile with the findings of Section 3.6 (where up to 1 m SWH variation was found in KB). An example snapshot of SWHs is shown in Fig. 60 which compares the performance of the outer and inner grids for KB region.

For the most part, the results from both the grids compare reasonably well in the "outer" bay region with and without the currents. This is encouraging as the outer grid resolution ($\sim$ 1 km) was about 5 times coarser than the nested KB grid ($\sim$ 200 m). The differences are more pronounced in the "inner" bay region, where the

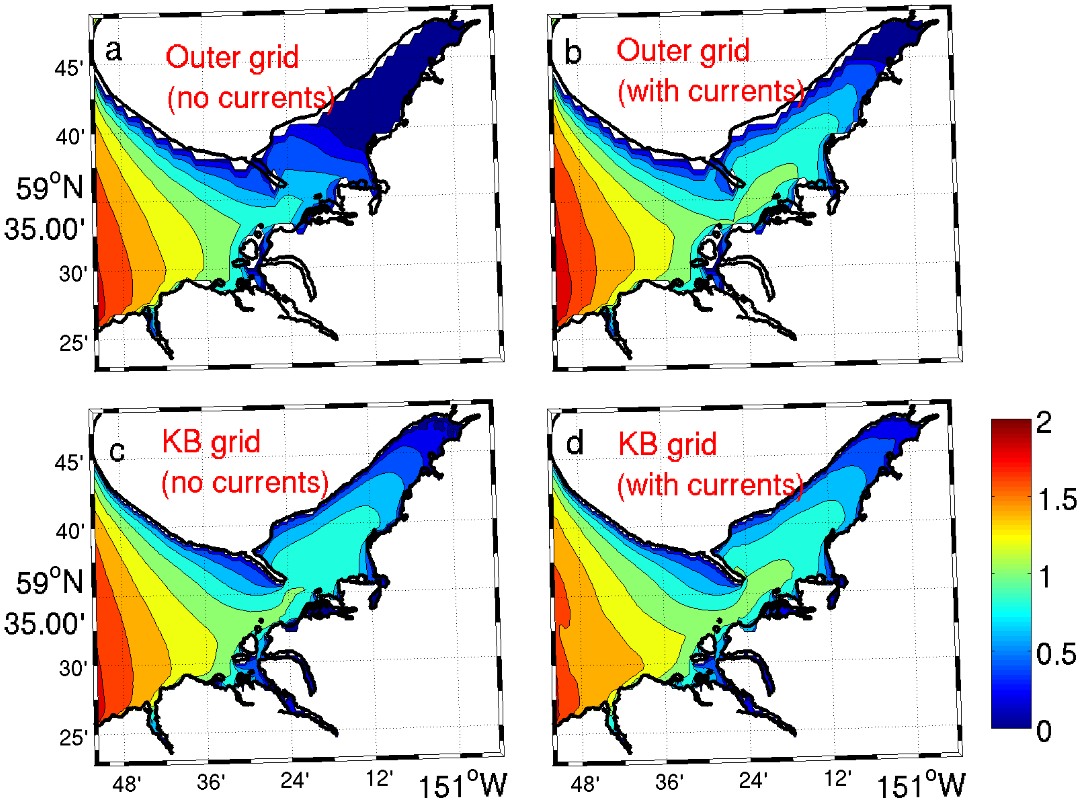

Fig. 60. Intercomparison of modeled SWH (in m) using low (top panels) and high-resolution (bottom panels) grids for KB region.

high-resolution grid shows development of waves further to the east even without the currents (Fig. 60c). This could possibly be due to the use of higher wave frequencies in the high-resolution grid (as discussed in Fig. 59). In addition, the outer grid does not resolve the coastal features properly, especially the Homer Spit and the western shoreline of the "inner" bay. Overall, it seems that the finer grid captures the shoreline variations better compared to the coarse outer grid.

Extreme analysis, similar to that done for the entire CI domain, was then performed for the coupled KB model. The maximum increase and decrease in SWH in the presence of currents is shown in Figs. 61 and 62. This analysis was also per-

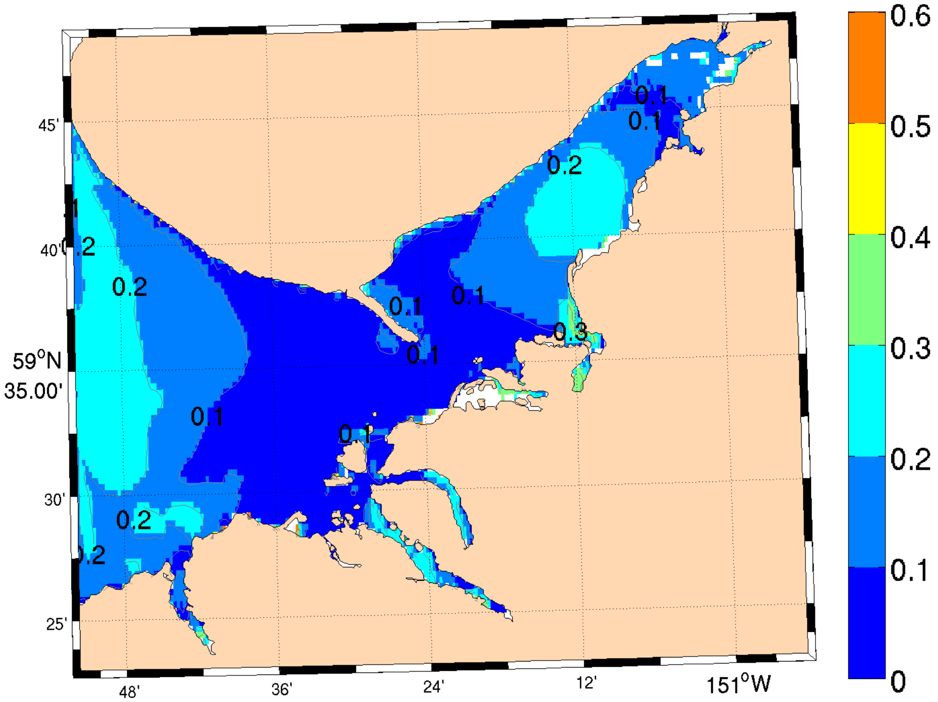

Fig. 61. Maximum increase in modeled SWH (in m) in presence of currents using finer KB grid.

formed over the two-week period. The maximum increase in SWHs is of the order of 0.2 m in the "inner" bay (Fig. 61), much smaller than the variation obtained using the outer grid (upto 1m; Fig. 33). The maximum decrease in SWHs was also found to be different for the two grids. The high-resolution grid shows large variations (~ -0.6m) along the western shoreline of the "inner" bay (Fig. 62), as compared to < 10 cm variation predicted by the outer grid (Fig. 34). The western shoreline, as discussed earlier, was mostly dominated by the wind-induced currents, and the effects of which are only captured by the high-resolution models. Although there are no data to validate either grid solutions, these findings illustrate that the coarse grid solutions may not be correct in the KB region and high-resolution grid is needed for better wave-current estimates.

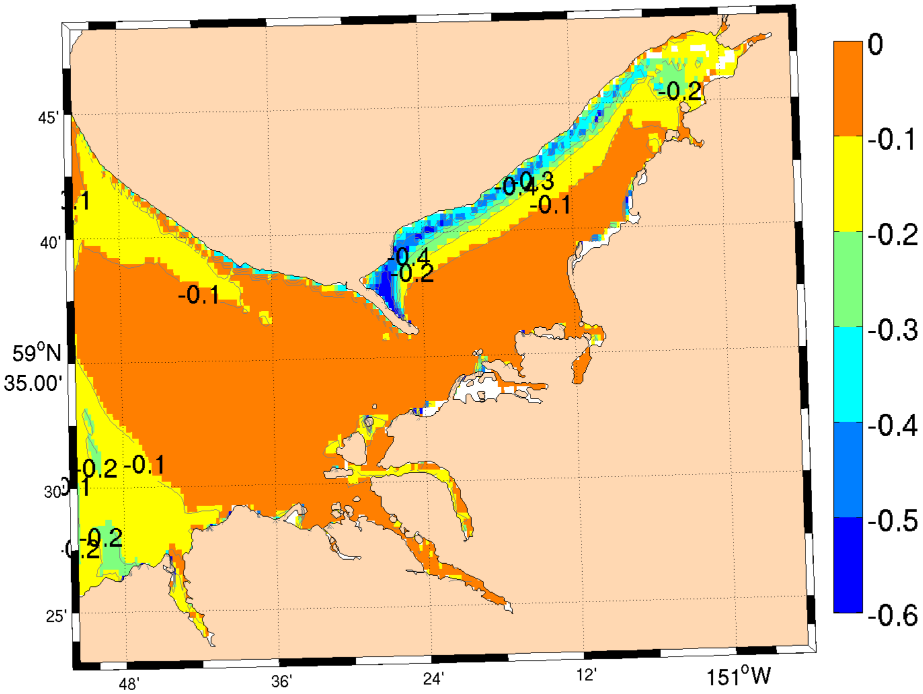

Fig. 62. Maximum decrease in modeled SWH (in m) in presence of currents using finer KB grid.

5.4 Discussion

The study undertaken in this section was motivated by the results obtained in Sections 3-4. In particular, this study performs high-resolution nearshore wave-current modeling in KB region in order to examine the validity of the outer grid solutions that showed upto 1 m variation in SWHs in the presence of currents.

The results indicate that a finer grid is required to accurately represent the complex coastal features of this region, in particular the Homer Spit. In addition, it is demonstrated that the locally-generated winds, for the most part, dominated the wave-current patterns in the "inner" bay. Hence, higher wave frequencies are required in order to resolve the short period waves in this region. This implies that the coarse resolution of the outer grid, along with the insufficient spectral frequency resolution, could have led to the inaccurate model results in the “inner” bay.

The circulation model was also evaluated for its capability of predicting the extent of dry regions, which are prominent along the western shoreline in the “inner” bay. Model simulations were performed using three different drying depths, viz. 10 cm, 20 cm, and 50 cm, and it was found that the choice of 50 cm drying depth captured the extent of dry regions quite well.

Overall, the results of extreme analysis using the finer grid show that the maximum increase and decrease in SWHs is about 0.2 m and 0.6 m respectively, in the presence of currents. These variations are different than those obtained using the coarse outer grid, further indicating the need for better-resolved grid in this region. The study conducted in this section could also benefit from future field measurements in order to verify the model performance.

6. DEVELOPMENT OF WAVE FORECASTING SCHEME FOR PRINCE WILLIAM SOUND, ALASKA

6.1 Introduction

Prince William Sound (PWS) is a relatively large inlet to the east of Kenai Peninsula in the Gulf of Alaska; it is surrounded by the Chugach Mountains (Fig. 63) which significantly influence the wind-fields in this area (Wang et al., 2001). PWS ecosystem provides habitat to various species of fish, birds, and other marine life. Most of the regions economy is based on oil, shipping, fishing, and recreation.

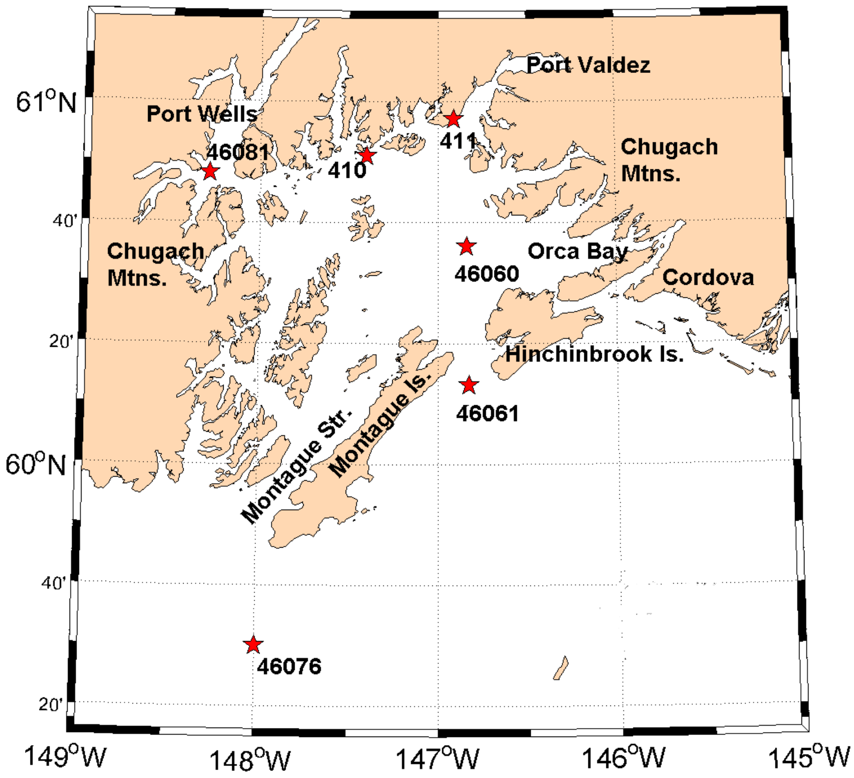

Fig. 63. Prince William Sound domain. Red stars denote the data locations.

PWS serves as a marine highway to hundreds of cargo ships, oil tankers, cruise ships, and ferries round the year. Port Valdez, at the north, is the epicenter of most of the shipping activity, and also the southern terminus of the Trans-Alaskan pipeline. To the east, the city of Cordova is home to Alaska's largest harbor with a capacity of over 500 fishing boats. From a technical/modeling perspective, the PWS domain has a complicated geometry (Fig. 63) that includes barrier islands at its mouth (Hinchinbrook and Montague islands), smaller islands inside the sound, numerous inlets and fjords (Valdez and Port Wells), bays and coves (e.g. Orca Bay), and a rugged mountainous coastline. Unlike most bays where the depths tend to decrease as one proceeds up the bay, a considerable increase is seen in PWS, with the depths changing from about 100 m offshore to over 450 m in the central sound; even larger depths are found in the north-west (Fig. 64). The presence of such geometrical and topographical features may be expected to influence wave propagation and growth via several mechanisms such as refraction, diffraction, and wave breaking and create significant spatial variations in the wave-fields.

Apart from these geometric complexities, the PWS domain also experiences extreme and complex weather conditions. According to Liu et al. (2006) "...during the cold season, the northern Gulf of Alaska is dominated by strong pressure gradients that interact with the underlying rugged topography to produce a variety of complex flows...." It is thus necessary to include the most accurate wind fields in the wave modeling scheme. In northern Gulf of Alaska, two sources of wind input are available. The Eta wind-fields provided by NCEP every 3 hours for the next 7 days are available on a resolution of about 30 km. However inside PWS, data points from Eta winds models are not available. As with the CI domain, high-resolution WRF winds are also available for PWS domain. The WRF forecast, which is provided by UAF once each day, includes hourly wind velocities for the next 48 hours.

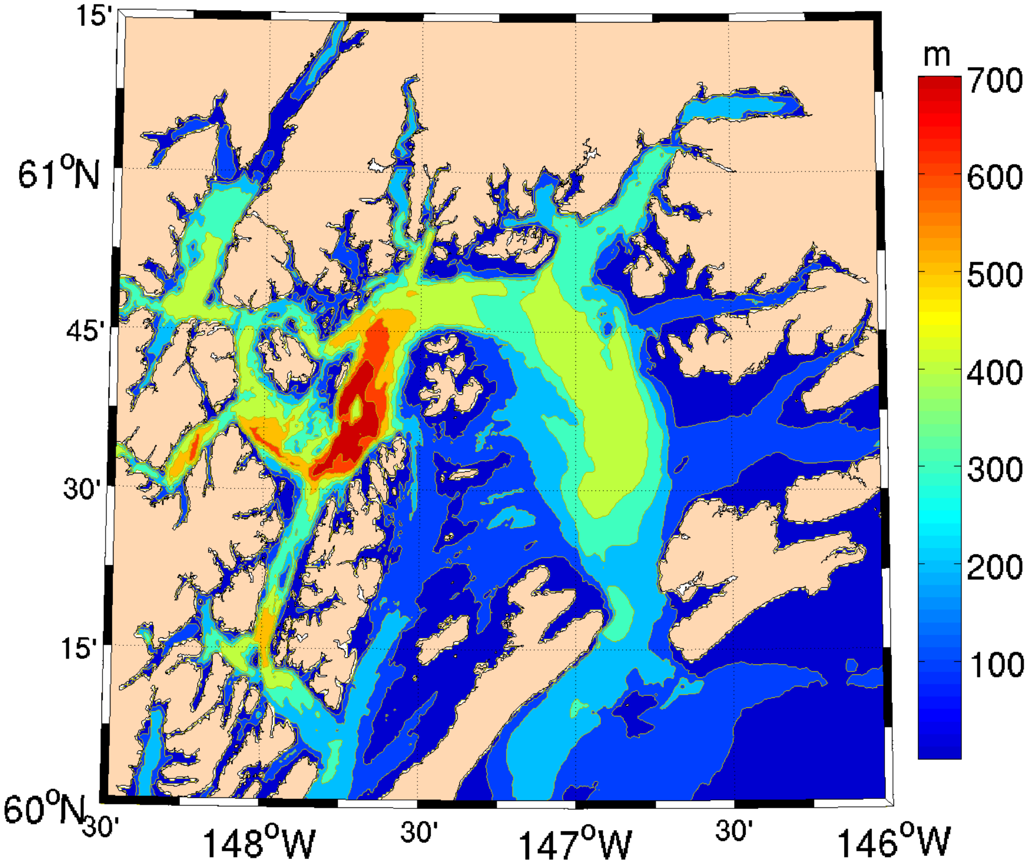

Fig. 64. Bathymetry of Prince William Sound.

This section describes the development of a forecasting system to support the safety of maritime operations in PWS, as part of the regional Alaska Ocean Observing System (AOOS). It involves a three-tiered coupled system: NOAA's WW3 simulations on a $\sim$ 30 km grid were used to force two other connected grids (which have resolutions of 2 km and 1 km respectively). As discussed earlier, WRF model provided the surface wind-fields. The research presented in this section differs from the existing literature on wave forecasts in the following ways. First, the PWS domain has an extremely energetic wind-wave climate with SWHs as large as 10 m during the winter season (`http://www.ndbc.noaa.gov/`). It also has significant spatial variability due to the presence of complex geometric features. In general, our analysis showed that waves are often attenuated by a factor of about 2 from the entrance of the sound to the central region. From the viewpoint of the performance of the system, these conditions are quite different from and somewhat more challenging than those studied by Dykes et al. (2009) in the Adriatic, which concerns fairly small SWHs (generally less than 3m) and low spatial variability. Next, the treatment of the forcing functions is different. As regards winds, Rogers et al. (2007) used the large-scale meteorological forecasts from NCEP for their regional domain, whereas in this study predictions from a regional wind model (WRF) have been used. Dykes et al. (2009) also have used a regional model, but it is different from the WRF model supported by the National Weather Service. For wave forcing along the open boundaries, we have had to rely on an approximate approach (necessitated by modeling convenience), to calculate directional spectra from the wave parameters obtained from the open-ocean simulations. In contrast, Rogers et al. (2007) forced the wave model with predicted details of directional wave spectra at two locations which were available to them. In the case of PWS such detailed spectral information is not readily available in the vicinity of the open boundary. On the other hand, Dykes et al. (2009) disregarded the use of boundary conditions due to the isolated nature of Adriatic Sea. This assumption is obviously not valid in PWS because significant wave energy is transmitted through the entrance between the barrier islands (Hinchinbrook and Montague) and also from the west of Montague Island (through Montague Strait) into the Sound (Fig. 63).

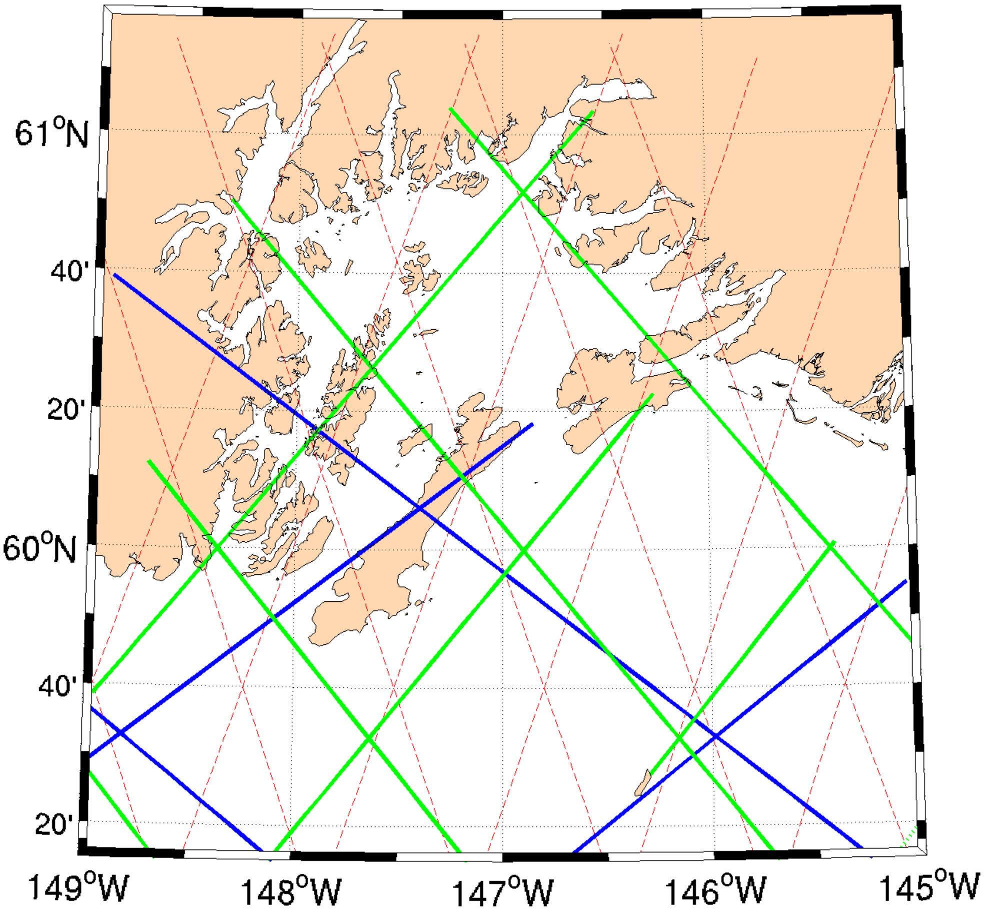

Fig. 65. Satellite tracks over PWS domain.

6.2 Available data

The daily forecasts from WW3 model for the Alaskan waters form the basis of wave information needed at the offshore boundaries. It includes wave parameters (SWH, Tp, and Dp) from which directional spectra can be approximated (details later). As regards model validation, data from four NDBC buoys are utilized: buoy 46076 (south of Montague Island), buoy 46061 at the entrance of PWS, buoy 46060 in the central sound, and buoy 46081 in the Port Wells region (Fig. 63). In addition to the above buoys, two wave gauges (410 near Outpost Island and 411 at the entrance to Valdez arm) were also deployed by the PWS OSRI to provide additional data points for model validation. The gauges were deployed in late October 2007 and recovered in first week of March 2008, coinciding with the time period of this study. Thus there were a total of six in situ sources of data, of which three were greater than 30 km from the shore (46076, 46061, 46060) and three were much closer (46081, 410 and 411 are less than 4 km, 1 km, and 0.5 km from the shore respectively).

Apart from the buoy and the gauge data, this dissertation also utilized satellite data for spatial validation of the wave forecasts. Fig. 65 shows tracks in the PWS domain for NASA's JASON-1 satellite (blue line), European Space Agency's ENVISAT satellite (red-dashed line; ENVISAT altimetry data were provided by the European Space Agency), and US Navy's Geosat Follow-On (GFO) satellite (green line). These satellites are on an exact repeat mission with the satellites flying over the same track every 10 days (JASON-1), every 17 days (GFO), and every 35 days (ENVISAT). SWH data are available at a distance of about 6 km along track. These satellite data greatly enhance the size of the database available for assessing system reliability.

6.3 Development of PWS forecasting system

The initial efforts in this dissertation involved experimentation with several grids in the hindcast mode. Initially, an outer grid at a resolution of 0.02^o ($\sim$ 2 km) containing 201x101 grid points and covering the region from -149^o W to -145^o W and 59.25^o N to 61.25^o N was developed (the boundary of Fig. 65). A model time-step of 12 min was used for this set-up. First, the sensitivity of using global (NAM) and regional winds (WRF) on wave predictions was done. Two simulations, one

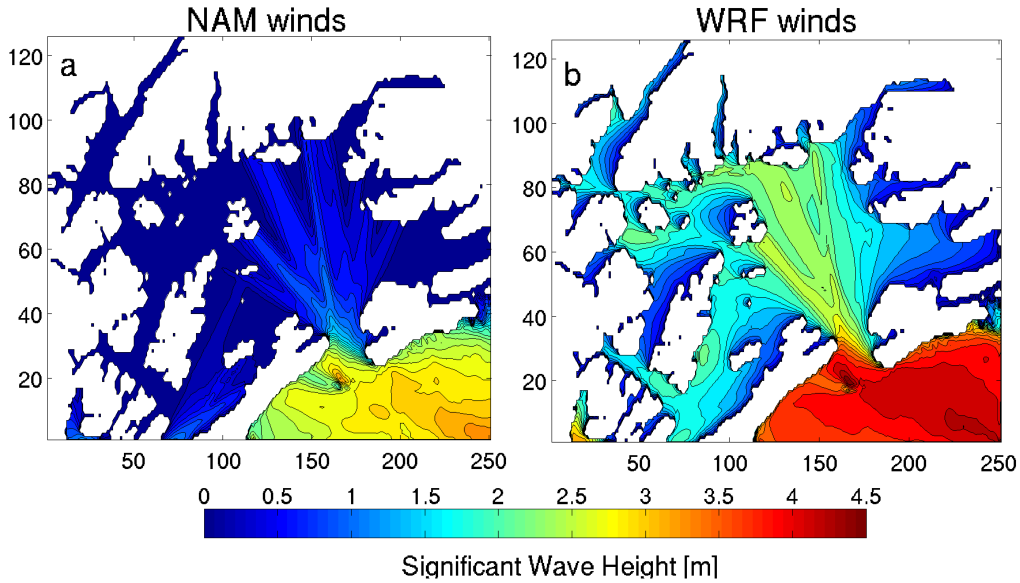

Fig. 66. Influence of (a) global and (b) regional winds on SWHs in PWS.

using the NAM winds and the other using the WRF winds, were performed. The boundary conditions on the open boundaries were assumed to be constant for both the runs. Also, the default settings for wave generation and dissipation were used in SWAN. The results of the two simulations, zoomed in over the PWS region, are shown in Fig. 66 for the same time instant. It is clear that the NAM winds, being at a coarse resolution, under-predict the wave climate inside the sound.

SWH predictions from the two wind models were also compared to the available data (Fig. 67). It is again clear that the winds from the WRF model provided better match for SWHs compared to those from the NAM model. It is thus clear that the NAM winds may not be appropriate for use in the wave modeling in PWS.

The wind-fields from WRF model were therefore used to force the wave model. The offshore wave data along the open boundaries were downloaded from the NCEP ftp server. The NCEP data are available only in the form of SWH, T_p, and D_p.

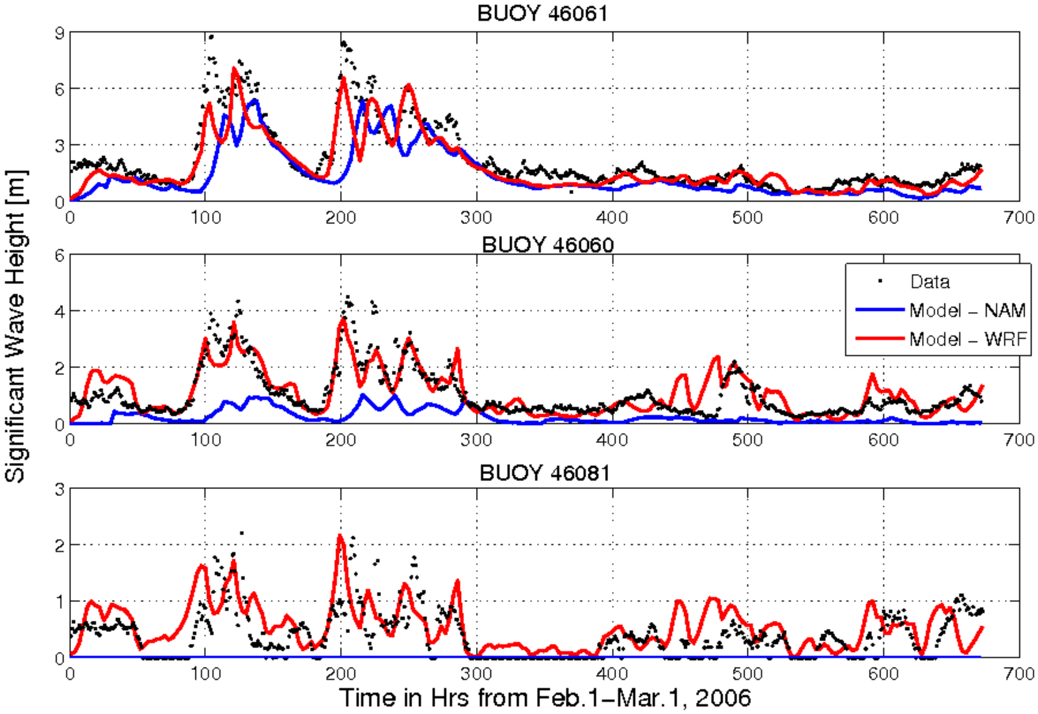

Fig. 67. SWH comparisons using NAM and WRF winds.

In general, boundary forcing in the form of directional wave spectra is needed. To address this, Rogers et al. (2007) used predictions of directional wave spectra at buoy locations which were then assumed constant along the open boundaries. Allard et al. (2008) forced their wave model with directional wave spectra generated by the 27-km European wave model at Fleet Numerical Meteorology and Oceanography Center. This would of course be the ideal method for coupling to a regional model, however for this study, directional wave spectra were not readily available from any external model; nor were there any buoys that provided reliable estimate of ocean conditions along all three open boundaries of PWS wave model domain. Two-dimensional wave spectra were therefore approximated using SWH, T_p, and D_p on the open boundaries in the following manner. First, the one-dimensional energy density was computed using the JONSWAP spectral form (using standard values for the parameters,$\gamma = 3.3$, σ_a=0.07, $\sigma_b = 0.09$). Since fetch length is not known, the coefficient α was calculated using the approximate integral form of the JONSWAP spectrum (Yamaguchi 1984):

$$\alpha = \frac{(2\pi)^4}{(0.06533\gamma^{0.8015} + 0.13467)} \frac{(SWH)^2 f_p^2}{16g^2} \tag{14}$$

where $f_p = 1/T_p$ is the peak wave frequency. The above approximation is accurate to within 0.3% for The one-dimensional spectra was converted to two-dimensional spectra using the dimensionless directional spreading function from Mitsuyasu et al. (1975).

Using the above settings, hindcast simulations were performed for a 10-day period during 2-13 April, 2007. As an example, SWH predictions on 6 April 00:00 UTC for the outer grid are shown in Fig. 68. The SWHs just outside the entrance were predicted to be around 6 m, attenuating to about 2 m in the central sound. A time-series comparison of SWH obtained using the outer grid are also shown at the locations of buoys 46061 and 46060 (Figs. 69a, b). At the location of buoy 46061 (Fig. 69a), three distinct storm events on 6, 7, and 9 April, with SWHs measured in the range 5-6 m, were reasonably predicted by the outer grid. Moving to the location of buoy 46060, the SWHs get attenuated to about 2.5 - 3 m; the model results are again reasonable. The outer grid results at the location of buoy 46081 (Fig. 69c), however, showed no wave development. Unfortunately, during this period, buoy 46081 was not transmitting data, thus the performance of the outer grid at this location cannot be evaluated. Nonetheless, the zero values of SWHs seem suspicious and indicate that the outer grid may not have properly resolved the wave climate at this location.

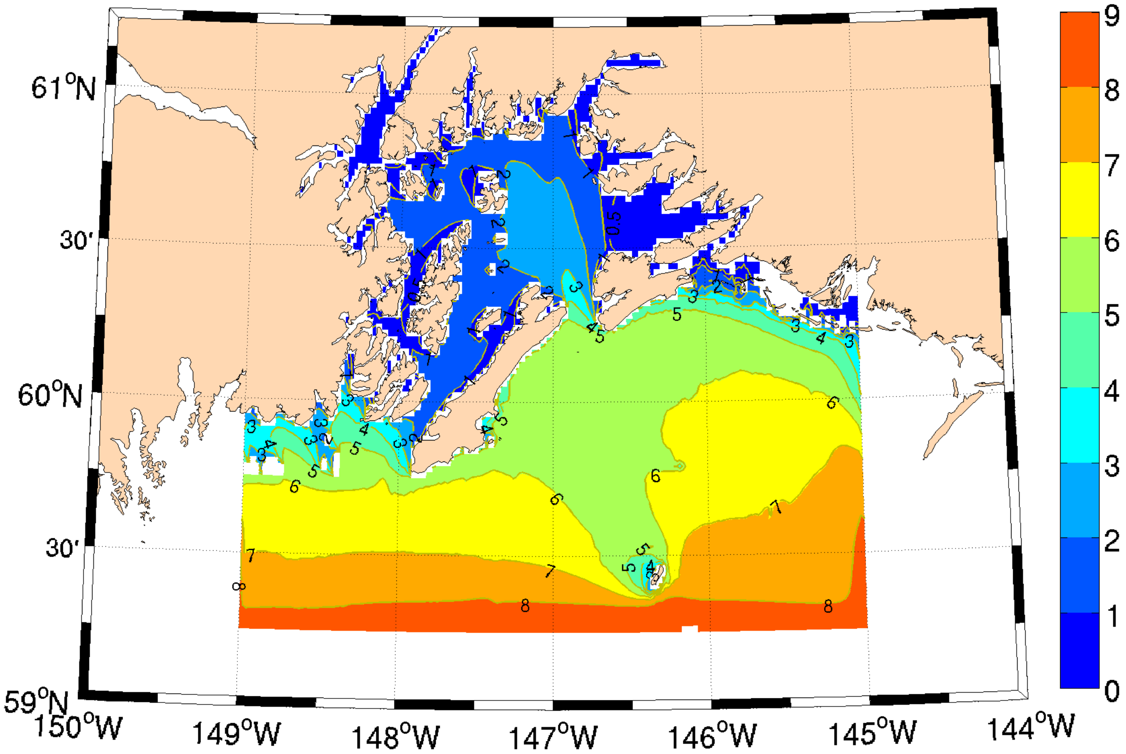

Fig. 68. An example snapshot of modeled SWH using the outer grid.

Therefore, another grid was constructed at a resolution of 0.01^o ($\sim$ 1 km) containing 251x126 grid points covering the region between -148.5^o W to -146^o W and 60^o N to 61.25^o N (Fig. 70). The hindcast simulations were performed for the inner grid using the same wind forcing. The solutions of outer grid at the boundaries of inner grid were used to drive the simulation for the inner grid. A snapshot of the SWH predictions from the inner grid is shown in Fig. 71 for the same event as in Fig. 68. The inner grid solution also shows the attenuation of SWHs by a factor of 2 as waves propagate northwards into the central sound. However, there are minor differences between the solutions of the two grids. In particular, the 2 m SWH contour extends farther north into the sound as compared to that from the outer grid solution. In addition, the inner grid performs better than the outer grid in resolving the near-shore

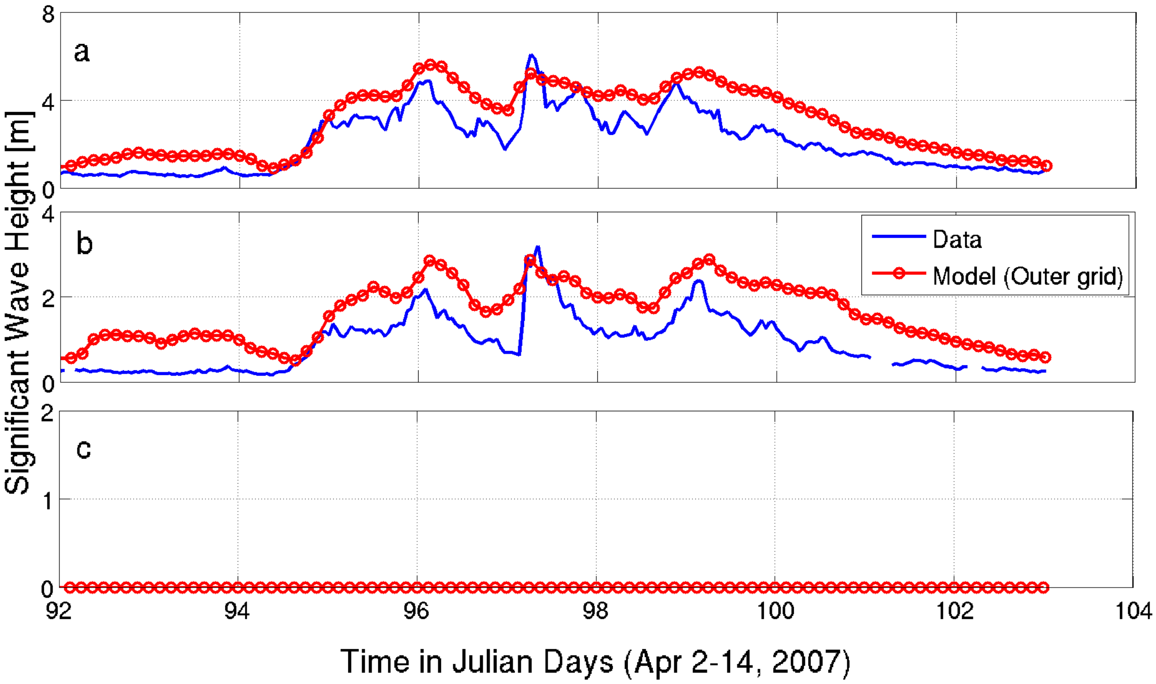

Fig. 69. SWH comparisons using the outer grid at the locations of (a) buoy 46061, (b) buoy 46060, and (c) buoy 46081.

features. Qualitatively, penetration and refraction/diffraction patterns through the islands in western part of the sound and in Orca Bay are more readily discernible.

A quantitative comparison of model predictions (using the inner grid) with data is also shown in Fig. 72. In general, the results of both simulations (inner and outer grid) appear to reproduce the storm events reasonably well. While there are no significant differences between the two simulations at the location of 46061 (Fig. 72a), some improvement with the inner grid is seen at 46060 (Fig. 72b). For very small waves, the improvement is of the order of 100%. As to the results at buoy 46081, the inner grid shows wave development as opposed to no waves using the outer grid.

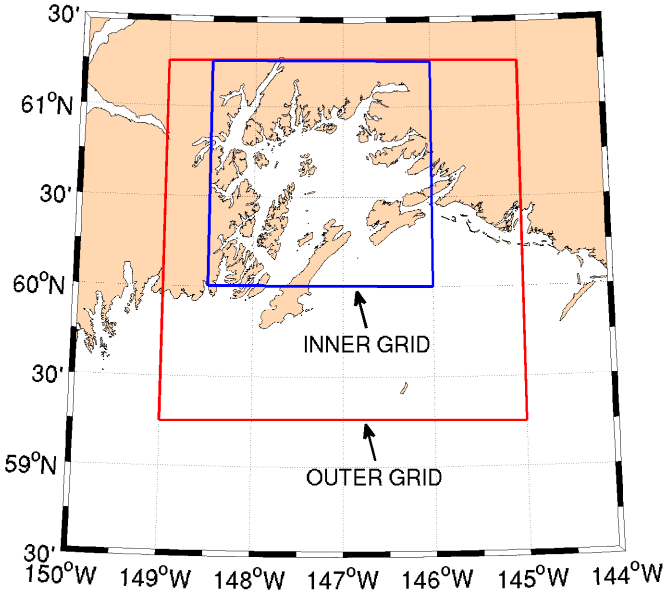

Fig. 70. Inner and outer grids for PWS wave model.

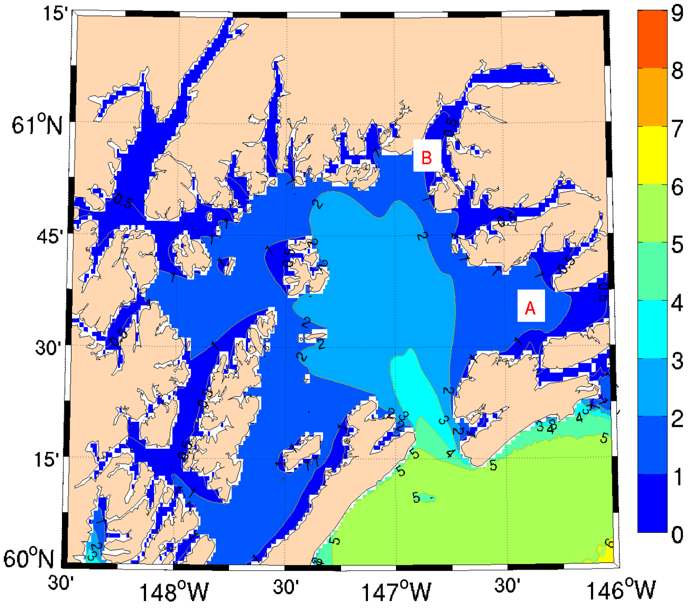

Fig. 71. Same as Fig. 68 but for inner grid.

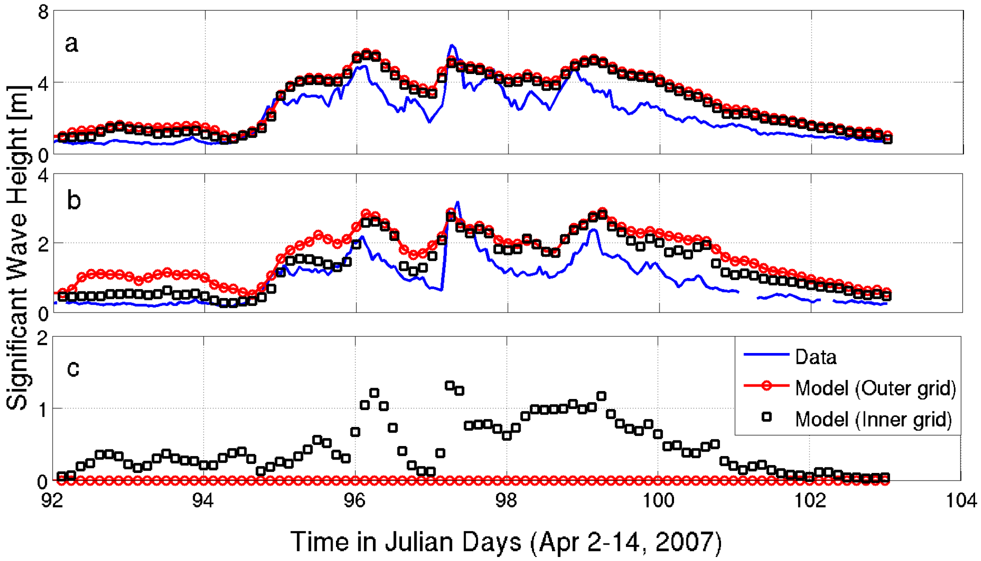

Fig. 72. SWH comparisons using the inner (squares) and outer (red circle) grids at the locations of (a) buoy 46061, (b) buoy 46060, and (c) buoy 46081.

Results were also examined at two other locations in the nearshore environment. These locations are marked by A & B in Fig. 71, and represent regions of interest, viz. the Port of Valdez area (shipping hub) and Orca Bay (site of extensive environmental research). These locations are much closer to the coast than the buoys 46061 and 46060, and thus should be affected by the grid resolution of the wave model. Note that there are no data gauges near A & B, and only the results from the two model grids are shown for intermodel comparison (Fig. 73). It can be clearly seen that the results from the two grids are different, with inner grid predicting larger SWHs compared to those from the outer grid.

To further check the validity of the inner grid solution in the nearshore environment, another event for which data at the location of buoy 46081 were available was modeled. The results shown in Fig. 74 confirm the observation that the outer grid is unable to resolve the near shore features (predicted SWHs are close to zero).

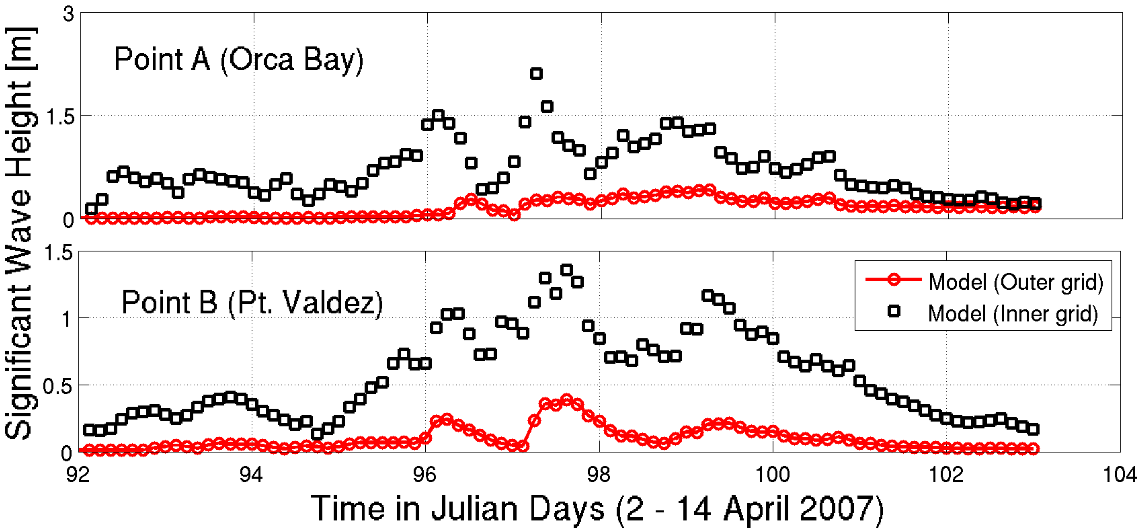

Fig. 73. SWH comparisons for the two grids at point A and point B.

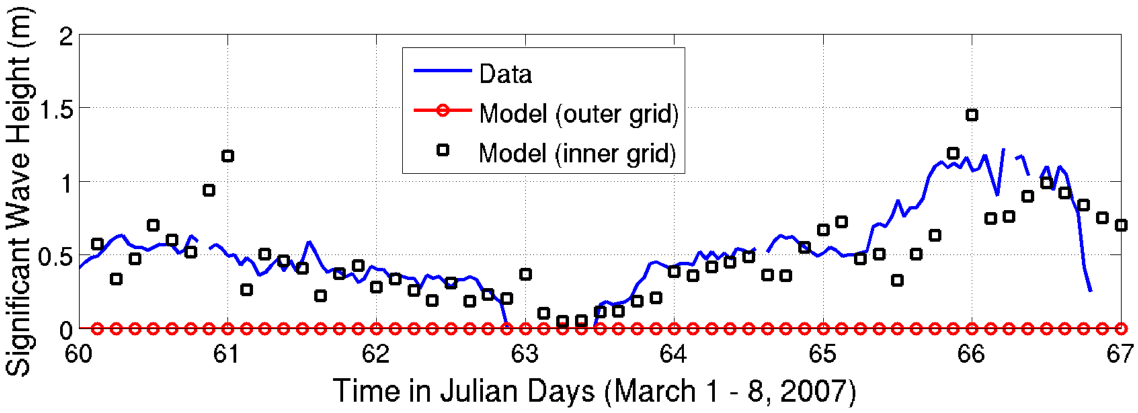

Fig. 74. SWH comparisons at the location of buoy 46081.

In contrast, the results from the inner grid match the data quite well. Thus, it is concluded that a higher resolution grid (∼1 km) is required for PWS domain to accurately resolve the nearshore wave climate.

A set of simulations was also performed using smaller time-steps. Fig. 75 shows the SWH results using time-steps of 12 min and 2 min. It is clear that there is no significant improvement from the use of smaller time-step, albeit the computational

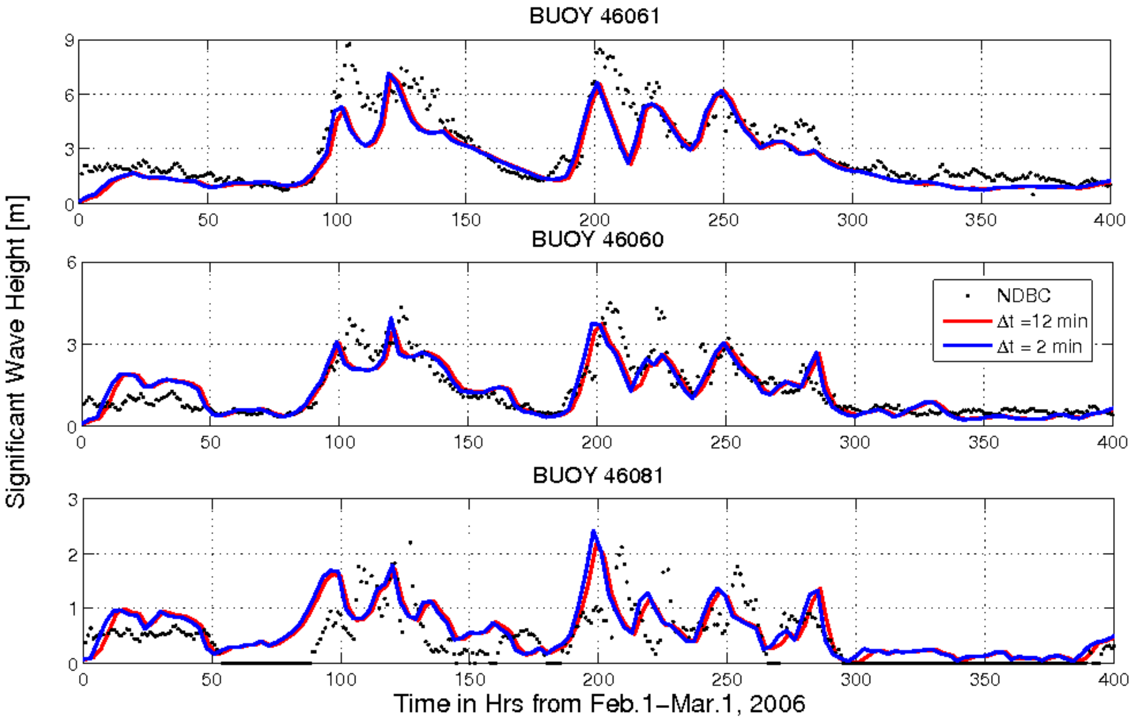

Fig. 75. SWH comparisons for different time-steps.

time increased drastically. Thus, it was concluded that 12 min time-step generated reliable results.

The wave model was next subjected to the input forcing of surface-currents from a barotropic model. Similar to CI, the PWS barotropic model was forced with the WRF wind input on the surface and water surface elevations on the open boundaries (Egbert and Erofeeva 2002). The barotropic model was only run for the inner grid and the coupling with the wave model was performed mainly to check if the inclusion of currents modifies the SWHs significantly. A sample snapshot of wind-wave-current conditions is shown in Fig. 76.

The winds during this event were mostly south-south west and ranged between 10-15 m/s (Fig. 76a). The flood current, flowing northward into the sound, was in

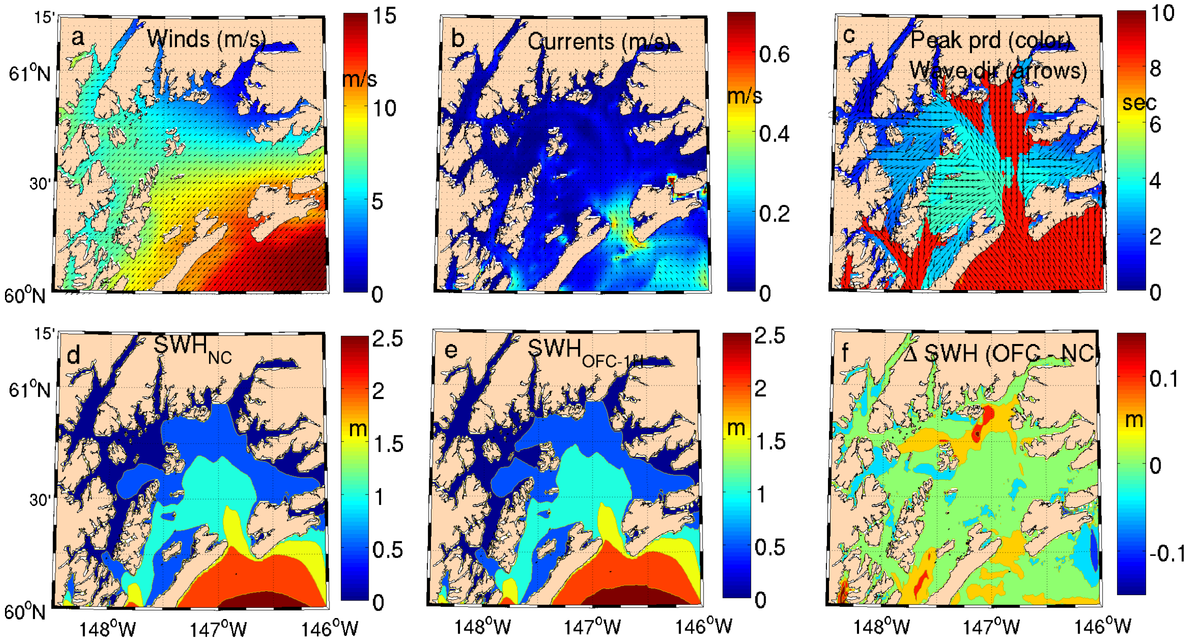

Fig. 76. Snapshot of wind-wave-current conditions for the inner grid.

the range 0.3-0.5 m/s with maximum intensity near the entrance (Fig. 76b). It can be clearly seen that the SWHs did not show a lot of variation upon the inclusion of currents. The maximum difference between the SWHs with and without the currents was on the order of ±10 cm (Fig. 76f). During other times also, it was found that the currents, for the most part, were of the order of 0.5 m/s near the entrance and inside the sound. The effect of these on SWHs was found to be minimal. It is thus concluded that the effect of currents is not significant on the wave climate in PWS. Hence, the wave-current interaction is not considered further.

6.4 Transition to operational mode

After the above testing, the nested grid system - comprised of the inner and outer grids - was used for forecasting purposes. For this purpose, a protocol to automatically download data by interconnecting two different FTP servers was developed. The system is run on a PC with a 3.40 GHz Pentium 4 processor and 2 GB of RAM, and uses a MATLAB code which is automated to run on a daily basis. The salient features of the system are shown in Fig. 77. The system is initialized at 00z and the input forcing functions are downloaded. The first 12 hours (denoted as “MODEL SIM TIME” in Fig. 77) include the time lag associated with the WW3 output (∼5.5 hours) and the WRF output (∼2.5 hours), and also the model computational time (∼ 2.5 hours). Overall about 12 hours of real time are lost in the modeling effort, and hence, even though each simulation is made for 48 h, the forecasts are provided at 12z for the next 36 h. Upon completion of the simulation, contour plots of SWH, T_p, D_p, and wave-induced velocities are generated and transferred to the AOOS FTP server. During the forecast mode, the sea-state at 24 h is also saved in order to initialize the next 00z run (the following day). The system obviously results in a 12 h overlap in the forecasts (between the last 12 hours of the previous days’ forecast and the first 12 hours of the current forecast). Consequently, for the recent 12 h, there will be an effect from two wind-fields which may or may not improve the wave forecast in some cases.

6.5 Discussion

Wave forecasts in coastal regions are needed for engineering and other applications. In this section, a high-resolution coastal wave forecasting system for PWS was developed using multiple nested grids. The scheme consisted of a three-way coupling between NOAA’s global model for wave boundary conditions, UAF’s local WRF model for wind-fields, and two nested grids for obtaining wave-fields in PWS.

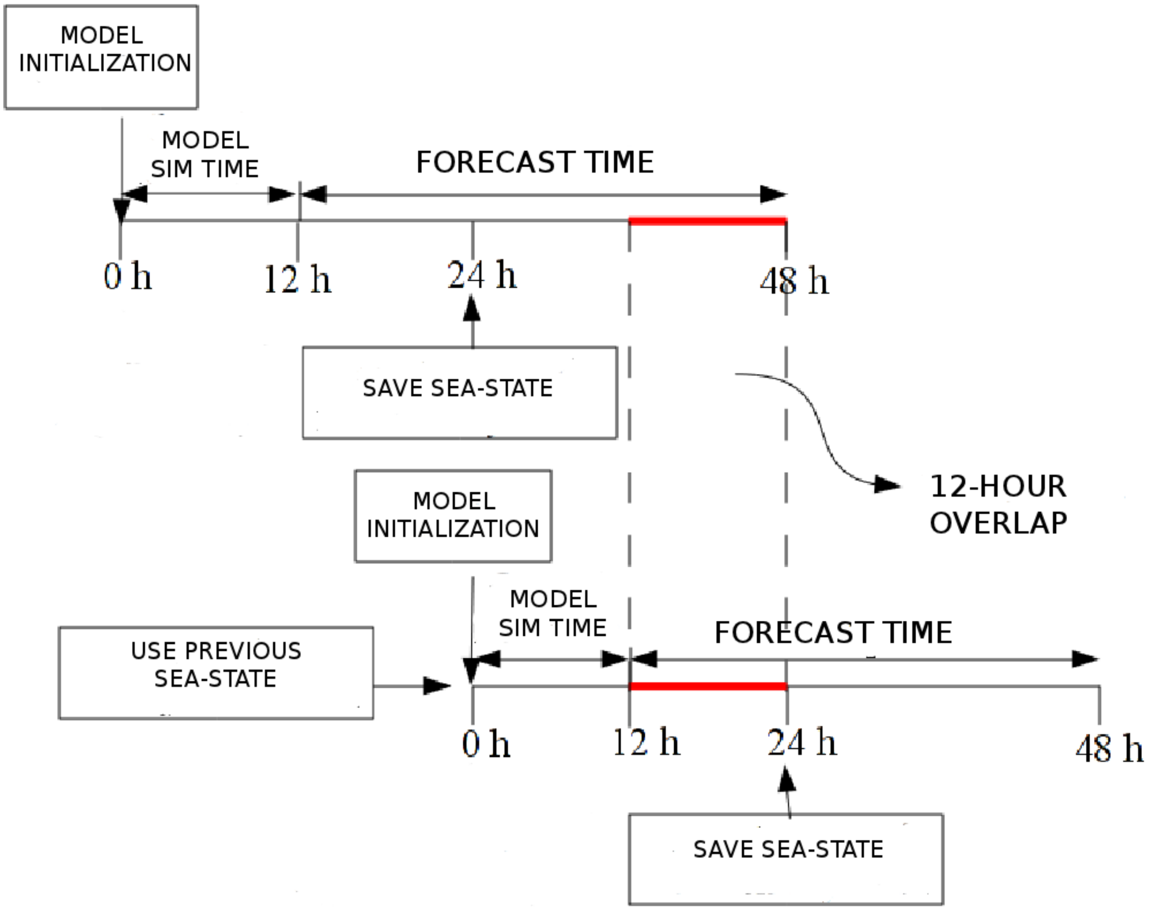

Fig. 77. PWS forecasting system protocol.

The system will provide daily forecasts (starting at 12z) for 36 hours on a continuous basis.

Although the system, as it stands, provides reasonable results for the hindcast studies described earlier, various errors that can accrue in the forecasts must be recognized. The assumption of JONSWAP spectral form to compute directional spectra at the open boundaries does not account for swell energy and may create errors, even though the total energy is conserved (this is briefly examined in the next section). In addition, errors can accrue from inaccuracies in the input forcing functions as obtained from other models (winds, SWHs at the open boundary, etc.)

and in the bathymetric representation. As regards the wind-fields, it was found in Section 4.4 that the random errors of the order of 10% have a relatively small effect on the predictions (see also Panchang et al. 2008). In any case, as stated in Section 1.3.1, if the model is to be run in the forecast mode, one has no choice but to accept that the flaws in the system exist and evaluate its reliability.

The reliability assessment of the wave forecasts is performed in the next section. Unfortunately in CI, there are currently no active buoys. Also, the historic wave data spans only a few months and that too with long gaps. Hence, the estimation of forecast uncertainty is only performed for PWS.

7. FORECAST SYSTEM RELIABILITY IN PRINCE WILLIAM SOUND, ALASKA

7.1 Introduction

After the hindcasting and testing work summarized in Section 6, operational forecasting was initiated in the PWS domain. In this section[1], the issue of forecast reliability is addressed in context of wave predictions in PWS. The motivation for this study stems from a need to provide reliable wave forecasts in order to meet various critical requirements associated with shipping, commercial and sport fishing vessel safety, and oil spill response. These needs mainly originate from lessons learned during the infamous "Exxon Valdez oil spill" in PWS in 1989 that destroyed most of region's ecosystem (Piatt et al., 1990). Mostly, the lack of suitable information on ocean climate affected the subsequent recovery and clean-up efforts. As a result, the PWS Oil Spill Recovery Institute (OSRI) has placed much emphasis on accurate environmental prediction.

For this purpose, wave forecasts are analyzed for roughly a year (June 2007 to May 2008) using the measured data. As stated earlier, this time period was selected, in part, due to the deployment of two wave gauges inside PWS - one near the outpost island (410), and the other at the entrance of Valdez arm (411) (Fig. 63). The data from the gauges were provided to us by PWS OSRI. Apart from the two gauges, measured data from four NDBC buoy locations (46076, 46061, 46060, and 46081) and a suite of satellite tracks were utilized in our statistical analysis. In the context of system reliability, these datasets were used to obtain reliability measures (in addition to the usual statistics) which can be used by managers of engineering operations,

---

[1] Parts of this section were published by Singhal et al. (2010). The author of this dissertation is permitted to reuse the published material "with permission from ASCE".

who are ultimately interested in knowing the likelihood of a predicted condition to actually occur and the associated error bounds.

7.2 Assessment of forecast skill: Results

During the initial analysis, it was difficult to make comparisons at the location of gauge 411 due to its close proximity to land (within 20 m). The model solutions from the inner grid, being at 1 km resolution, did not resolve such nearshore features, nor did the spatial interpolation from the closest grid points (which were about 1 km offshore) appear to represent the nearshore wave climate appropriately. SWHs from this gauge were mostly less than 1 m, and the model results at the closest grid point (1km offshore) were mostly overpredicted. Data from this gauge were therefore not considered in this analysis.

7.2.1 Quantitative assessment of wave forecasts

First, the impact of the approximated nature of the boundary conditions used in this study are discussed. For this purpose, SWH predictions at the location of buoy 46076 (within 30 km from the model boundary) are shown (Fig. 78). It can be seen that the model reproduces the data fairly well. Specifically, the larger SWHs (∼8 m) are reasonably predicted. In some cases, the latest forecast is better than the previous 36 h forecast. For example, the forecast made on day 321 captured the peak event (SWH ∼ 6 m) better than the forecast made on day 320 (Fig. 78). To examine the effect of the boundary conditions at other times and other locations, satellite data falling within a 20 km band inside the open boundaries were also used for comparison. Comparisons were performed for approximately 11 months. These comparisons are not described in detail since they are included in the overall comparisons described

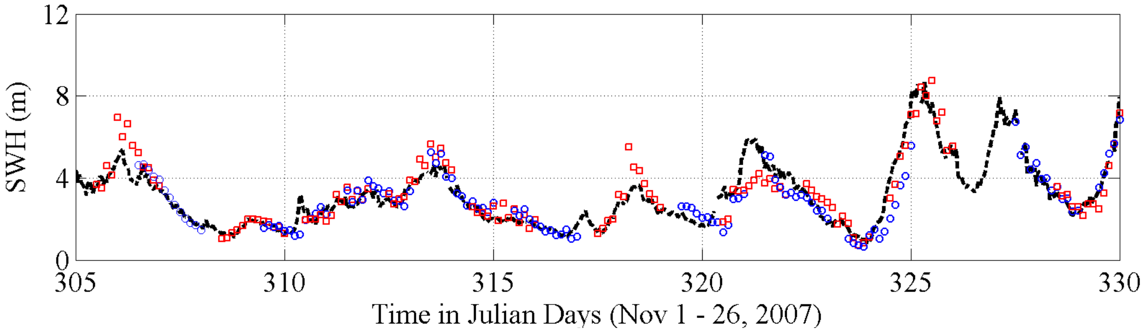

Fig. 78. SWH comparisons at the location of buoy 46076. Black dashed line represents measured data, alternate red and blue markers depict daily forecasts with 12 h overlap.

below; by way of summary, it is stated that a correlation coefficient of 0.95 resulted. This indicates that the approximate nature of the boundary conditions is reasonable.

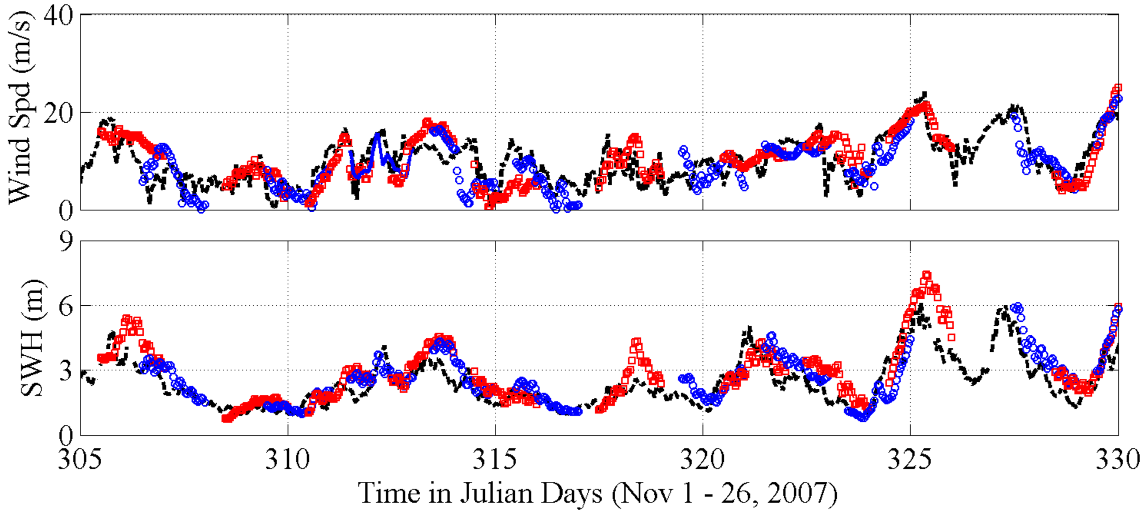

Fig. 79. Wind speed (top) and SWH (bottom) comparisons at buoy 46061. Legend is same as for Fig. 78.

To cite an example of the performance of the forecasting system, a time history of wind-wave forecasts during November 2007 is shown in Fig. 79. The month of November was observed to be the most energetic month marked by strong wind-wave events. The first half of the month experienced somewhat average, yet unfavorable (for marine activity), conditions: two peaks separated by about 10 days with SWH ∼4 m and wind speeds ∼15 m/s at the location of buoy 46061. The latter half of the month was dominated by larger waves with frequent occurrence of hazardous conditions (indicated by peaks about 3 days apart). At the location of Buoy 46061, the maximum wind speed was about 25 m/s, which was well predicted by the WRF model (Fig. 79 top panel), and the maximum SWH was about 6 m on day 330 (Fig. 79 bottom panel). Note that the maximum wave heights corresponding to these SWHs could be up to 10.8 m, if the Rayleigh distribution were to hold true (i.e. $H_{max} \sim 1.8$*SWH), and can pose a hazard to tanker traffic and cruise ships. Two additional peaks can be discerned around days 325 and 328 with SWHs of about 6 m (corresponding wind speeds were around 20 m/s). The wind and wave predictions are quite reasonable for the three storm events. The timing of each wind-wave peak is faithfully reproduced, albeit with some difference in magnitude (about 15% over-estimation on day 325). Given the magnitude of the three events, these errors are acceptable for most engineering purposes. Apart from these three peak events, the predicted SWHs were in reasonable agreement with data for the remainder of the month.

Wave predictions at the location of buoy 46060 also show similar agreement with data (Fig. 80a). Overall, the SWHs recorded at the location of buoy 46060 were about half of those at the location of buoy 46061 (similar to the findings of hindcast studies performed in Section 6.3). Model predictions were within 15% of the measurements at the location of buoy 46060, except on 23 November when the peak SWH was over-estimated by 25% (predicted SWH = 3.75 m, measured SWH = 3 m). At nearshore locations, i.e. at the locations of buoy 46081 and gauge 410, the SWHs

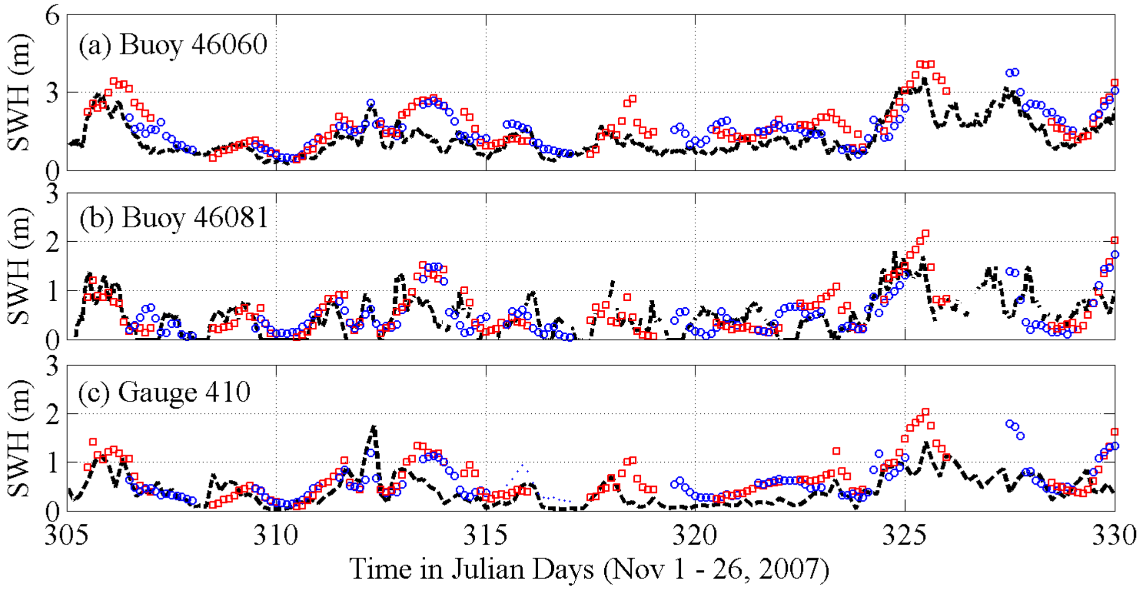

Fig. 80. SWH comparisons at (a) buoy 46060, (b) buoy 46081, and (c) gauge 410. Legend is same as for Fig. 78.

were generally small (Figs. 80b, c). While the model captures the observed trends reasonably well, occasional over-prediction is observed (e.g. days 325 and 330).

Apart from the temporal plot, a spatial plot of the wave-field obtained by the model during the peak event of 21 November is shown in Fig. 81. The wave forecast was made at noon on 20 November 2007 (UTC) and the predictions are shown for the 19 h forecast at 7 AM on 21 November 2007 (UTC). Data from measurement locations are also overlaid on the predicted wave-field. It may be noted that the satellite passes over the domain in about 15 seconds. Thus these data represent essentially a snapshot of the wave-field. The comparison between the measured data and the forecast is reasonable. In passing it is noted that during the same peak event, a preliminary estimate of wave-induced currents based on Stokes second order theory shows surface drift to be of the order of about 0.5 m/s. These estimates are of similar magnitude to the estimated barotropic currents shown in Section 6.3, and

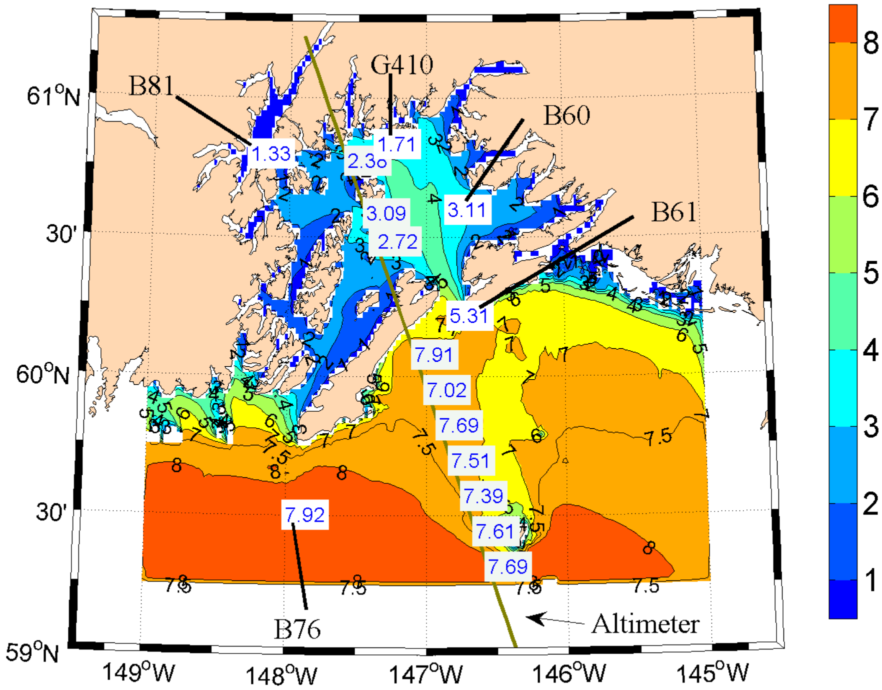

Fig. 81. Spatial comparison of SWH forecast with buoy and satellite data. Colors represent 19-h wave forecast, while numbers in boxes represent measured data. All units are in meters.

could play a significant role in overall fate of contaminant transport such as an oil spill. Along-track comparisons of wind speeds and SWHs during the same event are also shown in Fig. 82. The comparison between the measured data and the forecast is reasonable.

7.2.2 Statistical analysis of wave forecasts

A more comprehensive assessment of the forecasting system was performed through a statistical analysis of the results obtained during the full duration of this study. It is straightforward to compare the predictions with buoy data for any lead time L (up to the forecast length of 36 h) since both datasets are available at hourly inter-

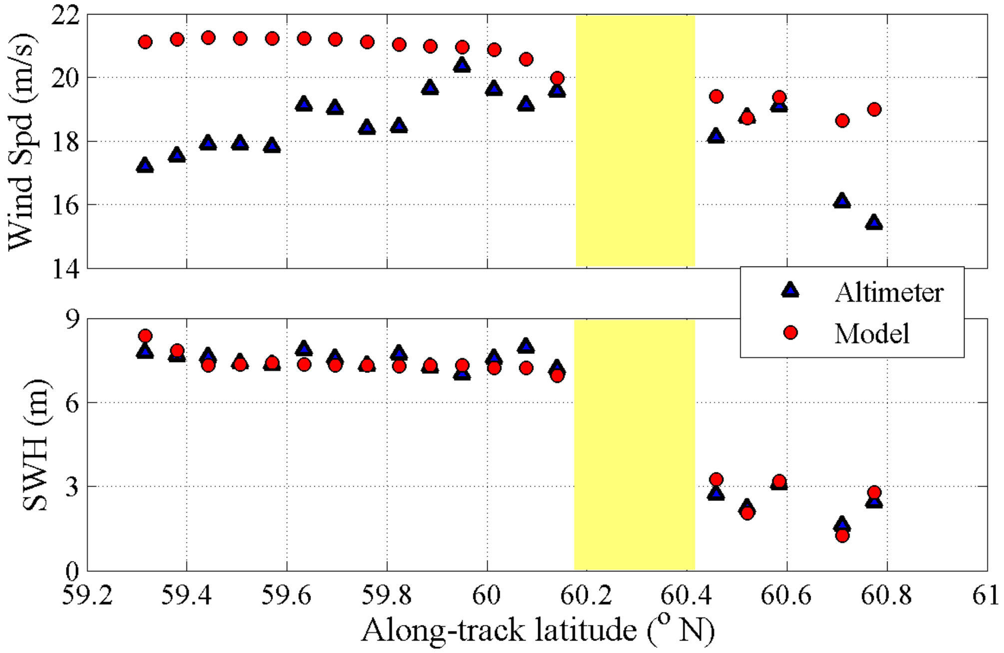

Fig. 82. Along-track comparisons of wind speed (top) and SWH (bottom) predictions. Yellow patch indicates when satellite crossed over land.

vals. Satellite data, on the other hand, are available only at specific times. In the model domain, the ENVISAT overflight corresponds to approximately 9 pm and 7 am (every 35 days); these data can thus be used only for comparing with forecasts made at noon the same day and the previous day (i.e. for L = 9 h, 33 h for a 9 pm forecast, and L = 19 h for a 7 am forecast). Similarly the overflight of other two satellites (JASON-1, GFO) corresponded to L = 9 h, 19 h, and 33 h as well as at other times. Thus, while it is possible to assess the forecasting model's performance for any L (up to 36 h) using buoy data, here we have used L = 9 h, 19 h, and 33 h in order to best use the satellite data, thus maximizing the spatial coverage and the data availability. Also, these lead times provide information on time scales that are reasonable for planning purposes.

Comparisons were performed after collocating measured wave heights from both point (buoy) and space (satellite) measurements in order to create a larger dataset. The predicted SWHs were spatially interpolated to conform to the exact measurement locations (buoy and satellite). For the buoy data, temporal interpolation was not necessary as both predicted and measured data were available on an hourly basis. As for the satellites, the crossing time was rounded to the closest forecast hour (most satellites crossed the domain in under 15 s). It may be worth noting that because of the grouping technique, the total number of points vary for L = 9 h, 19 h, and 33 h (more satellite tracks were available at 19 h, than at 9 h and 33 h). Also, due to input data outage (wind/boundary conditions and buoy measurements), a few of the wave forecasts were not processed (approximately 8% of the total 11 month test period). In general, we do not expect these issues to pose restrictions in our statistical analysis.

First, commonly-used statistical measures such as best-fit slope (m), correlation coefficient (R^2), root mean square error (RMSE) etc. were utilized to assess the overall reliability of the wave forecasts. These are shown in Fig. 83 and Table 4 for L= 9 h, 19 h, and 33 h. In general, the quality of the forecasts degrades for longer lead times. Overall, the correlation is high between the predicted SWHs and the data (R^2=0.83, 0.85 and 0.78 for the three forecasts) in spite of a lower correlation between the predicted and the measured wind speeds (R^2=0.64 for L = 9 h, 19 h; R^2=0.50 for L = 33 h). This dichotomy is particularly significant for L = 33 h; despite a somewhat low quality for the wind forecast ($R^2 = 0.5$), the influence on the SWH predictions is not significant. This could perhaps be explained by the possibility of the sea-state being fully developed at L = 33 h. The results contrasts the customary attribution of the mismatch between predicted and measured wave heights to poor wind predictions. This is encouraging because, in this case, these are

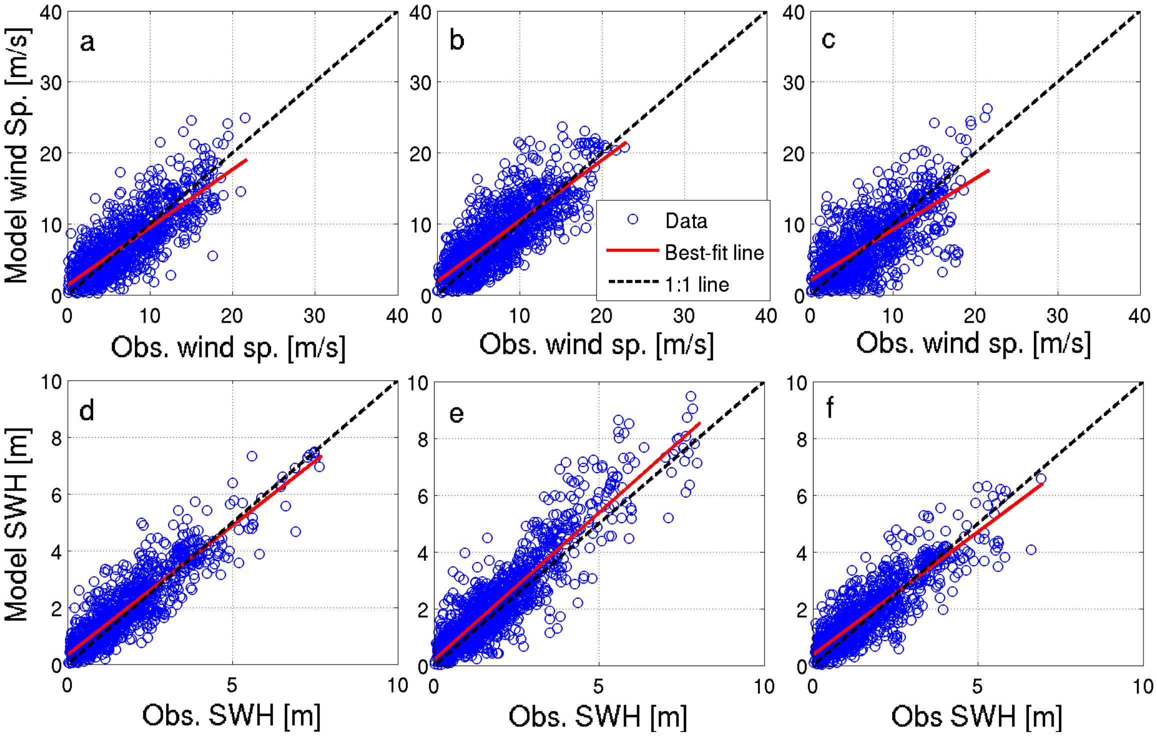

Fig. 83. Correlation plots of measured and modeled wind speeds (top panels) and SWHs (bottom panels) for (a), (d) L = 9h; (b), (e) L = 19h; and (c), (f) L = 33h.

Table 4
Statistical measures for wind speed (m/s) and SWH (m) for L = 9h, 19h, and 33h. m represents the best-fit slope, R^2 is the correlation coefficient, D is the index of agreement (Willmott et al. 1985), $RMSE$ is the root mean square error, and N is the sample size.

Measure	Wind Speed (m/s)			SWH (m)		
	9h	19h	33h	9h	19h	33h
m	0.82	0.85	0.72	0.91	1.04	0.87
R^2	0.64	0.64	0.50	0.83	0.85	0.78
D	0.89	0.88	0.84	0.95	0.94	0.93
$RMSE$	2.64	2.76	3.08	0.56	0.66	0.60
N	1164	1412	1156	1285	1533	1277

the only wind fields available and the effect of various flaws in the wind-fields (over which the modeler has no control) appear to impact the final product (SWH) only to a nominal extent.

For the most part, the predicted SWHs fell close to the slope 1 line. Specifically, Table 4 shows that the best-fit slopes for L=9 h, 19 h, and 33 h forecasts are 0.91, 1.04, and 0.87 respectively. Specifically, the performance of the modeling system during energetic wave events (i.e. wave heights larger than 6 m) was quite reasonable. Some of these SWHs (of the order of 8 m) are of a magnitude larger than that of a 50-yr return period condition (Londhe and Panchang, 2006); waves corresponding to such return periods have engineering significance and it is encouraging that they are properly predicted.

7.2.3 Uncertainty analysis and likelihood of occurrence

Plots such as shown in Figs. 79-83 give the impression that the forecasting system is reliable, but since the agreement is not perfect, such statistics do not enlighten the user as regards the likelihood of a forecasted event actually coming to pass. In other words, the probability of occurrence of each forecasted condition must be estimated. For this purpose, two methods are used: 1) RMSE method, and 2) Absolute error method. For both the methods, we first quantified all "predicted" wave heights into distinct wave groups from 0 - 1.5 m, 1.5 - 3 m, 3 - 5 m, 5 - 8 m, and 8 - 10 m. Grouping of wave heights based on the predicted values rather than on data is necessary since the measurements are not known a priori. The measured data points were then extracted for each predicted wave group. For the first method, the RMSE for each predicted wave group was estimated. Then, the absolute difference between each predicted wave height and the corresponding measured value were calculated. The percentage of data points for which this absolute value fell within specified intervals was estimated. The intervals chosen are 0.5, 1.0, and 1.5 times the RMSE.

For the second method, the absolute error for each predicted SWH was computed and percentage of values that fell within 15%, 25%, and 35% error was estimated.

The above analyses were performed separately for L = 9 h, 19 h, and 33 h. The results are summarized in Table 5. For the most part, the RMSE increased with increasing wave heights. The RMSE is about 15-20% of the median value for the larger wave groups (> 3m) for all lead times. For example, the estimated RMSE was around 2.02 m for waves in 8-10 m range for a 19-h forecast (about 20% of 9 m). Even though the RMSE of about 2 m seems large, it is reasonable given the size of the waves (8-10 m).

Table 5
Statistical estimates of forecast uncertainty and likelihood of forecast occurrence for L=9, 19, and 33h forecast.

L	Predicted SWH Group(m)	RMSE (m)	Likelihood of Occurrence						Samples (N)
			RMSE Bound			AE Bound			
			0.5	1.0	1.5	15%	25%	35%	
9-h	0.0-1.5	0.39	0.42	0.74	0.87	0.24	0.38	0.51	645
	1.5-3.0	0.63	0.42	0.70	0.86	0.40	0.60	0.77	423
	3.0-5.0	0.88	0.40	0.71	0.86	0.52	0.71	0.86	194
	5.0-8.0	0.92	0.57	0.70	0.78	0.70	0.87	0.96	23
	8.0-10.0	–	–	–	–	–	–	–	–
	Overall	**0.56**	**0.48**	**0.74**	**0.87**	**0.35**	**0.51**	**0.66**	**1285**
19-h	0.0-1.5	0.44	0.41	0.75	0.89	0.22	0.34	0.51	742
	1.5-3.0	0.69	0.43	0.69	0.86	0.39	0.57	0.75	475
	3.0-5.0	0.85	0.32	0.68	0.89	0.38	0.72	0.90	222
	5.0-8.0	1.35	0.27	0.67	0.87	0.35	0.69	0.85	84
	8.0-10.0	2.02	0.20	0.50	0.90	0.40	0.50	0.90	10
	Overall	**0.66**	**0.47**	**0.75**	**0.88**	**0.30**	**0.49**	**0.66**	**1533**
33-h	0.0-1.5	0.43	0.43	0.74	0.89	0.23	0.37	0.50	681
	1.5-3.0	0.70	0.41	0.70	0.86	0.37	0.56	0.71	406
	3.0-5.0	0.85	0.47	0.72	0.85	0.56	0.71	0.87	174
	5.0-8.0	1.05	0.44	0.69	0.75	0.56	0.75	0.94	16
	8.0-10.0	–	–	–	–	–	–	–	–
	Overall	**0.60**	**0.47**	**0.74**	**0.87**	**0.32**	**0.48**	**0.62**	**1277**

Moving to the right of the table, the error bounds to estimate the likelihood of occurrence are shown for the two methods described above. The results may be interpreted as follows. Table 5 shows, for example, that 71% of the predictions that fell in the 3-5 m range for L = 9 h have RMSE of 0.88 m. In other words, a wave height to be predicted in the range 3-5 m would have a 71% chance of actually being between 2.12-5.88 m (i.e. approximately within a tolerance of ±(1*RMSE)) if the forecasting system were to be implemented again. For the absolute error method, a predicted SWH in the same wave range (3-5 m) would have a 52% chance of being between 2.55 5.75 m with 15% absolute error bound. Overall the analysis shows that for all lead times, chances of a predicted wave height to occur within ±(1*RMSE) were around 70-75%; and around 50% within 25% absolute error. Obviously, the probabilities would increase or decrease depending upon the choice of the error bound (i.e. RMSE or absolute error).

7.2.4 Estimate of time-averaged sea-states

Due to modeling limitations, wave forecasting models sometimes miss the timing of extreme wave events (Londhe and Panchang 2006; Rogers et al. 2007). An example of such a discrepancy can be seen around 17 November when the predictions seem to have a time offset (Fig. 79). However, precise prediction of the peak may not be necessary; an average sea-state in an interval of time suitable for engineering operations (say 4 hours) may be adequate. For this purpose, a separate analysis was performed for the winter season using a slightly different technique than utilized for the entire year. Instead of using the hourly predicted values, we used a 4 h window around L = 9 h, 19 h, and 33 h and averaged all values that were contained within the window. This was mainly done in order to provide a “4-h averaged sea-state” that would incorporate the randomness during the 4-h period, more suitable for rapidly changing conditions.

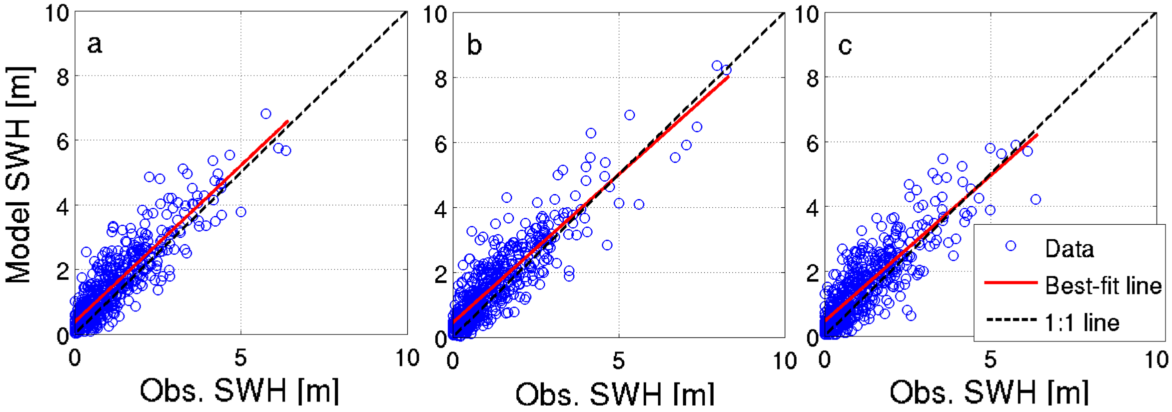

Fig. 84. Correlation plots of 4-h averaged SWHs for (a) L = 9h, (b) L = 19h, and (c) L = 33h.

In present analysis, we chose the averaging window between 7 - 11 h, 17 - 21 h, and 31 - 35 h for L = 9 h, 19 h, and 33 h respectively. Only data from point measurements (buoys and gauges) were included in the analysis as satellite data are not suitable for temporal averaging (most tracks crossed the domain in under 15 seconds). Again, all point measurements were collocated at different lead times. Correlation measures for the predicted and measured 4-h averaged sea-state are shown in Fig. 84 and Table 6. The overall statistics for the winter season were similar to that for the entire year. The only significant improvement was with the 9-h forecast where predictions were within 3% of the measurements ($m = 0.97$ for the best-fit line; Table 6). Other statistics were nearly identical for L = 19 h and 33 h lead times.

The likelihood of occurrence for each wave forecast during the winter season was also determined. Due to the availability of fewer data points, we divided waves into groups between 0-3 m and greater than 3 m. The results are shown in Table 7, and in general the statistics were similar to those shown in Table 2. Overall, chance of

Table 6

Statistical measures for 4-h averaged SWHs for L=9, 19, and 33h forecast lead times. Legend is same as that for Table 3.

Measure	SWH (m)		
	9h	19h	33h
m	0.97	0.91	0.90
R^2	0.78	0.78	0.72
D	0.92	0.92	0.90
$RMSE$	0.64	0.68	0.69
N	518	520	518

any forecasted wave condition to fall within ±(1*RMSE) is over 65%; if the error bound is ±(1.5*RMSE), the probability is greater than 82%.

Table 7

Statistical estimates of forecast uncertainty and likelihood of forecast occurrence for 4-h averaged sea-state for all lead times.

L	Predicted SWH Group(m)	RMSE (m)	Likelihood of Occurrence						Samples (N)
			RMSE Bound			AE Bound			
			0.5	1.0	1.5	15%	25%	35%	
9-h	0.0-3.0	0.56	0.46	0.71	0.85	0.22	0.35	0.49	460
	3.0-10.0	1.11	0.38	0.66	0.86	0.43	0.62	0.74	58
	Overall	**0.64**	**0.45**	**0.73**	**0.87**	**0.25**	**0.38**	**0.52**	**518**
19-h	0.0-3.0	0.61	0.43	0.73	0.86	0.17	0.31	0.46	458
	3.0-10.0	1.10	0.40	0.71	0.85	0.40	0.66	0.82	62
	Overall	**0.68**	**0.46**	**0.73**	**0.87**	**0.20**	**0.36**	**0.50**	**520**
33-h	0.0-3.0	0.63	0.44	0.73	0.87	0.19	0.30	0.44	467
	3.0-10.0	1.11	0.31	0.65	0.82	0.37	0.55	0.78	51
	Overall	**0.69**	**0.45**	**0.73**	**0.87**	**0.20**	**0.33**	**0.47**	**518**

7.2.5 Error statistics

Although the reliability of the forecasts, using the system as it stands, in terms of the probability of occurrence is, for the most part, of the order of 73% (for a tolerance of ±(1*RMSE)), the user would ultimately like greater accuracy. To that end, the results were examined in greater detail using additional statistical measures. Apart from R^2, RMSE etc., it is also important to report the "systematic" and "unsystematic" nature of errors (Willmott et al. 1985). These measures can provide useful information towards improving the reliability of the forecasting system. The systematic error indicates the deviation (bias) of the best-fit slope from 1:1 line whereas the unsystematic error explains the randomness associated with the predicted values. In general, the systematic error should be minimized in order to provide forecasts with maximum accuracy. The unsystematic error, on the other hand, should approach the RMSE. Our results show that the systematic error was relatively close to the RMSE for all wave groups, indicating the error to be largely biased (Table 8). If the entire dataset is used, the systematic error was smaller than 0.26 for all lead times. For each wave group, the unsystematic error was about half the RMSE suggesting that at least half of the error is random and cannot be remedied. For the entire dataset, the unsystematic error was close to RMSE (0.52, 0.61, and 0.56 for all lead times) suggesting that the forecasts are as good as they can be. In addition, Table 8 shows estimates of the index of agreement (D), a dimensionless quantity which indicates the extent to which model predictions are free of error (Willmott et al. 1985). In general, D is more than 0.50 for any given forecast; $D > 0.93$ if the entire dataset is used. Based on the estimates obtained using the entire dataset, it is clear that grouping of waves into distinct groups helps in identifying the large systematic errors that can be minimized to improve the reliability of forecasts.

It is obviously reasonable to explore methods to minimize the systematic error and hence provide the user with more reliable estimates. For example, Dykes et al. (2009) multiplied the input winds by a factor of 1.1 in an effort to improve a systematic under-prediction in SWH. It was, however, found that the under-prediction in SWH was not directly related to the under-prediction in the winds. In this study,

Table 8
Error statistics for all lead times. RMSES is the systematic RMSE, RMSEU is the unsystematic RMSE, SI is the scatter index, and D is the index of agreement.

L	Predicted SWH Group(m)	RMSE (m)	RMSES (m)	RMSEU (m)	Bias	SI	D	Samples (N)
9-h	0.0-1.5	0.39	0.26	0.29	0.11	0.53	0.75	645
	1.5-3.0	0.63	0.51	0.37	0.12	0.33	0.61	423
	3.0-5.0	0.88	0.78	0.41	0.11	0.26	0.60	194
	5.0-8.0	0.92	0.75	0.53	0.06	0.15	0.81	23
	8.0-10.0	–	–	–	–	–	–	–
	Overall	**0.56**	**0.21**	**0.54**	**0.11**	**0.36**	**0.95**	**1285**
19-h	0.0-1.5	0.44	0.33	0.29	0.05	0.53	0.69	742
	1.5-3.0	0.69	0.57	0.37	0.14	0.35	0.60	475
	3.0-5.0	0.85	0.70	0.51	0.19	0.29	0.61	222
	5.0-8.0	1.35	1.19	0.65	0.19	0.27	0.62	84
	8.0-10.0	2.02	1.98	0.41	0.27	0.30	0.50	10
	Overall	**0.66**	**0.26**	**0.61**	**0.15**	**0.40**	**0.94**	**1533**
33-h	0.0-1.5	0.43	0.29	0.28	0.08	0.55	0.71	681
	1.5-3.0	0.70	0.58	0.38	0.15	0.37	0.60	406
	3.0-5.0	0.85	0.76	0.37	0.07	0.24	0.57	174
	5.0-8.0	1.05	1.01	0.27	0.15	0.21	0.62	16
	8.0-10.0	–	–	–	–	–	–	–
	Overall	**0.60**	**0.23**	**0.56**	**0.10**	**0.39**	**0.93**	**1277**

an effort to improve the predictions was undertaken by the introduction of uniformly distributed error in the wind-fields (similar to that done for CI, Section 4.4). Unfortunately, the same response as that observed by Dykes et al. (2009) resulted. We therefore attempted to use the statistical nature of the errors to guide the improvement. In particular, the results summarized in Fig. 83 indicated an over-prediction for about two-thirds of the points. This information was used to "nudge" the predicted SWHs on a random basis to minimize over-predictions. Approximately 66% of the SWH predictions (randomly selected using a uniform distribution) were reduced by the RMSE for that SWH group; the remaining SWHs were similarly appropriately increased. Although the randomness was uniformly distributed, some values moved in the wrong direction and resulted in an even larger bias/error. Similar nudging was performed using the best-fit slopes and intercepts, however, the results failed to show a significant improvement. This effort was therefore abandoned.

7.3 Discussion

Since modeling schemes involve errors that may or may not be easily quantifiable or remedied, this section examined the issue of wave forecast reliability from the perspective of the user. This work is in keeping with ongoing research efforts which included a field experiment in PWS August 2009 for assessing the reliability of circulation and drift models using drogues (Schoch and Chao 2010, Schoch et al. 2011).

For assessing the reliability of wave forecasts, forecast data from June 2007 to May 2008 were utilized. From an assessment perspective, the choice of this period was fortunate since the 2007-08 winter months produced a dynamic wave regime in PWS, with SWHs (exceeding 7 m at the location of buoy 46061) comparable to the estimated 50-year event. In situ data at five locations and data from three satellites were utilized for spatial validation of the wave forecasts. These data were collocated to generate the largest dataset, based on the satellite over-flight time, for forecast assessment. This was done for forecast lead times of 9 h, 19 h, and 33 h. In general, the data showed an attenuation factor of about 2 in SWH from just outside of the sound to the central sound and the simulations appear to capture this attenuation. The results showed high correlation, in the range 0.78-0.85, between predicted and measured SWHs for the selected forecast lead times. The input wind forcing from WRF was reliable for the most part ($R^2 > 0.50$, $D > 0.84$) and, even when there was significant scatter relative to measured winds (e.g. scatter index = 0.46), the wave forecasts were reasonable.

The issue of forecast reliability has been briefly addressed in the past, mostly through the use of R^2, scatter indices, etc. These measures do not provide the user with guidance regarding the reliability of a given forecast. In this section, we estimated the likelihood of occurrence of a given forecast by availing of two statistical bounds, viz. the RMSE and the absolute error. The results, provided in Table 5, show, for example, that a predicted SWH in the range of 3-5 m for L = 19 h would have 68% chance of being within a tolerance of ±(1*RMSE) around a measurement (if one existed), and a 72% chance of being within a 25% of such a measurement. While these data may suggest that the error distribution is Gaussian, the bias towards overprediction and an estimate of kurtosis great than 3 violate the requirements of a Gaussian distribution. Assuming the modeling system (and all its components) perform in the same manner (i.e. barring changes to model physics, resolution, or grid configurations as demonstrated by Chen et al. (2007), etc.), a user could expect comparable performance in the future.

The results also show a systematic error, which manifests itself in the form of an over-prediction (positive bias) of SWHs. This indicates that future efforts should be focused towards improving the grid resolution (e.g. use of unstructured grids) and/or model physics (refraction/diffraction effects etc.), which erroneously contribute to over-prediction. In addition, the wave-current interaction, on 1 km grid resolution, did not alter the SWHs to a great extent. However, through use of unstructured grids, such higher order features could be resolved on much higher resolutions. Future studies could also be dedicated toward use of data assimilation techniques in wave modeling, in order to improve the estimates obtained in this work.

8. SUMMARY AND CONCLUSIONS

8.1 Main contributions

The main contributions of this dissertation are summarized in the following:

1. **Development of integrated forecasting schemes for coastal domains** This dissertation developed high-resolution integrated forecasting systems for Cook Inlet (CI) and Prince William Sound (PWS), Alaska by coupling regional wind, wave, and circulation models. Apart from their larger overall size compared to other existing integrated forecast systems (e.g. Humboldt Bay Harbor, Mississippi Bight), both these domains presented unique challenges that complicated surface modeling. For instance, these regions have complex bathymetry, rugged coastlines with meandering channels (e.g. Knik and Turnagain Arms), and sharp topographical gradients that abruptly rise to over 3000 m and greatly influence the wind-wave climate. In addition, CI domain experiences strong tidal fluctuations with prominent wetting and drying of shallow areas that further alters the wave climate. These complexities and the detailed qualitative and quantitative assessment of their impact on the wave climate have been addressed in this dissertation. The results of the coupled wave-circulation model were found to be qualitatively consistent with the expectations and inspired confidence in the forecasting schemes. It is also demonstrated that the integrated model is capable of reliably predicting the extent of dry regions in several shallower regions, for example the Turnagain Arm and the inner regions of Kachemak Bay. The results of the coupled model were also examined quantitatively, to the extent possible, and showed reasonable match to data.

2. **Viability of coupled wave-circulation modeling for forecasting purposes**

   This dissertation examined the viability of running a coupled wave-circulation model, from the viewpoint of the accuracy and efficiency, in the forecast mode. In particular, sensitivity studies involving the coupling of wave (SWAN) and circulation (EFDC) in one-way and two-way modes were performed to determine the extent of wave-current interaction along various regions of the domains. These studies show that, in the CI domain, the one-way coupling (from EFDC to SWAN) is sufficient and also more efficient than the two-way coupling to properly account for wave-current interactions. In contrast, it is shown that the coupling between SWAN and EFDC may not be needed in PWS domain, since the currents are relatively small ($\sim$ 0.5 m/s) and do not modify the wave climate to a great extent. Sensitivity studies involving the updating interval of water-levels and currents in the wave model showed that a smaller updating interval ($\sim$1h or less) is required for properly accounting the rapidly changing tidal conditions in CI. In addition, the adequacy of the barotropic model for CI wave modeling is examined by comparing modeled flow velocities to NOAA data obtained in 2005. On average, it is found that the barotropic model matched the observed flow velocities to a high degree ($R^2 > 0.8$).

3. **Mapping of regions with large SWH variability for various applications in CI**

   The work performed in this dissertation determined the spatial variability in SWHs due to the effects from various phenomena, and also generated statistical maps that show regions with extreme variations in SWH. It was found that the effects of wave-current interaction were most prominent in the northern

CI, with largest SWH variation of upto ± 1m. Extreme SWH variations were also found at the constriction near the Forelands, and in the region east of the Kalgin Island. Due to the presence of extensive offshore engineering (oil platforms, gas pipelines, etc.) in these regions, these findings are of vital importance for a number of applications (e.g. oil spill response and tracking, vessel safety and navigation, etc). In fact, over the last two decades, these regions have experienced significant oil spills (source: NOAA Oil Spill Response).

Large SWH variations (up to 1m), due to wave-current interactions, were also observed in the Kachemak Bay (KB) region using the outer CI grid ($\sim$ 1km resolution). These results, along with the economical (fishing/tourism/harbor) and scientific (largest national research reserve system) importance of this region, motivated an additional high-resolution ($\sim$ 200m resolution) modeling study to further examine the validity of the outer grid solutions. The results obtained from this study indicated that a finer grid is required for KB region in order to better capture the small-scale coastline features, in particular, the Homer Spit. It was also shown that the wind variability, as a result of mountainous topography, greatly influenced the wave climate, and hence higher wave frequencies (0.05 - 1 Hz) were required for properly resolving the locally generated wind-waves in this region. The coupled high-resolution model was also evaluated for its capability in simulating the extent of dry regions. It was found that the model reproduced the dry regions reasonably well with 50 cm drying depth (when compared to those shown in NOAA's nautical charts).

Sensitivity studies were also performed by altering the wind and current fields (through $\pm 10\%$ noise) to determine the corresponding variation in the wave predictions. It was, again, noticed that the largest SWH variation occurred in the northern CI region. Overall, the maps generated in this study can also be useful for planning future deployments of wave/current gauges to further understand the dynamic interactions between various phenomena. One prospective location for a wave gauge is to the east of Kalgin Island, where wave-current interaction was found to be significant. However, this region and other regions further to the north can have substantial ice formation during the winter season and thus seasonal deployment would have to be considered. Nevertheless, any data collected through such field surveys could be used for model validation purposes, and may lead to additional model advancements.

4. **New techniques for estimating forecast uncertainty and likelihood of occurrence**

   The issue of forecast reliability has been briefly addressed in the past, mostly through the use of R^2, scatter indices, etc. These measures do not provide the forecast user with guidance regarding the reliability of a given forecast. This dissertation thus examined the issue of wave forecast reliability using about a year of forecast data in PWS. In particular, the likelihood of occurrence of a given forecast was estimated using two statistical bounds, viz. the RMSE and the absolute error. The results, provided in Table 5, show, for example, that a predicted SWH in the range of 3-5 m for L = 33 h would have 72% chance of being within a tolerance of ±(1*RMSE) around a measurement (if one existed), and a 71% chance of being within a 25% error of such a measurement. Assuming the modeling system (and all its components) perform in the same manner, the forecast user could expect comparable performance in the future.

   These estimates have great practical significance for planning of various engineering applications, e.g. evacuation of offshore platforms, ship routing, coastal planning and assessment, etc. Such estimates could also be used to develop a real-time forecast uncertainty map over the coastal and global oceans, which mariners could readily access by punching in the "ocean zip-code" appropriate to their location.

5. **Development of user-friendly interface for real-time dynamic coupling of models**

   In order to develop the integrated forecasting schemes described in this dissertation, one of the biggest challenges was addressing the coupling of various models in dynamic mode. This led to the development of a simple interface, written in basic Shell scripting language embedded in a MATLAB code, that controlled the execution and data exchange between the two models. The basic working of this interface is described in the illustration shown in Fig. 21 in Section 3.6. Although it is shown that, on scales of roughly 1 km, this interface is not needed in CI, it could be used and easily applied to much smaller scales where the feedback from waves to currents could be significant.

8.2 Future directions

The research work described in this dissertation sets a solid foundation for future work. The most obvious and logical extension could be the implementation of unstructured grids that would resolve the nearshore features on much higher scales than considered in this work. This would also eliminate the need for multiple grids in various regions, and in general, should reduce the computational time for generating the wave forecasts. Although, this is debatable since SWAN developers mention that the use of unstructured grids does not necessarily improve the computational costs, and in some cases can become even more expensive than the structured grids.

With the advent of remote sensing, the use of data assimilation techniques is gaining prominence. Assimilation of satellite data in forecast models may improve the forecast reliability. This, however, poses limitations because of relatively low crossing frequency of satellites. In PWS, for instance, JASON-1 crossed the domain every 10 days and hence assimilation could only be performed every 10 days on a limited number of points, which may or may not improve the overall reliability. At any rate, exploration of such techniques still seems a viable option.

In the context of wave-current interaction studies, it also seems logical to perform simulations on much finer scales, particularly in the surf-zone, where wave-induced flows - in addition to tide- and wind-driven flows - could also become important. Such regions would require two-way dynamic coupling of wave and circulation models.

Another extension to this work could be the implementation of a sediment transport model. In general, the wind-wave-current motion can also initiate the movement of the sediment bed, which could in turn modify the wave-current patterns due to changes in the bathymetry and fluid density. The strong tidal currents, in the northern CI region near Anchorage, could alter the bed morphology thereby affecting the wind-wave-tidal dynamics. Obviously, accounting for such nonlinear interactions would require use of much higher resolution, along with the coupling of wind, wave, current, and sediment transport models. Fortunately, EFDC comes equipped with a sediment-transport module which would avoid the need for a separate model.

REFERENCES

Allard, R.A., Dykes, J.D., Hsu, Y.L., Kaihatu, J.M., Conley, D. 2008. A real-time nearshore wave and current prediction system. Journal of Marine Systems 69, 37-58.

Beget, J.E., Kienle, J. 1992. Cyclic formation of debris avalanches at Mount St. Augustine. Nature 356, 701-704.

Bidlot, J., Holmes, D.J., Wittmann, P.A., Lalbeharry, R., Chen, H.S. 2002. Intercomparison of the performance of operational ocean wave forecasting systems with buoy data. Weather Forecasting 17, 287-310.

Booij, N., Ris, R.C., Holthuijsen, L.H. 1999. A third-generation wave model for coastal region: 1. Model description and validation. Journal of Geophysical Research 104 (C4), 7649-7666.

Cavaleri, L., Bertotti, L., Lionello, P. 1991. Wind wave-cast in the Mediterranean Sea. Journal of Geophysical Research C96, 10739-10764.

Chakraborti, S.K. 1996. Equilibrium range spectrum of waves propagating on currents. ASCE Journal of Waterway, Port, Coastal and Ocean Engineering 122(6), 302-303.

Chen, Q., Wang, L. Zhao, H., Douglass, S.L. 2007. Prediction of storm surges and wind waves on coastal highways in hurricane-prone areas. Journal of Coastal Research 23(5), 1304-1317.

Chen, Q., Zhao, H., Hu, K., Douglass, S.L. 2005. Prediction of wind waves in a shallow estuary. ASCE Journal of Waterway, Port, Coastal and Ocean Engineering 131(4), 137-148.

Dingemans M.W., Radder, A.C., De Vriend, H.J. 1987. Computation of the driving forces of wave-induced currents. Coastal Engineering 11, 539-563.

Done, J., Davis, C.A., Weisman, M. 2004. The next generation of NWP: Explicit forecasts of convection using the Weather Research and Forecasting (WRF) model. Atmospheric Science Letters 5, 110-117.

Dykes, J.D., Wang, D.W., Book, J.W. 2009. An evaluation of a high-resolution operational wave forecasting system in Adriatic Sea. Journal of Marine Systems 78(1), S255-S271.

Egbert, G.D., Erofeeva, S.Y. 2002. Efficient inverse modeling of barotropic ocean tides. Journal of Atmospheric and Oceanic Technology 19(2), 183-204.

Funakoshi, Y., Hagen, S.C., Bacopoulos, P. 2008. Coupling of hydrodynamic and wave models: Case study for Hurricane Floyd (1999) hindcast. ASCE Journal of Waterway, Port, Coastal and Ocean Engineering 134(6), 321-335.

Gelci, R., Cazale, H., Vassal, J. 1956. Utilization des diagrammes de propagation a la prevision energetique de la houle. Bulletin d'Information du Comite Central d'Oceanographie et d'Etudes des Cotes 8, 170-187.

Gorman, R.M., Neilsen, C.G. 1999. Modelling shallow water wave generation and transformation in an intertidal estuary. Coastal Engineering 36, 197-217.

Guedes Soares, C., de Pablo, H. 2006. Experimental study of the transformation of wave spectra by a uniform current. Ocean Engineering 33, 293-310.

Hamrick, J.M. 1992. A three-dimensional environmental fluid dynamics computer code: theoretical and computational aspects. The College of William and Mary, Virginia Institute of Marine Science, Special Report 317, 1-63.

Hasselmann, K. 1962. On the non-linear energy transfer in a gravity-wave spectrum, part 1: general theory. Journal of Fluid Mechanics 12, 481-500.

Hasselmann, K., Barnett, T.P., Bouws, E., Carlson, H., Cartwright, D.E., Enke, K., Ewing, J.A., Gienapp, H., Hasselmann, D.E., Kruseman, P., Meerburg, A., Miller, P., Olbers, D.J., Richter, K., Sell, W., Walden, H. 1973. Measurements of wind-wave growth and swell decay during the Joint North Sea Wave Project (JONSWAP). Ergnzungsheft zur Deutschen Hydrographischen Zeitschrift Reihe 8(12), Supplement A, 1-95.

Hedges, S.T., Anastasiou, K., Gabriel, D. 1985. Interaction of random waves and currents. ASCE Journal of Waterway, Port, Coastal and Ocean Engineering 111(2), 275-288.

Holthuijsen, L.H. 2007. Waves in oceanic and coastal waters. Cambridge University Press, Cambridge.

Huang, N.E., Chen, D.T., Tung, C.C., Smith, J.R. 1972. Interactions between steady non-uniform currents and gravity waves with applications for current measurements. Journal of Physical Oceanography 2, 420-431.

Janssen, P.A.E.M. 1989. Wave-induced stress and the drag of air flow over sea waves. Journal of Physical Oceanography 19, 745-754.

Ji, Z.-G., Morton, M.R., Hamrick, J.M. 2001. Wetting and drying simulations of estuarine processes. Estuarine, Coastal, and Shelf Science 53, 683-700.

Jin, K.-R., Hamrick, J.H., Tisdale, T. 2001. Application of a three-dimensional hydrodynamic model for Lake Okeechobee. Journal of Hydraulic Engineering 126, 758-771.

Jin, K.R., Ji, Z.-G. 2001. Calibration and verification of a spectral wind-wave model for Lake Okeechobee. Ocean Engineering 28(5), 571-584.

Jin, K.R., Ji, Z.-G. 2005. Application and validation of three-dimensional model in a shallow lake. ASCE Journal of Waterway, Port, Coastal and Ocean Engineering 131(5), 213-225.

Johnson, M. 2008. Water and ice dynamics in Cook Inlet. Final Report, OCS Study MMS 2008-061. Mineral Management Service, 1-106.

Kain, J.S., Weiss, S.J., Levit, J.J., Baldwin, M.E., Brigh, D.R. 2006. Examination of convection-allowing configurations of the WRF model for the prediction of severe convective weather: the SPC/NSSL Spring program 2004. Weather Forecasting 21, 167-181.

Komen, G., Cavaleri, L., Donelan, M., Hasselmann, K., Hasselmann, S., Janssen, P.A.E.M. 1994. Dynamics and modeling of ocean waves. Cambridge University Press, Cambridge.

Kuo, A.Y., Shen, J., Hamrick, J.M. 1996. The effect of acceleration on bottom shear stress in tidal estuaries. ASCE Journal of Waterway, Port, Coastal, and Ocean Engineering 122, 75-83.

Liu, H., Olsson, P.Q., Volz, K.P., Yi, H. 2006. A climatology of mesoscale model simulated low-level wind jets over Cook Inlet and Shelikof Strait, Alaska. Estuarine, Coastal and Shelf Science 70, 551-566.

Londhe, S.N., Panchang, V.G. 2006. One-day wave forecast based on artificial neural networks. Journal of Atmospheric and Oceanic Technology 23, 1593-1603.

Longuet-Higgins, M.S., Stewart, R.W. 1964. Radiation stresses in water waves; a physical discussion with applications. Deep Sea Research 11, 529-562.

Mellor, G.L., Yamada, T. 1982. Development of a turbulence closure model for geophysical fluid problems, Reviews of Geophysics and Space Physics 20(4), 851-875.

Millar, D.L., Smith, H.C.M., Reeve, D.E. 2007. Modelling analysis of the sensitivity of shoreline change to a wave farm. Ocean Engineering 34, 884-901.

Mitsuyasu, H., Tasai, F., Subara, T., Mizuno, S., Ohkusu, M., Honda, T., Rikiishi, K. 1975. Observations of the directional spectrum of ocean waves using a cloverleaf buoy. Journal of Physical Oceanography 5, 750-760.

Moeini, M.H., Etemad-Shahidi, A. 2007. Applications of two numerical models for wave hindcasting in Lake Erie. Applied Ocean Research 29, 137-145.

Mölders, N. 2008. Suitability of Weather Research and Forecasting (WRF) model to predict the June 2005 fire weather for interior Alaska. Weather Forecasting 23, 953-973.

Nwogu, O. 1993. Effect of steady currents on directional wave spectra. In: Proceedings of the 12th International Conference on Offshore Mechanics and Arctic Engineering (OMAE) Glasgow 1, 25-32.

Oey, L.-Y., Ezer, T., Hu, C., Muller-Karger, F.E. 2007. Baroclinic tidal flows and inundation processes in Cook Inlet, Alaska: numerical modeling and satellite observations. Ocean Dynamics 57, 205-221.

Okkonen, S. R., Howell, S.S. 2003. Measurements of Temperature, Salinity, and Circulation in Cook Inlet, Alaska. Final Report, OCS Study MMS 2003-036. Mineral Management Service, 1-28.

Okkonen, S. R., Pegau, S., Saupe, S. 2009. Seasonality of boundary conditions for Cook Inlet, Alaska. Final Report, OCS Study MMS 2009-041. Mineral Management Service, 1-60.

Olsson, P.Q., Volz, K.P. 2011. Forecasting near-surface weather conditions and precipitation in Alaska's Prince Willian Sound with the PWS-WRF modeling system. Continental Shelf Research, in review.

Panchang, V.G., Jeong, C., Li, D. 2008. Wave climatology in coastal Maine for aquaculture and other applications. Estuaries and Coasts 31, 289-299.

Park, K., Jung, H.S., Kim, H.S., Ahn, S.M. 2005. Three-dimensional hydrodynamic eutrophication model (HEM-3D): application to Kwang-Yang Bay, Korea. Marine Environmental Research 60(2), 171-193.

Piatt, J.F., Lensink, C.Journal, Butler, W., Kendziorek, M., Nysewander, D.R. 1990. Immediate impact of the Exxon Valdez oil spill on marine birds. The Auk 107, 387-397.

Pierson, W.J., Moskowitz, L. 1964. A proposed spectral form for fully developed wind seas based on the similarity theory of S.A. Kitaigorodskii. Journal of Geophysical Research 69, 5181-5190.

Pierson, W.J., Neumann, G., James, R.W. 1955. Practical methods for observing and forecasting ocean waves by means of wave spectra and statistics. H.O. Pub 603, US Navy Hydrographic Office, 1-284.

Plant, N.G., Edwards, K.L., Kaihatu, J.M., Veeramony, J., Hsu, L., Holland, K.T. 2009. The effect of bathymetric filtering on nearshore process model results. Coastal Engineering 56, 484-493.

Ris, R.C., Booij, N., Holthuijsen, L.H. 1999. A third-generation wave model for coastal regions: part II-verification. Journal of Geophysical Research 104 (C4), 7667-7681.

Rogers, W.E., Hwang, P.A., Wang, D.W. 2003. Investigation of wave growth and decay in the SWAN model: three regional-scale applications. Journal of Physical Oceanography 33, 366-389.

Rogers, W.E., Kaihatu, J.M., Hsu, Y.L., Jensen, R., Dykes, J.D., Holland, T. 2007. Forecasting and hindcasting with the SWAN model in the Southern California Bight. Coastal Engineering 54(1), 1-15.

Schoch, G.C., Chao, Y. 2010. Ocean observing system demonstrated in Alaska. EOS Transactions 91(20), American Geophyical Union, 181-182.

Schoch, G.C., Chao, Y., Colas, F., Farrara, J., McCammon, M., Olsson, P., Singhal G. 2011. An ocean observing and prediction experiment in Prince William Sound, Alaska. Bulletin of American Meteorological Society, doi: 10.1175/2011BAMS 3023.1.

Schoch, G.C., Chenelot, H. 2004. The role of estuarine hydrodynamics in the distribution of kelp forests in Kachemak Bay, Alaska. Journal of Coastal Research SI(45), 179-194.

Shen, J., Boon, J., Kuo, A.Y. 1999. A numerical study of a tidal intrusion front and its impact on larval dispersion in the James River estuary. Estuary 22, 681- 692.

Shen, J., Kuo, A.Y. 1999. Numerical investigation of an estuarine front and its associated eddy. ASCE Journal of Waterway, Port, Coastal, and Ocean Engineering 125(3), 127-135.

Singhal, G., Panchang, V.G., Lillibridge, J.L. 2010. Reliability assessment for operational wave forecasting system in Prince William Sound, Alaska. ASCE Journal of Waterway, Port, Coastal and Ocean Engineering 137(6), 227-241. (Reused in this dissertation "With permission from ASCE").

Sorensen, O.R., Kofoed-Hansen, H., Rugbjerg, M., Sorensen, L.S. 2004. A third generation spectral wave model using an unstructured finite volume technique. In: Proceedings of the 29th International Conference on Coastal Engineering, Portugal, 3, 894-906.

Stabeno, P.J., Bond, N.A., Hermann, A.J., Kachel, N.B., Mordy, C.W., Overland, J.E. 2004. Meteorology and oceanography of the northern Gulf of Alaska. Continental Shelf Research 24, 859-897.

Sverdrup, H.U., Munk W.H. 1947. Wind sea and swell: theory of relations for forecasting. H.O. Pub. 601, US Navy Hydrographic Office, Washington DC, 1-44.

SWAMP Group 1985. Sea wave modeling project (SWAMP). An intercomparison study of wind wave predictions models, part 1: principal results and conclusions. Ocean wave modeling, Plenum, New York, 1-256.

Thomas, G.P. 1981. Wave-current interactions: an experimental and numerical study, Part 1: linear waves. Journal of Fluid Mechanics 110, 457-474.

Tolman, H.L. 1991. A third generation model for wind waves on slowly varying, unsteady and inhomogeneous depths and currents. Journal of Physical Oceanography 21, 782-797.

Tolman, H.L. 1999. User manual and system documentation of WAVEWATCH III version 1.18. NOAA/NWS OMB contribution 166, 1-110.

Tolman, H.L. 2009. User manual and system documentation of WAVEWATCH III version 3.14. NOAA/NWS/NCEP/MMAB Technical Note 276, 1-194.

WAMDI Group 1988. The WAM model - a third-generation ocean wave prediction model. Journal of Physical Oceanography 18, 1775-1810.

Wang, J., Jin, M., Patrick, E.V., Allen, J. R., Eslinger, D.L., Mooers, C.N.K., Conney, R.T. 2001. Numerical simulations of seasonal circulation patterns and thermohaline structures of Prince William Sound, Alaska. Fisheries Oceanography 10(1), 132-148.

Willmott, C.J., Ackleson, S.G., Davis, R.A., Feddema, J.J., Klink, K.M., Legates, D.R., O'Donell, J., Rowe, C.M. 1985. Statistics for the evaluation and comparison of models. Journal of Geophysical Research 90(C5), 8995-9005.

Yamaguchi, M. 1984. Approximate expressions for integral properties of the JONSWAP spectrum. In: Proceedings of the Japanese Society of Civil Engineering 345/II-1, 149-152 (in Japanese).

Zou, R., Carter, S., Shoemaker, L., Parker, A., Henry, T. 2006. Integrated hydrodynamic and water quality modeling system to support nutrient total maximum load development for Wissahickon Creek, Pennsylvania, Journal of Environmental Engineering 132(4), 555-566.

Zubier, K., Panchang, V., Demirbilek, Z. 2003. Simulations of wave at Duck (North Carolina) using two numerical models. Coastal Engineering Journal 45 (3), 439-469.

VITA

Gaurav Singhal received the degree of Bachelor of Technology (with Honors) in Ocean Engineering and Naval Architecture from the Indian Institute of Technology, Kharagpur, in 2003, Master of Science in Oceanography from Texas A&M University, in 2005, and that of Doctor of Philosophy in Ocean Engineering from Texas A&M University, in 2011.

He can be reached via Dr. Vijay Panchang, Professor and Head, Maritime Systems Engineering, 200 Seawolf Parkway, Texas A&M University, Galveston, TX 77553, or by email at singhalg@gmail.com.